Signatures of electronic excitations in the Raman spectra of graphene materials

Garcia-Ruiz, Aitor

Award date:
2020

Awarding institution:
University of Bath

Signatures of electronic excitations in Raman spectra of graphene materials

A DISSERTATION PRESENTED
BY
AITOR GARCÍA-RUIZ FUENTES
TO
THE DEPARTMENT OF PHYSICS

IN PARTIAL FULFILLMENT OF THE REQUIREMENTS
FOR THE DEGREE OF
DOCTOR OF PHILOSOPHY
IN THE SUBJECT OF
PHYSICS

BATH UNIVERSITY
BATH, UNITED KINGDOM

SEPTEMBER 2019

Thesis advisor: Marcin Mucha-Kruczyński Aitor García-Ruiz Fuentes

Signatures of electronic excitations in Raman spectra of graphene materials

Abstract

In this thesis, we present the tight binding method to describe electronic properties of graphene. We begin with a theoretical description of electronic Raman scattering (ERS) in graphene, under the framework of time-dependent perturbation theory. Our original work is presented in chapters 4, 5 and 6. In each chapter, we model the Raman spectra of graphene-based systems of special interest in carbon research: superconducting graphene, graphite and twisted bilayer graphene. Our findings underpin that purely electronic excitations in Raman spectra generate distinctive features that allows us to characterise and study these materials. In particular, Raman spectra give us insights into the position of van Hove singularities, the size of gaps or the flatness of bands. At the end of each chapter, we provide additional information about the current experimental status.

Contents

Acknowledgments

Almost every single thesis starts with the acknowledgement to the supervisor, and this one is by no means an exception. Marcin taught me how important conciseness is and his support and ideas have been the cornerstone of this work. Furthermore, he has helped me in the development of my future career, by establishing collaborations with other researchers. This takes me to my second acknowledgement, to Professor Vladimir Falko. His contribution to the direction of this thesis was immense, and I learned a lot from the fruitful meetings. I would like to thank my mum too, who greatly supported me throughout my PhD journey. Last but not least, I would like to thank Daniel Lagos, also finishing his PhD at the university of Bristol, and the colleagues in my office, in 4W 4.5, for so much banter.

No amount of experimentation can ever prove me right; a single experiment can prove me wrong.

Albert Einstein

1 Introduction

Graphene. The prefix *graph-* immediately tells the reader about the link of this word with writing. Such link in graphene is twofold: not only it has been in pencils for centuries, but it has also inspired an enormous amount of scientific literature. Many graphene experts agree that the starting point for graphene science was in 1859, when B. Brodie discovered a method to obtain graphite flakes [1]. Later on, the structure of graphite was determined by X-ray diffraction in powder [2] and single-crystal [3], and the first theory to understand this material was first proposed by P. Wallace in 1947 [4]. The following decades shaped scientific research on graphite. H.P. Boehm, who first coined the word "graphene" to describe single-layer graphite sheet, produced in 1962 a few layers graphite films [5], and one decade later, epitaxial graphene was grown from substrates [6, 7]. In the meantime, theorists noticed that relativistic physics of Dirac fermions could emerge from an effective low-energy description of graphite [8]. We witnessed in

the eighties the discovery of fullerenes, carbon atoms held together by single and double bonds that form a closed mesh [9, 10], and in the following decade, the rise of carbon nanotubes [11, 12]. The millennium ended and yet the quest for the truly two dimensional counterpart of graphite still continued.

The giant leap in the history of graphene took place in 2004, when Sir A. Geim and Sir K. Novoselov exfoliated mechanically the first graphene flake using the Scotch tape method [13], for which they were awarded with the Nobel prize six years later. Their deed triggered an unprecedented 'gold rush' in carbon research. From the point of view of theoretical physics, this finding challenged the grounds of physics, as it was thought that thermal fluctuations would destroy any kind of 2D order [14–17]. From the point of view of experimental physics, properties of graphene beat records: it has a superb thermal conductivity [18], its electrical conductivity is greater than copper [19], the spin-orbit coupling is weak in graphene [20, 21], which enables spin transport [22–24], optical absorption is so strong that one can spot graphene flakes with the naked eye [25] and it is the strongest and thinnest material ever made [26].

It is, therefore, no surprise that these properties attracted the attention of insdutry. In fact, many companies have already turned into profits some wonders of this materials. To mention just a few examples, CARDEA ZERO is a solid state drive developed by TEAMGROUP that boosts its performance thanks to graphene's heat capacity [27], the earphone company ANKER, released ZOLO earphones in the market, which uses the structural enhancing properties of graphene to improve the sound quality [28], and EMBERION incorporated graphene in some of its photodetectors to improve their sensitivity for night vision [29]. This carbon allotrope was even present in the last winter Olympiads, in the modality of skeleton, were participants used sleds by the company *Versarien* that were strengthened with graphene [30]. On a side note, a PhD student from Bath university won the bronze medal using one of them [31].

However, the impact of graphene has always sounded louder in fundamental science. It ignited the interest on two dimensional materials (see Fig. 1.0.1), like

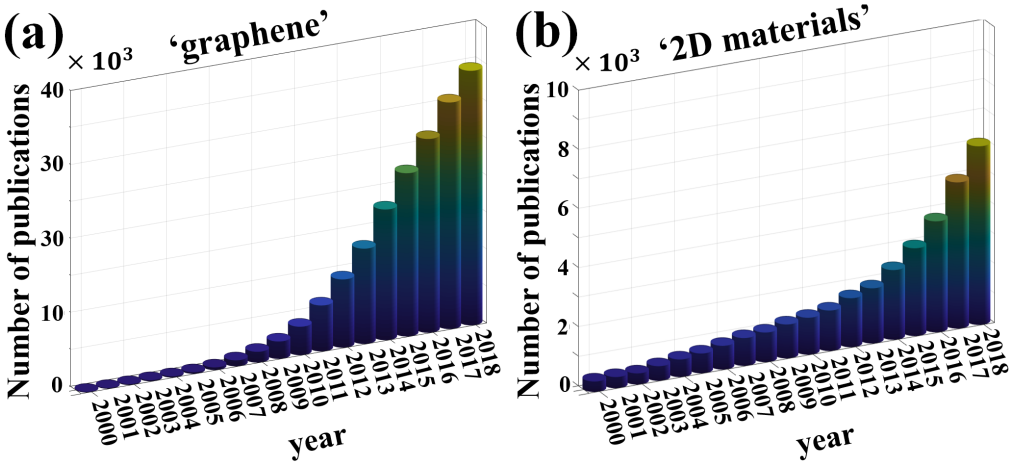

Figure 1.0.1: Data was obtained from the web `www.webofknowledge.com`. Histograms represent the number of articles published containing the word "graphene" and "2D materials". These two graphs highlight the correlation between the advent of graphene and the development of 2D materials.

hexagonal boron nitride or transition-metal dichalcogenides, which were mechanically exfoliated soon after graphene appeared on stage [32, 33]. Furthermore, stacking these layers gives rise a new class of materials, also known as van der Waals heterostructures [34]. Held together by the weak forces between consecutive layers, the transport and optical properties of these structures usually differ significantly from those of their constituent components. Additionally, the relative angle between these layers provides an extra degree of freedom that can be exploited [35]. In order to harness the full potential of these structures, therefore, characterisation of samples has become at least as important as their preparation.

It is precisely here where Raman spectroscopy comes into play. This technique is based on the Raman effect, discovered by Sir C. V. Raman in 1928 [36], and it consists of inelastic scattering of light after transferring or extracting energy from matter. The power of this technique relies on the fact that the physical processes by which a substance gains or loses energy are unique to that substance, hence, the detected light in a Raman experiment provides a fingerprint of it. Additionally, this technique is fast and non-invasive, which is widely acknowledged across different

disciplines, such as forensics [37], pharmacy [38] or nanoscience [39]. Graphene science has also taken the most of Raman [40], as the chemical selectivity of this spectroscopy has been used to study a myriad of structural changes in graphene and graphene materials. This fact is the starting point of our work.

This thesis aims to prove theoretically that the electronic properties of graphene materials can be studied using Raman spectroscopy. This relies on a type of Raman event, often referred to as *electronic Raman scattering*, that excites graphene by introducing one electron-hole pair, a purely electronic excitation. Therefore, graphene and Raman scattering in graphene, our two main characters, are introduced in the next two chapters. In each of the following three chapters, we introduce one member of the family of graphene materials, namely superconducting graphene, graphite and twisted bilayer graphene. We model their electronic Raman spectra, and predict the emergence of distinctive features, in close connection to their electronic properties. At the end of each chapter, we provide a brief description of the current experimental status, because we acknowledge that the outcome of a single experiment can always prove us wrong.

It always seems impossible until it is done

Nelson Mandela

2 Graphene

2.1 Graphene on paper

Because the properties of graphene are inherited by the individual carbon atoms that comprise it, the chemistry of carbon is the best starting point to describe graphene. Each carbon atom contains six electrons. The two electrons forming a closed $1s^2$ shell are effectively disconnected from the outside world, while the remaining four constitute the $2s^2\ 2p^2$ configuration. In crystals, however, the total energy decreases due to the overlap between the different electron wave functions, and the state of minimal energy is reached when the overlap between neighbouring electronic orbitals is maximal. In graphene, such energy gain is enough to promote one electron from the $2s$ state into a $2p$ state, resulting in the formation of three hybridized sp^2 orbitals confined in a plane, each carbon bond forming an angle of 120° between two neighbouring ones, at a distance $d \approx 1.42$Å. These orbitals are

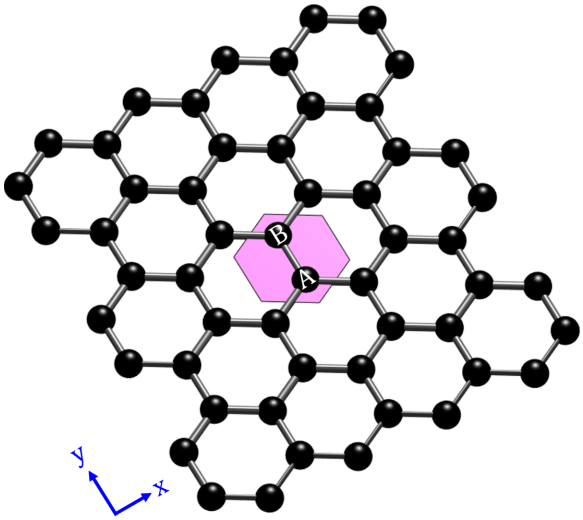

Figure 2.1.1: Pictorial representation of graphene and the unit cell, containing two atoms that belong to the triangular sub-lattices A and B. In our notation, zig-zag chain of the hexagones goes along the x-axis. The A atoms in such chain occupy the higher position in the y-axis.

responsible for the formation of the characteristic honeycomb lattice of graphene (Fig. 2.1.1), which can be regarded as two triangular Bravais lattices, often referred to as A and B sublattices, with lattice vectors

$$\boldsymbol{a}_1 = a\left(\frac{1}{2}, \frac{\sqrt{3}}{2}\right), \qquad \boldsymbol{a}_2 = a\left(-\frac{1}{2}, \frac{\sqrt{3}}{2}\right), \tag{2.1}$$

$a \approx 2.46$Å being the lattice constant. Each sublattice contributes with one atom in the unit cell, and the relative position between the A and B atoms is $\boldsymbol{d}_1 = (0, d)$. The remaining electron constitutes the p_z orbital, oriented perpendicular to the plane. The overlap between these orbitals in neighbouring sites is lower than that of sp^2 ones, which increases the energy of the p_z orbitals, and because these can accommodate two electrons, the lowest state energy is expected to have the three fully occupied sp^2 orbitals and one partially occupied p_z orbital that determines most of the transport and optical properties of graphene.

In this thesis, we employ the tight-binding model [4] to describe the electronic properties of graphene. The key assumption behind this model is in its name: each electron is assumed to be *tightly bound* to one atom, interacting weakly with its environment. Accordingly, the electronic wave function around each atom is very similar to that of an atomic orbital of a free carbon atom, in our case the p_z orbital, $\left|\psi_z(\boldsymbol{r})\right\rangle$. The Hamiltonian of graphene $\mathcal{H}$, couples nearest-neighbouring orbitals, allowing electrons to hop from one atomic site to one of the three nearest neighbouring atomic sites. This defines the so-called nearest neighbour coupling

$$\begin{aligned} \gamma_0 &= \left\langle \psi_z(\boldsymbol{r}-\boldsymbol{d}_i)\right| \mathcal{H} \left|\psi_z(\boldsymbol{r})\right\rangle \equiv \int \mathrm{d}\boldsymbol{r}\psi_z^*(\boldsymbol{r}-\boldsymbol{d}_i)\mathcal{H}\psi_z(\boldsymbol{r}), \qquad (2.2)\\ \boldsymbol{d}_i &= \mathcal{R}_{(i-1)\frac{2\pi}{3}}\boldsymbol{d}_1, \qquad i = 1,2,3, \end{aligned}$$

where $\mathcal{R}_\varphi$ denotes a clockwise rotation by an angle φ. While there is no consensus on the actual value of this hopping parameter, ab initio calculations suggest $\gamma_0 \approx -2.7$ eV [41], and such is the value chosen for the work we present in this thesis. By the same token, one can define the next-nearest neighbour hopping parameter

$$\begin{aligned} \gamma_n &= \left\langle \psi_z(\boldsymbol{r}-\boldsymbol{a}_j)\right| \mathcal{H} \left|\psi_z(\boldsymbol{r})\right\rangle \equiv \int \mathrm{d}\boldsymbol{r}\psi_z^*(\boldsymbol{r}-\boldsymbol{a}_j)\mathcal{H}\psi_z(\boldsymbol{r}), \qquad (2.3)\\ \boldsymbol{a}_j &= \mathcal{R}_{(j-1)\frac{\pi}{3}}\boldsymbol{a}_1, \qquad j = 1,\ldots,6. \end{aligned}$$

Recent experimental data suggested that the value of the hopping parameter above is $\gamma_n \approx 0.1\gamma_0$ [42]. At this point, we could use the p_z orbitals centred in each atomic site, $\left|\psi_z(\boldsymbol{r}-\boldsymbol{R})\right\rangle$, as the basis of our Hamiltonian. In fact, a similar procedure, known as linear combination of atomic orbitals (LCAO) [43], is used in chemistry to study molecules. In crystals, however, writing any Hamiltonian in such basis is not handy, since its dimension would be as big as the number of atoms in the crystal. Instead, we can define a basis that encompasses all atomic orbitals for each sublattice, built under the assumption that the value of any wavefunction at two points related by a translation of lattice vectors can only be different by a relative phase factor. This idea was developed by Bloch [44], and for graphene such

basis takes the form

$$\left|\varphi_{\lambda,\boldsymbol{k}}(\boldsymbol{r})\right\rangle = \sum_{\boldsymbol{R}} e^{i\boldsymbol{k}\cdot(\boldsymbol{R}+\Delta_\lambda)}\varphi_z(\boldsymbol{r}-\boldsymbol{R}-\Delta_\lambda). \tag{2.4}$$

Above, $\Delta_A = \boldsymbol{d}_1/2$ and $\Delta_B = -\boldsymbol{d}_1/2$ denote the position of the A and B atoms in the unit cell of graphene, respectively, and the sum over $\boldsymbol{R} = i\boldsymbol{a}_1 + j\boldsymbol{a}_2$ $(i, j \in \mathbb{Z})$ spans over all units cells in the lattice. For the sake of shortening the notation, we have omitted normalisation factors in the equation above, acknowledging that it introduces units of inverse length. We use the basis $\left\{\left|\varphi_{A,\boldsymbol{k}}(\boldsymbol{r})\right\rangle, \left|\varphi_{B,\boldsymbol{k}}(\boldsymbol{r})\right\rangle\right\}$ and construct the matrix elements of the Hamiltonian $\left\langle\varphi_{\lambda',\boldsymbol{k}}(\boldsymbol{r})\right| \mathcal{H} \left|\varphi_{\lambda,\boldsymbol{k}}(\boldsymbol{r})\right\rangle$ using the relations in Eqs. (2.2) and (2.3)

$$\mathcal{H}_G(\boldsymbol{k}) = \begin{pmatrix} \gamma_n f^n(\boldsymbol{k}) & \gamma_0 f(\boldsymbol{k}) \\ \gamma_0 f^*(\boldsymbol{k}) & \gamma_n f^n(\boldsymbol{k}) \end{pmatrix}, \tag{2.5}$$

$$f(\boldsymbol{k}) = \sum_{i=1}^{3} e^{i\boldsymbol{d}_i\boldsymbol{k}},$$

$$f^n(\boldsymbol{k}) = \sum_{j=1}^{6} e^{i\boldsymbol{a}_j\boldsymbol{k}}.$$

Notice that this simplification came with the cost of introducing a new variable, the wave number $\boldsymbol{k}$, which defines the reciprocal space. One important property of Bloch functions in Eq. (2.4) is their periodicity in $\boldsymbol{k}$ along the reciprocal lattice vectors $\boldsymbol{b}_1$ and $\boldsymbol{b}_2$, which satisfy $\boldsymbol{b}_i \cdot \boldsymbol{a}_j = 2\pi\delta_{i,j}$, and in graphene they are

$$\boldsymbol{b}_1 = \frac{2\pi}{a}\left(1, \frac{1}{\sqrt{3}}\right), \tag{2.6a}$$

$$\boldsymbol{b}_2 = \frac{2\pi}{a}\left(-1, \frac{1}{\sqrt{3}}\right). \tag{2.6b}$$

Therefore, it suffices to solve the Schrödinger equation, $\mathcal{H}(\boldsymbol{k})\left|\Psi(\boldsymbol{k})\right\rangle = \varepsilon_{\boldsymbol{k}}\left|\Psi(\boldsymbol{k})\right\rangle$,

for a finite number of $\boldsymbol{k}$ points satisfying

$$|\boldsymbol{k}| \leq \left| \boldsymbol{k} + \sum_{i,j} i\boldsymbol{b}_1 + j\boldsymbol{b}_2 \right|, \qquad i, j \in \mathbb{Z}. \tag{2.7}$$

This set of $\boldsymbol{k}$ points are closer to the origin of the reciprocal space (Γ point) than they are to any other reciprocal lattice points, and they define the first Brillouin zone (BZ). For graphene, it corresponds to the area enclosed by a regular hexagon centred at the Γ point with vertices at the $\boldsymbol{K}$ points,

$$\boldsymbol{K}_\xi = \xi \frac{4\pi}{3a} (1, 0), \tag{2.8a}$$

$$\boldsymbol{K}'_\xi = \xi \frac{4\pi}{3a} \left(\frac{-1}{2}, \frac{\sqrt{3}}{2} \right), \tag{2.8b}$$

$$\boldsymbol{K}''_\xi = \xi \frac{4\pi}{3a} \left(\frac{-1}{2}, \frac{-\sqrt{3}}{2} \right), \tag{2.8c}$$

with $\xi = \pm 1$. We now assume that the overlap between two neighbouring p_z orbitals is negligible. Therefore, Bloch functions orthonormal, $\left\langle \varphi_{\lambda,\boldsymbol{k}}(\boldsymbol{r}) \,\middle|\, \varphi_{\lambda',\boldsymbol{k}}(\boldsymbol{r}) \right\rangle = \delta_{\lambda,\lambda'}$, and the solutions to the Schrödinger equation are found by diagonalising the Hamiltonian in Eq. (2.5), which yields the band structure

$$\varepsilon_{\beta,\boldsymbol{k}} = \beta \left| \gamma_0 f(\boldsymbol{k}) \right| + \gamma_n f^n(\boldsymbol{k}). \tag{2.9}$$

In the equation above, the Greek letter β labels the conduction ($\beta = +1$) and the valence ($\beta = -1$) band. The dispersion of graphene, shown in Fig. 2.1.2a, consists of two bands, crossing at the corners of the Brillouin zone in (2.8). For neutral graphene, the lower (valence) band is fully filled, the upper (conduction) band is empty, with the Fermi level lying exactly at the crossing points. The conduction and valence bands are parabolic at the Γ point, and they contain saddle points between two neighbouring $\boldsymbol{K}$ points, also known as $\boldsymbol{M}$ points. As we will see along this thesis, these two features leave signatures in the electronic density of states (DoS), the momentum-integrated number of states within an energy win-

dow between E and $E + \mathrm{d}E$,

$$\mathcal{N}(E) = 2 \int \frac{\mathrm{d}\boldsymbol{k}}{(2\pi)^2} \delta(E - \varepsilon_{\beta,\boldsymbol{k}}), \tag{2.10}$$

where the factor of 2 accounts for the spin degeneracy. It can be shown that parabolic bands ($\varepsilon_{\boldsymbol{k}} = c_0 k^2$) give rise to steps in the DoS, while saddle points lead to sharp peaks, or van Hove singularities (vHSs) (Fig. 2.1.2b). We also observe that at the neutrality point (CNP), at $E = 0$, the DoS is linear. This is a consequence of one of the most distinctive hallmarks of graphene: its conical dispersion around the $\boldsymbol{K}$ points. To illustrate this, we expand the factors $f(\boldsymbol{k})$ and $f^n(\boldsymbol{k})$ around the corners $\boldsymbol{K}_\xi$,

$$f(\boldsymbol{p}) \approx \frac{\sqrt{3}a}{2\hbar} \left(-\xi p_x + i p_y\right), \tag{2.11a}$$

$$f^n(\boldsymbol{p}) \approx -3\gamma_n, \tag{2.11b}$$

where $\boldsymbol{p} \equiv \hbar\left(\boldsymbol{k} - \boldsymbol{K}_\xi\right)$ is the momentum measured from the $\boldsymbol{K}_\xi$ point. Notice that we only need to expand around these two points, as the other two corners in Eq. (2.8), $\boldsymbol{K}'_\pm = \boldsymbol{K}_\pm \pm \boldsymbol{b}_2$ and $\boldsymbol{K}''_\pm = \boldsymbol{K}_\pm \mp \boldsymbol{b}_1$, are equivalent points in reciprocal space. Inserting (2.11) in Eq. (2.5) results in the Hamiltonian

$$\mathcal{H}_{\mathrm{L}}(\boldsymbol{p}) = \begin{pmatrix} 0 & v\left(\xi p_x - i p_y\right) \\ v\left(\xi p_x + i p_y\right) & 0 \end{pmatrix}, \tag{2.12}$$

Above we rescale the energy to omit the on-site energy shift $-3\gamma_n$ in the diagonal terms, and define $v = \frac{\sqrt{3}a}{2\hbar}|\gamma_0| \sim 10^6 m/s$ as the Fermi velocity. Notice that the points $\boldsymbol{K}_+$ and $\boldsymbol{K}_-$, often referred to as valleys, are inequivalent, making valley index $\xi = \pm 1$ a good quantum number at energies around the charge neutrality point. The expression in Eq. (2.12) is often referred to as the Dirac Hamiltonian. This becomes apparent after the basis choice $\left\{ \left|\varphi^+_{A,\boldsymbol{p}}(\boldsymbol{r})\right\rangle, \left|\varphi^+_{B,\boldsymbol{p}}(\boldsymbol{r})\right\rangle, \left|\varphi^-_{B,\boldsymbol{p}}(\boldsymbol{r})\right\rangle, \right.$

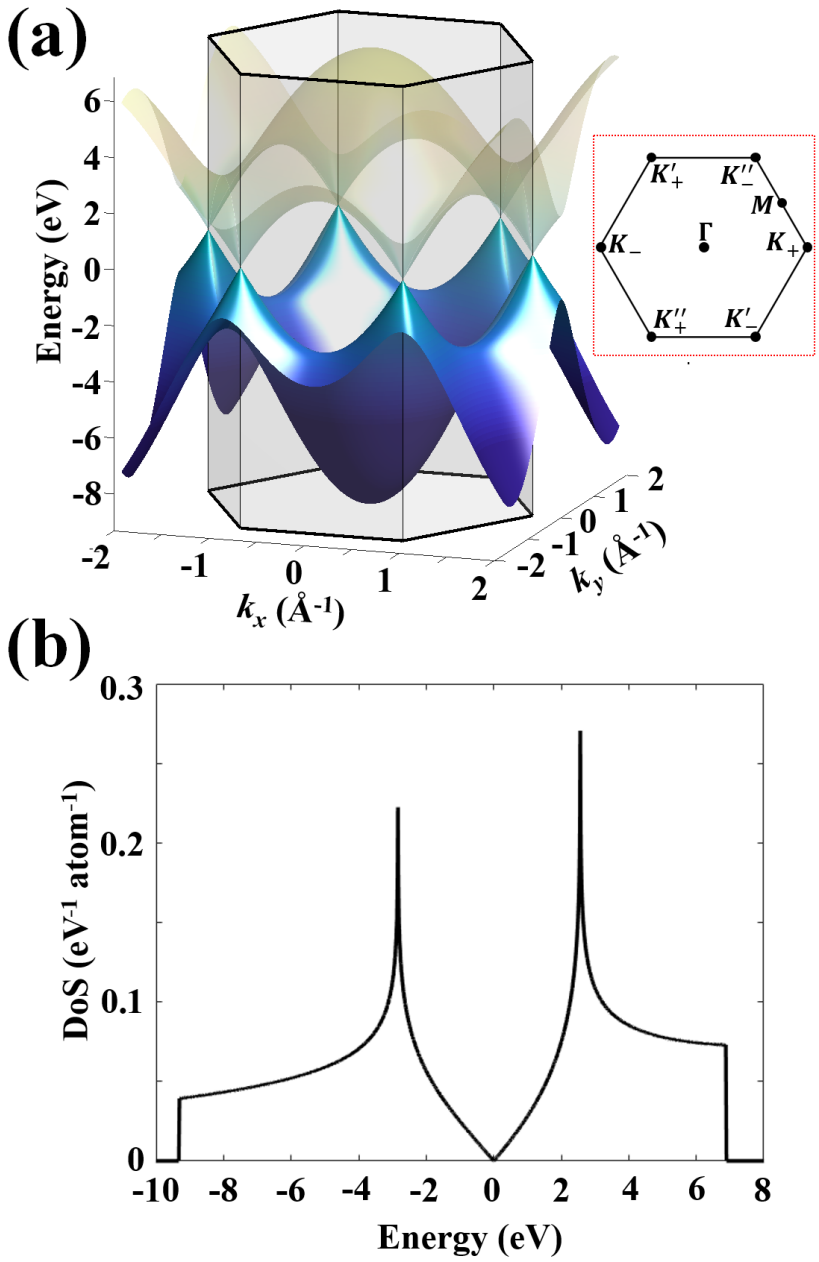

Figure 2.1.2: (a) Band structure of graphene, originated from p_z orbitals of carbon atoms, plotted in a $4\text{Å}^{-1} \times 4\text{Å}^{-1}$ square around the Γ point. The hexagonal prism represents the first Brillouin zone of graphene. We introduce transparency to the upper band to emphasise that it is empty for pristine graphene at $T = 0$ K. (b) Numerical density of states of graphene. The units of volume are chosen so that integrating over the whole energy range gives 1.

$-\left|\varphi^{-}_{A,\boldsymbol{p}}(\boldsymbol{r})\right\rangle\Big\}$, which rewrites Eq. (2.12) in the compact form

$$\mathcal{H}_{\mathrm{L}}(\boldsymbol{p}) = \tau_0 \otimes v\boldsymbol{p}\cdot\sigma, \tag{2.13}$$

$\sigma = (\sigma_x, \sigma_y)$ being the vector of Pauli matrices and τ_0 the 2×2 unit matrix in valley indices. This is formally the same Hamiltonian that Paul Dirac derived in the context of massless fermions with spin $1/2$ [45]. The eigenvalues and eigenvectors of such Hamiltonian read

$$\varepsilon_{\beta,\boldsymbol{p}} = \beta v p, \tag{2.14a}$$

$$\left|\Phi^{\xi}_{\beta,\boldsymbol{p}}(\boldsymbol{r})\right\rangle = \frac{1}{\sqrt{2}}\left(\left|\varphi^{\xi}_{A,\boldsymbol{p}}(\boldsymbol{r})\right\rangle + \xi\beta e^{i\xi\theta}\left|\varphi^{\xi}_{B,\boldsymbol{p}}(\boldsymbol{r})\right\rangle\right), \tag{2.14b}$$

$\beta = \pm 1$ and $\theta \equiv \arctan\left(p_y/p_x\right)$ being the band index and angle that the vector $\boldsymbol{p}$ forms with respect to the p_x-axis, respectively. Now inserting Eq. (2.14a) in Eq. (2.10), we find that the density of states around the CNP is indeed linear,

$$\mathcal{N}^{\mathrm{L}}(E) = 2\sum_{\xi,\beta}\int \frac{\mathrm{d}\boldsymbol{p}}{(2\pi\hbar)^2}\delta(E-\beta v p) = \frac{2E}{\pi\hbar^2 v^2}. \tag{2.15}$$

Throughout this thesis, we are going to employ the k dot p approximation [46], which allows us to express the complicated structure of the solutions in Eq. (2.14b) in terms of plane waves. Such approximation works under two assumptions: p_z orbitals in Eq. (2.4) are rapidly decaying functions that only take significant values around their centre, so that we can take $\exp\left[i\boldsymbol{k}(\boldsymbol{R}+\Delta_\lambda)\right] \approx \exp\left(i\boldsymbol{k}\boldsymbol{r}\right)$ in Eq. (2.4), and the spatial evolution of the Bloch basis is slow enough for momentum $\boldsymbol{k} \approx \boldsymbol{K}_\xi$ (a more thorough derivation can be found in [47]). With this approach, the complete solution for the time-dependent Schrödinger equation, around the $\boldsymbol{K}_\xi$ valley takes the form

$$\left|\Psi^{\xi}_{\beta,\boldsymbol{p}}(\boldsymbol{r},t)\right\rangle = \frac{1}{\sqrt{2}}\begin{pmatrix}1\\ \xi\beta e^{i\xi\theta}\end{pmatrix} e^{\frac{i}{\hbar}(\boldsymbol{r}\cdot\boldsymbol{p}-\varepsilon_{\beta,\boldsymbol{p}}t)}, \tag{2.16}$$

written in a 2-component basis that gives the electronic amplitude in the sublattice sites A and B.

We conclude this section by describing the second order corrections to the linear Hamiltonian in Eq. (2.12),

$$\mathcal{H}^{\mathrm{tw}}(\boldsymbol{p}) = \frac{v^2}{6\gamma_0}\boldsymbol{T}(\boldsymbol{p})\cdot\sigma, \tag{2.17a}$$

$$\mathcal{H}^{\mathrm{nn}}(\boldsymbol{p}) = -\frac{\gamma_n v^2}{2\gamma_0^2}p^2\sigma_0, \tag{2.17b}$$

where, for the sake of compacting the notation, we define $\boldsymbol{T}(\boldsymbol{p}) \equiv (p_y^2 - p_x^2, 2\xi p_x p_y)$. The first term is the so-called trigonal warping, and lowers the rotational symmetry of the linear dispersion to C_{3v}. Conversely, the second term corresponds to the parabolic dispersion, and while it keeps the $C_{\infty v}$ rotational symmetry of graphene dispersion, it introduces electron-hole asymmetry.

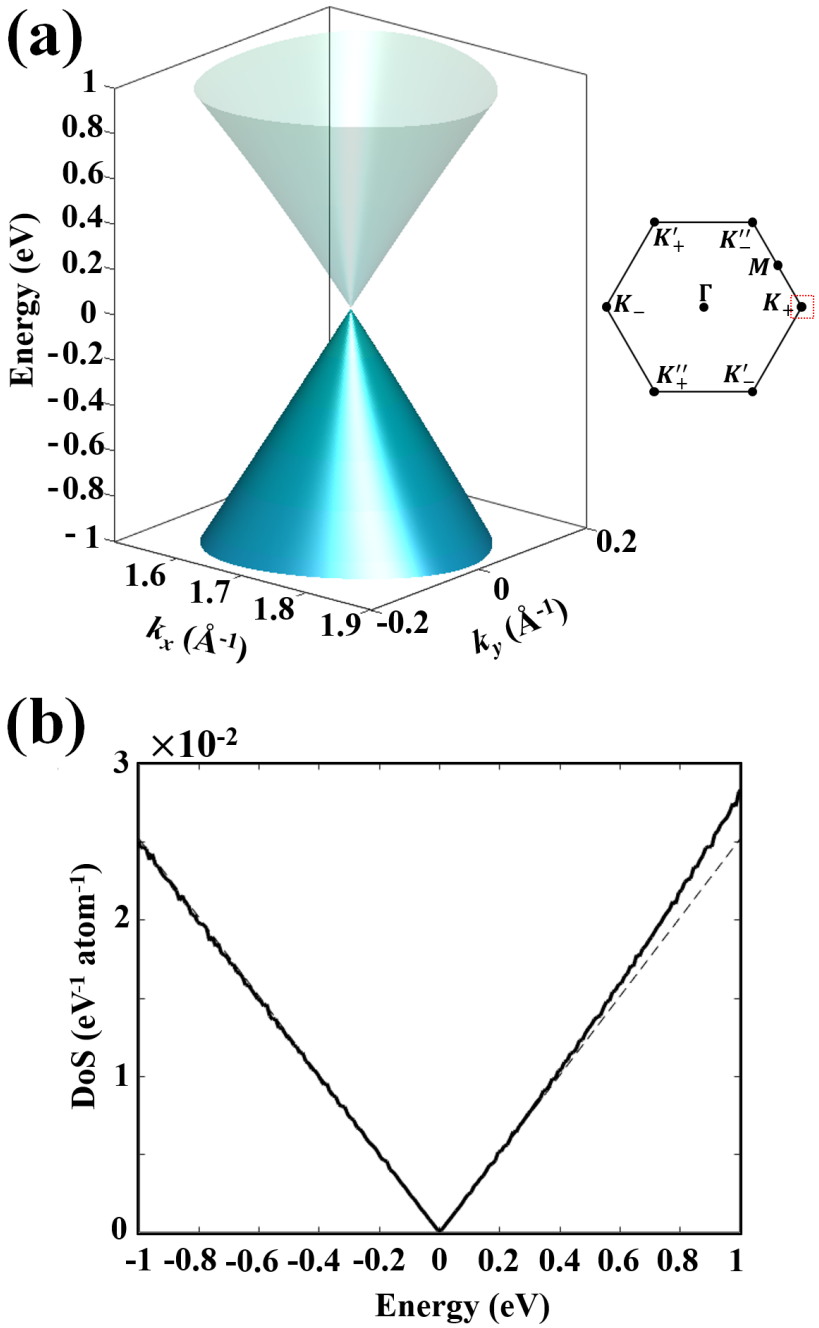

Figure 2.1.3: (a) Band structure of pristine graphene around a $4\text{Å}^{-1} \times 4\text{Å}^{-1}$ square centred at the $\boldsymbol{K}_+$ point. (b) Density of states using Eq. (2.10) (solid lines) and linearised dispersion obtained from Eq. (2.15) (dashed lines) of graphene around the charge neutrality point.

2.2 Graphene in the lab

The first mechanical exfoliation of graphene sounded like a starting pistol for many laboratories all around the world, where scientists devoted tireless efforts in the following years to characterise and understand this material with all available spectroscopic techniques. To this aim, atomic force microscope (AFM) was used to identify monolayers of graphene [13], while scanning tunnelling microscopy (STM) and transmission electron microscopy (TEM) were used to produce images of graphene with Angstrom resolution [48, 49]. Transport measurements were also performed to evidence the linear density of states around the charge neutrality point [50, 51], as well as to test the two important implications of Dirac equation, namely the perfect transmission through a voltage barrier, also known as Klein tunnelling [52–56], and the characteristic $\sqrt{N}$-discretisation of Landau levels under the application of a magnetic field in graphene observed through the anomalous quantum Hall effect [57–59] (see Fig. 2.2.2). Optical measurements are routinely employed to study and characterise graphene. As a matter of fact, optical absorption was used to identify the first exfoliated graphene layers on silicon oxide, which consistently absorb 2.3% of the incoming light [25], allowing us to determine the thickness of graphite up to a few layers. One of the most direct techniques to prove the band structure of graphene described in Fig. 2.1.2 is angle resolved photo-emission spectroscopy (ARPES), in which high energy photons impinge on graphene and eject electrons off the crystal based on the photoelectric effect. Even out of the sample, the motion of these electrons depend on the momentum they once had in the graphene, which allows us to reconstruct the band structure by changing the energy of the incident photons. Additionally, spectral weights in ARPES can be obtained with the electronic amplitudes in Eq. (2.16), a connection that has provided a deep understanding of graphene and graphene materials [60–62]. However, Raman spectrocopy is arguably one of the most popular non-invasive tools study graphene, due to its versatility, energy resolution, cost and effectiveness [63, 64]. This so acknowledged that almost every experimental paper on graphene or graphene materials contain at least one Raman spectrum. Owing

to the interest on this spectroscopic technique, the rest of this thesis aims to study features in the Raman spectrum of graphene-based systems from a theoretical perspective and connect them to fundamental properties of the band structure.

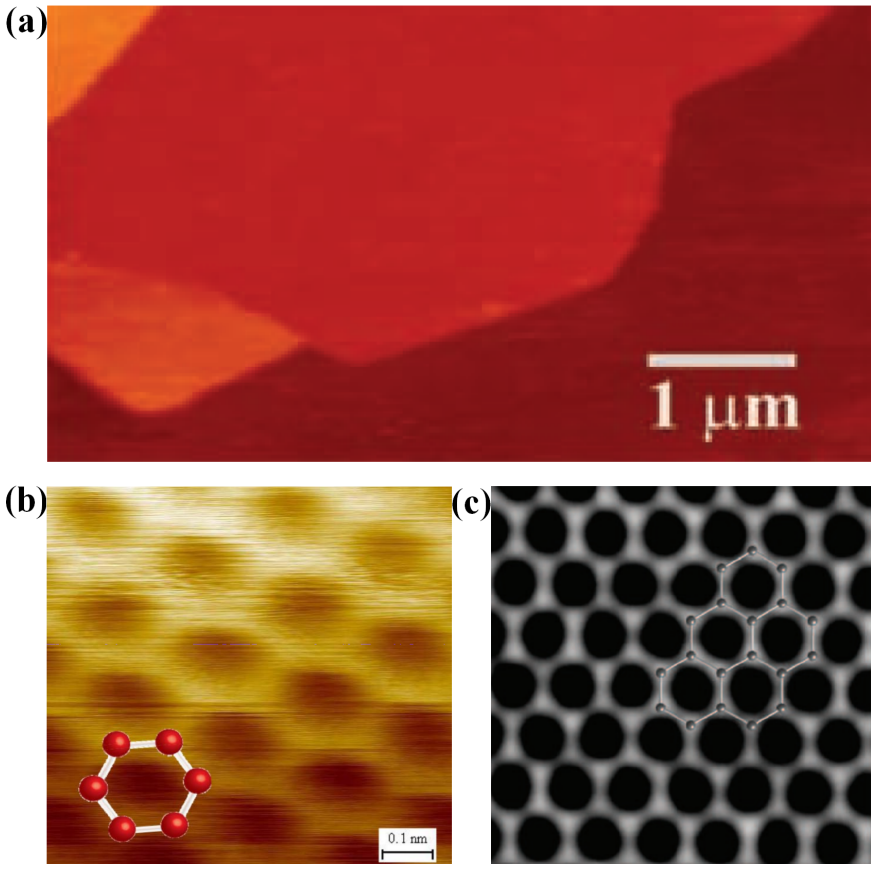

Figure 2.2.1: (a) Source: [13] Fig. 1c. The first reported image of monolayer graphene on silicon oxide taken with AFM. (b) Source: Fig.2b from [48]. Image of monolayer graphene taken with STM. (c) Image of monolayer graphene taken with TEM.

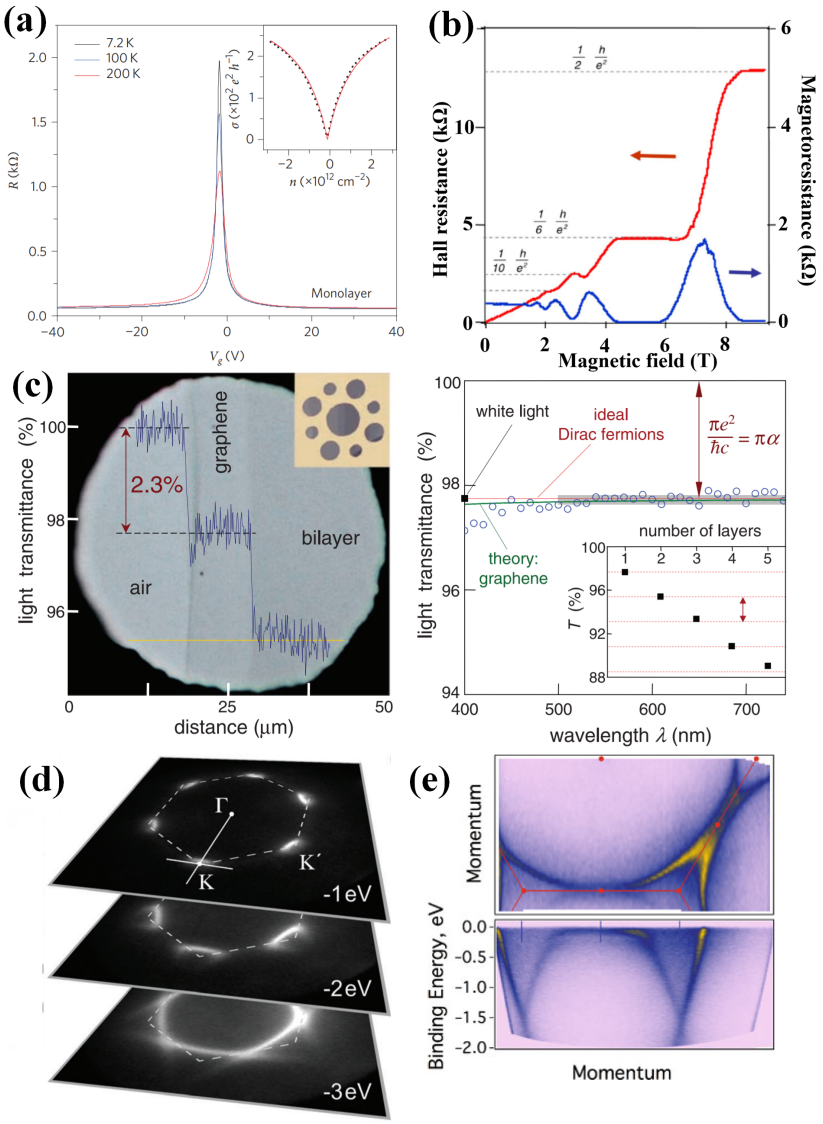

Figure 2.2.2: (a) Source: [50] Fig.3a. Resistance dependence on the applied gate voltage for graphene on boron nitride. The inset represents the conductivity versus the carrier concentration. (b) Source: [58] Fig.2. Quantised Hall resistance (red) and magentoresistance (blue) of graphene as a function of the applied magnetic field. (c) Source: [25] Fig.1. Optical absorption measurements on graphene. Authors reported the observation of monolayer graphene with the nake eye and the potential for optical absorption as a technique to count the number of layers in thin graphitic films. (d) Source: [65] Fig. 5b. ARPES measurements of graphene on germanium probing the valence band of graphene. (e) Source: [66] Fig. 1h. ARPES measurements of doped graphene to probe the conduction band.

Ask the right questions, and nature will open the doors to her secrets.

Chandrashekhara Venkata Raman

3

Electronic Raman scattering in graphene

Interaction with light is one of the main routes used by experimentalists to characterise and study graphene materials. To mention just a few examples, optical absorption allows us count the number of layers in graphitic films, from few layers down to monolayer [67], with X-ray diffraction we can determine the interlayer distance in graphite [68], photo-luminescence provides an estimate for the Fermi level [69], and angle resolved photo-emission spectroscopy (ARPES) has been used to study the effect of substrates on the band struture [70]. Amongst all the spectroscopic techniques, however, Raman spectroscopy has stood out remarkably as a formidable tool to study graphene [63]. This technique is based on the inelastic scattering of light, and was originally studied in molecules, as the scattered light provides a structural fingerprint of them: the energy difference between the incoming and outgoing photons is spent in exciting or de-exciting vibrational and/or rotational modes that change the polarisation of the molecule,

which are exclusive to each molecule. Unsurprisingly, this effect also appears in crystals, where the incoming light scatters inelastically by coupling with lattice vibrations (phonons) that change the charge distribution. Graphene, however, is centro-symmetric, and crystal vibrations cannot induce such change in polarization. Instead, the mechanism for Raman in graphene rely on electrons, which are coupled to both phonons and the electromagnetic field through the terms $\mathcal{V}_{\text{ph}}$ and $\mathcal{V}_{\text{em}}$, respectively. This, in turn, paves a unique way to study electrons in graphene, as analysed theoretically by Basko [71]. He derived the amplitude for a Raman process that results in the creation of n phonons,

$$\langle s_{\text{f}}| \mathcal{R} |s_{\text{i}}\rangle \sim \sum_{s_n,\cdots,s_1} \frac{\langle s_{\text{f}}| \mathcal{V}_{\text{em}} |s_{\text{n}}\rangle}{\varepsilon_{\text{f}} - \varepsilon_{\text{n}} - 2i\gamma} \cdot \frac{\langle s_{\text{n}}| \mathcal{V}_{\text{ph}} |s_{\text{n}-1}\rangle}{\varepsilon_{\text{n}} - \varepsilon_{\text{n}-1} - 2i\gamma} \cdots \frac{\langle s_2| \mathcal{V}_{\text{ph}} |s_1\rangle}{\varepsilon_2 - \varepsilon_1 - 2i\gamma} \cdot \frac{\langle s_1| \mathcal{V}_{\text{em}} |s_{\text{i}}\rangle}{\varepsilon_1 - \varepsilon_{\text{i}} - 2i\gamma}. \tag{3.1}$$

In this equation, γ stands for a phenomenological broadening of the electronic dispersion, and we use the short notation $|s_{\text{x}}\rangle$ to denote a quantum state in the crystal with energy ε_{x}. This amplitude describes a Raman process where an incoming photon interacts with an initial state, $|s_{\text{i}}\rangle$ (absence of phonons, a Fermi sea of electrons and one incoming photon), after which one electron in the valence band is promoted to the conduction band, characterising the first virtual state of the whole process, $|s_1\rangle$ (absence of photons and phonons, and a Fermi sea with an electron-hole pair). Then the system undergoes to n photonless virtual states, in each of them, one electron spends part of its energy in creating one phonon. Eventually, such electron recombines with a hole leaving behind n phonons in the crystal and one scattered photon. This is the final state, $|s_{\text{f}}\rangle$.

In pristine graphene, Eq. (3.1) describes two prominent features of the Raman spectrum, the G peak at $\sim$ 1580cm $^{-1}$, which originates from the creation of one phonon with zero momentum, and the 2D peak at $\sim$ 2460 cm^{-1}, which is the result of the creation of two phonons with momenta $\pm\boldsymbol{K}_+$, respectively [71]. In graphene materials, the connection between Eq. (3.1) and experimental Raman spectra provides a wealth of information about the samples: the number of layers in thin films of graphite can be determined by the ratio between the intensities of

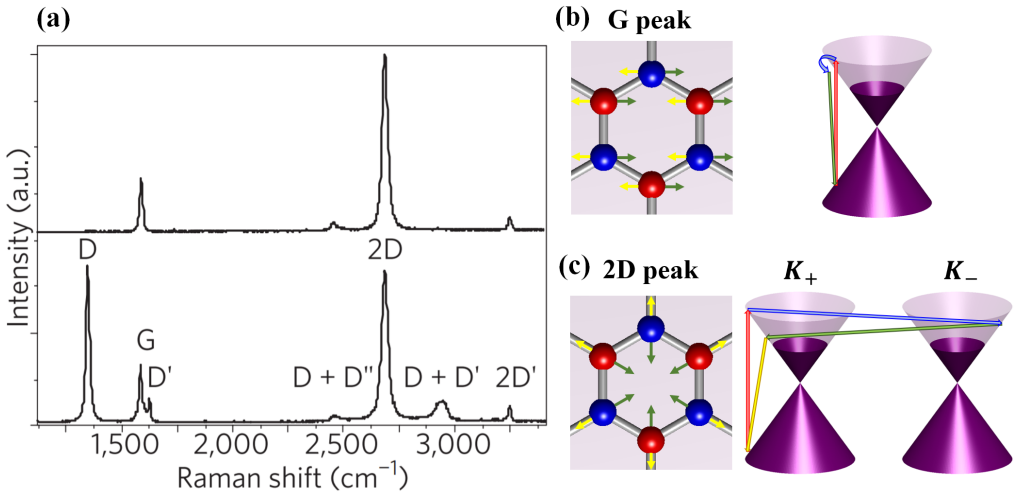

Figure 3.0.1: (a) Source: [63] Fig. 1e. Raman spectrum of graphene without (top) and with (bottom) impurities. (b) One vibrational mode responsible for the G peak, and representation of the three-steps process associated: creation of one electron-hole pair (red arrow), intravalley electron-phonon interaction (blue arrow) and recombination (green arrow). (c) One vibrational mode responsible for the 2D peak and representation of the four-steps process associated: creation of one electron-hole pair (red arrow), first intervalley electron-phonon interaction (blue arrow), second intervalley electron-phonon interaction (green arrow) and recombination (yellow arrow).

the G and the 2D peak [72], the strength of the electron-electron scattering can be obtained by experimental fitting of the parameter γ [73], the splitting of the G peak is a signature of strain in graphene [74], and the intensity of other Raman peaks at $\sim$ 1350 cm^{-1} (D peak) and at $\sim$ 1600 cm^{-1} (D$'$ peak) is a signature of defects in the sample, allowing us to estimate the impurity concentration [64] and even identify the type of impurity by comparing the different heights of the peaks in the Raman spectrum [75].

However, the idea that Raman shifts are solely caused by lattice vibrations, which has taken root among many experimentalists, does not provide a complete picture of the Raman effect. Another type of excitation in crystals, where the final state is an electron-hole pair, can also result in inelastic scattering of photons. This type

of Raman scattering, also known as electronic Raman scattering (ERS), was first theorised by P. Wolff in the sixties [76]. He introduced the time-dependent perturbation $\mathcal{V}_{\text{em}}$ in the Hamiltonian of a two-band semiconductor and computed the two leading terms in the perturbation expansion. The first order contribution accounts for processes where both incident and scattered photons are absorbed and emitted simultaneously, whereas in the second order contribution, these photons are absorbed and emitted at two different times. He concluded that the former is significantly stronger than the latter in semiconductors, and it leaves detectable signals in the Raman spectrum, which were experimentally confirmed [77–79]. Furthermore, because only electrons are involved in this type of scattering, these type of Raman signal provide an exceptional tool to extract direct information about electronic dispersions, such as band edges or the presence of vHSs.

Following previous works [80–82], we present in the next section the theory of electronic Raman scattering in graphene. We demonstrate that, contrary to what is observed in most semiconductors, the second-order contribution is larger than the first-order one. ERS signals are comparatively weaker than phonon-related ones in the Raman spectra, which makes their experimental observation a challenge. We provide a short description of the experimental work on ERS in graphene at the end of this chapter.

3.1 Theoretical description of ERS in graphene

To formulate the theory of ERS in monolayer graphene [80], which is the basis for the rest of the results in this thesis, we describe the interaction between graphene electrons and the photon field by constructing the canonical momentum,

$$\boldsymbol{P} = \boldsymbol{p} - e\boldsymbol{A}, \tag{3.2}$$

where e is the charge of the electron and $\boldsymbol{A}$ is the photon field,

$$\boldsymbol{A}(\boldsymbol{r}, t) = \sum_{\Omega, \boldsymbol{q}, q_z} \frac{\hbar}{\sqrt{2\varepsilon_0 \Omega}} \left(\boldsymbol{l} e^{\frac{i}{\hbar}(\boldsymbol{q}\cdot\boldsymbol{r} - \Omega t)} \hat{b}_{\boldsymbol{q}, q_z, \boldsymbol{l}} + h.c. \right), \tag{3.3}$$

Here, the operator $\hat{b}_{\boldsymbol{q},q_z,\boldsymbol{l}}$ ($\hat{b}^{\dagger}_{\boldsymbol{q},q_z,\boldsymbol{l}}$) annihilates (creates) a photon with in-plane momentum $\boldsymbol{q}$, out-of-plane momentum q_z and polarization $\boldsymbol{l} = (l_x, l_y)$, and Ω is the energy of the incident photon. Inserting the photon field in Eqs. (2.12) and (2.17) generates three leading perturbative terms,

$$\begin{aligned}
\mathcal{V}_{\mathrm{em}}(\boldsymbol{r},t) &= \mathcal{V}^{\mathrm{L}}_{\mathrm{em}}(\boldsymbol{r},t) + \mathcal{V}^{\mathrm{tw}}_{\mathrm{em}}(\boldsymbol{r},t) + \mathcal{V}^{\mathrm{nn}}_{\mathrm{em}}(\boldsymbol{r},t), \\
\mathcal{V}^{\mathrm{L}}_{\mathrm{em}}(\boldsymbol{r},t) &= -ve\ (\boldsymbol{A}(\boldsymbol{r},t)) \cdot \sigma, \\
\mathcal{V}^{\mathrm{tw}}_{\mathrm{em}}(\boldsymbol{r},t) &= \frac{e^2v^2}{6\gamma_{\mathrm{o}}} \boldsymbol{T}(\boldsymbol{A}(\boldsymbol{r},t)) \cdot \sigma, \\
\mathcal{V}^{\mathrm{nn}}_{\mathrm{em}}(\boldsymbol{r},t) &= -\frac{\gamma_n e^2v^2}{2\gamma_{\mathrm{o}}^2} |\boldsymbol{A}(\boldsymbol{r},t)|^2 \sigma_{\mathrm{o}}.
\end{aligned} \tag{3.4}$$

The first term in the equation above, inherited from the Dirac Hamiltonian in Eq. (2.12), is linear in the photon field, and is responsible for the optical absorption (and emission) in graphene. The second and third terms originate from the trigonal warping and the parabolic dispersion of graphene, respectively. Because they are quadratic in photon field, they participate in processes where two photons are absorbed and/or emitted simultaneously. These are the building blocks to evaluate the Raman amplitude for a process that turns $|s_{\mathrm{i}}\rangle$, a Fermi sea of electrons plus an incoming photon with energy Ω, momentum $(\boldsymbol{q}, q_z)$ and polarisation $\boldsymbol{l}$, into $|s_{\mathrm{f}}\rangle$, a Fermi sea of electrons with an electron-hole pair and one scattered photon with energy $\tilde{\Omega}$, momentum $(\tilde{\boldsymbol{q}}, \tilde{q}_z)$ and polarisation $\tilde{\boldsymbol{l}}$, in a time T. Using time-dependent perturbation theory [83], its general expression takes the form

$$\begin{aligned}
\langle s_{\mathrm{f}}| \mathcal{R} |s_{\mathrm{i}}\rangle = \sum_{n=1}^{\infty} \int_{-T/2}^{T/2} \frac{\mathrm{d}t_n}{i\hbar} \langle s_{\mathrm{f}}| \mathcal{V}_{\mathrm{em}}(\boldsymbol{r}_n, t_n) \sum_{\nu_{n-1}} |s_{\nu_{n-1}}\rangle \langle s_{\nu_{n-1}}| \cdots \\
\int_{-T/2}^{t_3} \frac{\mathrm{d}t_2}{i\hbar} \mathcal{V}_{\mathrm{em}}(\boldsymbol{r}_2, t_2) \sum_{\nu_1} |s_{\nu_1}\rangle \langle s_{\nu_1}| \int_{-T/2}^{t_2} \frac{\mathrm{d}t_1}{i\hbar} \mathcal{V}_{\mathrm{em}}(\boldsymbol{r}_1, t_1) |s_{\mathrm{i}}\rangle .
\end{aligned} \tag{3.5}$$

For each n in the sum above, the electromagnetic potential $\mathcal{V}_{\mathrm{em}}$ interacts n times with the quantum state in graphene, to connect the initial and final quantum states. Between two consecutive interactions, the system evolves with a virtual quantum

state of the unperturbed Hamiltonian of graphene. The expression in Eq. (3.5) for large n is exceedingly complicated. However, the entire approach relies on the quick convergence of the sum, which we can truncate at $n = 2$. The term in the sum above corresponding to $n = 1$, also known as the contact interaction, accounts for processes where the emission and absorption take place at a given time t, and have the following mathematical expression

$$
\begin{aligned}
\langle s_f| \mathcal{R}^c |s_i\rangle =& \frac{1}{i\hbar}\int_{-\frac{T}{2}}^{+\frac{T}{2}} dt \,\langle s_f| \left(\mathcal{V}_{em}^{tw}(\boldsymbol{r},t) + \mathcal{V}_{em}^{nn}(\boldsymbol{r},t)\right)|s_i\rangle = \qquad (3.6)\\
=& \frac{1}{2i\hbar}\frac{\hbar^2 e^2}{2\varepsilon_o\sqrt{\Omega\tilde{\Omega}}}\int_{-\frac{T}{2}}^{+\frac{T}{2}} dt e^{\frac{i}{\hbar}(\tilde{\Omega}-\Omega+\varepsilon_e-\varepsilon_h)t}\int d\boldsymbol{r} e^{\frac{i}{\hbar}(\boldsymbol{p}_h-\boldsymbol{p}_e+\boldsymbol{q}-\tilde{\boldsymbol{q}})\cdot\boldsymbol{r}}\\
&\times\left[\frac{v^2}{6\gamma_o}\begin{pmatrix}1 & \xi\beta_e e^{-i\xi\theta_e}\end{pmatrix}\begin{pmatrix}0 & L_-\tilde{L}_-^*\\ L_+\tilde{L}_+^* & 0\end{pmatrix}\begin{pmatrix}1\\ \xi\beta_h e^{i\xi\theta_h}\end{pmatrix}\right.\\
&\left.-\frac{\gamma_n v^2}{\gamma_o^2}\begin{pmatrix}1 & \xi\beta_e e^{-i\xi\theta_e}\end{pmatrix}\begin{pmatrix}\boldsymbol{l}\cdot\tilde{\boldsymbol{l}} & 0\\ 0 & \boldsymbol{l}\cdot\tilde{\boldsymbol{l}}\end{pmatrix}\begin{pmatrix}1\\ \xi\beta_h e^{i\xi\theta_h}\end{pmatrix}\right] =\\
=& \frac{\hbar^2 e^2}{2\varepsilon_o\sqrt{\Omega\tilde{\Omega}}}\frac{\sin\left[(\varepsilon_e-\varepsilon_h-\omega)\frac{T}{2\hbar}\right]}{\varepsilon_e-\varepsilon_h-\omega}\delta\left(\frac{\boldsymbol{p}_h-\boldsymbol{p}_e+\boldsymbol{q}-\tilde{\boldsymbol{q}}}{\hbar}\right)\\
&\times\left\{\frac{\xi v^2}{6\gamma_o}\left[L_-\tilde{L}_-^*\beta_h e^{i\xi\theta_h}+L_+\tilde{L}_+^*\beta_e e^{-i\xi\theta_e}\right]\right.\\
&\left.-\frac{\gamma_n v^2}{\gamma_o^2}\left(1+\beta_h\beta_f e^{i\xi(\theta_h-\theta_e)}\right)\boldsymbol{l}\cdot\tilde{\boldsymbol{l}}\right\},
\end{aligned}
$$

where we define $\omega \equiv \Omega - \tilde{\Omega}$, write $L_\pm = l_x \pm i l_y$ and $\tilde{L}_\pm^* = \tilde{l}_x^* \pm i\tilde{l}_y^*$ to compact the notation, and introduce the subscripts "e" and "h" to the energy ε, momentum $\boldsymbol{p}$, band index β and angle $\theta = \arctan(p_y/p_x)$ of the electron and the hole in the final state, respectively. In contrast, the term corresponding to $n = 2$ accounts for processes where emission and absorption happen at two different times and in any

order, which reads

$$\langle s_i|\,\mathcal{R}^{L}\,|s_f\rangle = \sum_{\nu}\int_{-\frac{T}{2}}^{+\frac{T}{2}}\frac{dt_2}{i\hbar}\langle s_f|\,\mathcal{V}^{L}_{em}(\boldsymbol{r}_2,t_2)\,|s_\nu\rangle\int_{-\frac{T}{2}}^{t_2}\frac{dt_1}{i\hbar}\langle s_\nu|\,\mathcal{V}^{L}_{em}(\boldsymbol{r}_1,t_1)\,|s_i\rangle \tag{3.7}$$

$$= \frac{-e^2v^2}{8\varepsilon_o\sqrt{\Omega\tilde{\Omega}}}\sum_{\nu}\int_{-\frac{T}{2}}^{\frac{T}{2}}dt_2 e^{\frac{i}{\hbar}(\varepsilon_e+\tilde{\Omega}-\varepsilon_\nu)t_2}\int_{-\frac{T}{2}}^{t_2}dt_1 e^{\frac{i}{\hbar}(\varepsilon_\nu-\Omega-\varepsilon_h)t_1}\delta\left(\frac{\boldsymbol{p}_h-\boldsymbol{p}_e+\boldsymbol{q}-\tilde{\boldsymbol{q}}}{\hbar}\right)$$

$$\begin{pmatrix}1 & \xi\beta_e e^{-i\theta_e}\end{pmatrix}\begin{pmatrix}0 & \tilde{L}^*_-\\ \tilde{L}^*_+ & 0\end{pmatrix}\begin{pmatrix}1\\ \xi\beta_\nu e^{i\theta_\nu}\end{pmatrix}\begin{pmatrix}1 & \xi\beta_\nu e^{-i\theta_\nu}\end{pmatrix}\begin{pmatrix}0 & L_-\\ L_+ & 0\end{pmatrix}\begin{pmatrix}1\\ \xi\beta_h e^{i\theta_h}\end{pmatrix} +$$

$$\frac{-e^2v^2}{8\varepsilon_o\sqrt{\Omega\tilde{\Omega}}}\sum_{\nu}\int_{-\frac{T}{2}}^{\frac{T}{2}}dt_2 e^{\frac{i}{\hbar}(\varepsilon_e-\Omega-\varepsilon_\nu)t_2}\int_{-\frac{T}{2}}^{t_2}dt_1 e^{\frac{i}{\hbar}(\varepsilon_\nu+\tilde{\Omega}-\varepsilon_h)t_1}\delta\left(\frac{\boldsymbol{p}_h-\boldsymbol{p}_e+\boldsymbol{q}-\tilde{\boldsymbol{q}}}{\hbar}\right)$$

$$\begin{pmatrix}1 & \xi\beta_e e^{-i\theta_e}\end{pmatrix}\begin{pmatrix}0 & L_-\\ L_+ & 0\end{pmatrix}\begin{pmatrix}1\\ \xi\beta_\nu e^{i\theta_\nu}\end{pmatrix}\begin{pmatrix}1 & \xi\beta_\nu e^{-i\theta_\nu}\end{pmatrix}\begin{pmatrix}0 & \tilde{L}^*_-\\ \tilde{L}^*_+ & 0\end{pmatrix}\begin{pmatrix}1\\ \xi\beta_h e^{i\theta_h}\end{pmatrix}.$$

We introduce ε_ν and β_ν to denote the energy and band index of the the virtual electronic state, respectively, and $\theta_\nu = \arctan(p_{\nu,y}/p_{\nu,x})$, with $\boldsymbol{p}_\nu = (p_{\nu,x}, p_{\nu,y})$ being the momentum of the virtual electronic state. Expressions in Eqs. (3.6) and (3.7) represent the amplitude for any type of ERS event that leaves an electron-hole excitation in monolayer graphene. For pristine graphene at zero Kelvin, electrons populate completely the valence band, leaving empty its conduction counterpart. In that case, the only possible ERS excitations result from electronic transitions from the valence band to the conduction band (inter-band transition), shown in Fig. 3.1.1. When the conduction band is partially filled or the valence band is partially depleted, the Fermi level is shifted from the Dirac point by μ, and inter-band transitions with an energy lower than 2μ are forbidden, due to the Pauli blocking. This opens the door for the formation of electron-hole pairs within the same band (intra-band transitions), depicted in Fig. 3.1.3. Because these two types of electronic transitions lead to different spectral features, and the mathematical treatment is slightly different, we analyse them separately in the following two sections.

3.1.1 Inter-band transitions

Inter-band electronic transitions result in one hole in the valence band and one electron in the conduction band. Consequently, the band indices in Eqs. (3.6) and (3.7) are $\beta_h = -1$ and $\beta_e = +1$. In the following calculation we are going to consider that photons essentially carry no in-plane momentum and, therefore, electronic transitions are vertical ($\boldsymbol{p}_h = \boldsymbol{p}_e$). Such approximation is justified because the ratio between the momenta of the photons and the momenta of the electrons involved in the Raman process is about $\frac{\Omega/c}{\varepsilon/v} \sim \frac{1}{30}$. The contact interaction contributes to the Raman amplitude as

$$\begin{aligned}\langle s_f|\,\mathcal{R}^c\,|s_i\rangle =& \frac{\hbar^2 e^2}{2\varepsilon_o\sqrt{\Omega\tilde{\Omega}}}\frac{\sin\left[(\varepsilon_e-\varepsilon_h-\omega)\frac{T}{2\hbar}\right]}{\varepsilon_e-\varepsilon_h-\omega}\delta\left(\frac{\boldsymbol{p}_h-\boldsymbol{p}_e+\boldsymbol{q}-\tilde{\boldsymbol{q}}}{\hbar}\right) \\ &\times\left\{\frac{\xi v^2}{6\gamma_o}\left[-L_-\tilde{L}_-^* e^{i\xi\theta_h}+L_+\tilde{L}_+^* e^{-i\xi\theta_e}\right]-\frac{\gamma_n v^2}{\gamma_o^2}\left(1-e^{i\xi(\theta_h-\theta_e)}\right)\boldsymbol{l}\cdot\tilde{\boldsymbol{l}}\right\}\approx \\ \approx& i\frac{\hbar^2 e^2 v^2}{6\gamma_o\varepsilon_o\Omega}\frac{\sin\left[(\varepsilon_e-\varepsilon_h-\omega)\frac{T}{2\hbar}\right]}{\varepsilon_e-\varepsilon_h-\omega}\left[(l_x\tilde{l}_x^*-l_y\tilde{l}_y^*)\sin(\theta)+(l_x\tilde{l}_y^*+l_y\tilde{l}_x^*)\cos(\theta)\right].\end{aligned} \tag{3.8}$$

In the two-steps processes, an electron is annihilated in the valence band and another is created in the conduction ($\beta_v = +1$) band at t_1. At a later time t_2, either this electron is annihilated and another one in created in the conduction band (Fig. 3.1.1a) or an electron in the valence band fills the vacant state left by the first one in the valence band (Fig. 3.1.1b). The incoming photon can be absorbed either at t_1 or at t_2, and the outgoing photon is emitted at t_2 or at t_2, respectively. Therefore, the time integrals in Eq. (3.7) generate the factors

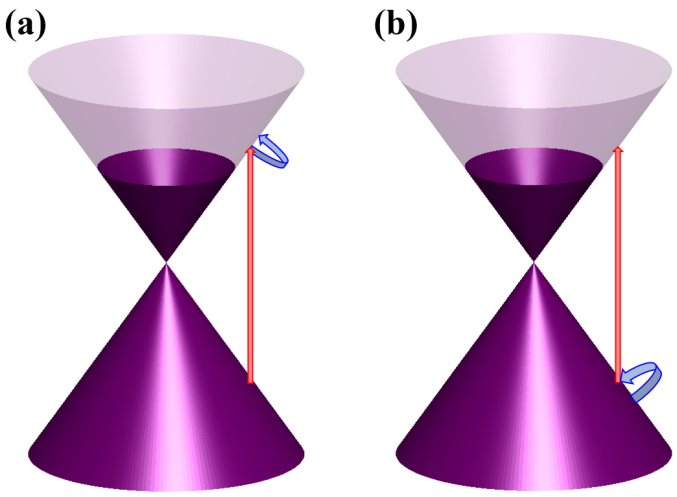

Figure 3.1.1: Inter-band two-steps process. The red and blue arrows represent an electronic transition ocurring at a time t_1 and t_2, respectively. The intermediate state of the system is a Fermi sea of electrons with an electron-hole pair. The photon absorption/emission (not shown) happens at t_1 or t_2.

$$\mathcal{I}_v^{\mathrm{a}} = \left(\frac{i}{\hbar}\right)^2 \int_{-\frac{T}{2}}^{\frac{T}{2}} \int_{-\frac{T}{2}}^{t_2} dt_2 dt_1 e^{\frac{i}{\hbar}(\varepsilon_e - \varepsilon_v + \tilde{\Omega})t_2} e^{\frac{i}{\hbar}(\varepsilon_v - \Omega - \varepsilon_h)t_1} \tag{3.9a}$$

$$= \int_{-\frac{T}{2}}^{\frac{T}{2}} dt_2 e^{\frac{i}{\hbar}(\varepsilon_e - \varepsilon_v + \tilde{\Omega})t_2} \frac{e^{\frac{i}{\hbar}(\varepsilon_v - \Omega - \varepsilon_v)t_2}}{\frac{i}{\hbar}(\varepsilon_v - \Omega - \varepsilon_h - i\delta^+)}$$

$$= \frac{2i\hbar^2}{\varepsilon_v - \Omega - \varepsilon_h - i\delta^+} \frac{\sin\left[(\varepsilon_c - \varepsilon_h - \omega)\frac{T}{2\hbar}\right]}{\varepsilon_e - \varepsilon_h - \omega}$$

$$\mathcal{I}_v^{\mathrm{e}} = \left(\frac{i}{\hbar}\right)^2 \int_{-\frac{T}{2}}^{\frac{T}{2}} \int_{-\frac{T}{2}}^{t_2} dt_2 dt_1 e^{\frac{i}{\hbar}(\varepsilon_e - \varepsilon_v - \Omega)t_2} e^{\frac{i}{\hbar}(\varepsilon_v + \tilde{\Omega} - \varepsilon_h)t_1} \tag{3.9b}$$

$$= \int_{-\frac{T}{2}}^{\frac{T}{2}} \frac{dt_2}{\hbar^2} e^{\frac{i}{\hbar}(\varepsilon_e - \varepsilon_v - \Omega)t_2} \frac{e^{\frac{i}{\hbar}(\varepsilon_v + \tilde{\Omega} - \varepsilon_h)t_2}}{\frac{i}{\hbar}(\varepsilon_v + \tilde{\Omega} - \varepsilon_h - i\delta^+)}$$

$$= \frac{-2i}{\varepsilon_v + \Omega - \varepsilon_e - i\delta^+} \frac{\sin\left[(\varepsilon_e - \varepsilon_h - \omega)\frac{T}{2\hbar}\right]}{\varepsilon_e - \varepsilon_h - \omega}.$$

The superscripts above "a" ("e") corresponds to the terms where the absorption (emission) take place at a time t_1. The energy scales in our problem allow us to per-

form another approximation. Raman spectroscopy typically uses lasers of incident light in the visible spectrum, with energies of the order of $\Omega \sim 2$ eV, while most common Raman features appear at energy shifts one order of magnitude smaller, like the G peak ($\omega_G \approx 0.2$ eV). Therefore, we can expand these factors as

$$\mathcal{I}_v^{\mathrm{a}} \approx \frac{2i}{\Omega}\left(1+\frac{\varepsilon_v-\varepsilon_{\mathrm{h}}}{\Omega}\right)\frac{\sin\left[\left(\varepsilon_{\mathrm{e}}-\varepsilon_{\mathrm{h}}-\omega\right)\frac{T}{2\hbar}\right]}{\varepsilon_{\mathrm{e}}-\varepsilon_{\mathrm{h}}-\omega} \tag{3.10a}$$

$$\mathcal{I}_v^{\mathrm{e}} \approx \frac{-2i}{\Omega}\left(1+\frac{\varepsilon_{\mathrm{e}}-\varepsilon_v}{\Omega}\right)\frac{\sin\left[\left(\varepsilon_{\mathrm{e}}-\varepsilon_{\mathrm{h}}-\omega\right)\frac{T}{2\hbar}\right]}{\varepsilon_{\mathrm{e}}-\varepsilon_{\mathrm{h}}-\omega}. \tag{3.10b}$$

We now take the leading contribution in the round brackets, and the amplitude for the two-steps processes can be rewritten as

$$\begin{aligned}\langle s_{\mathrm{f}}|\,\mathcal{R}^{\mathrm{L}}\,|s_{\mathrm{i}}\rangle =& \frac{2i}{\Omega}\frac{\hbar^2e^2v^2}{\varepsilon_0\sqrt{\Omega\tilde{\Omega}}}\frac{\sin\left[\left(\varepsilon_{\mathrm{e}}-\varepsilon_{\mathrm{h}}-\omega\right)\frac{T}{2\hbar}\right]}{\varepsilon_{\mathrm{e}}-\varepsilon_{\mathrm{h}}-\omega}\delta\left(\frac{\boldsymbol{p}_{\mathrm{h}}-\boldsymbol{p}_{\mathrm{e}}}{\hbar}\right)\begin{pmatrix}1 & \xi e^{-i\xi\theta_{\mathrm{e}}}\end{pmatrix} \\ &\times\left[\begin{pmatrix}0 & \tilde{L}_-^*\\ \tilde{L}_+^* & 0\end{pmatrix}\begin{pmatrix}0 & L_-\\ L_+ & 0\end{pmatrix}-\begin{pmatrix}0 & L_-\\ L_+ & 0\end{pmatrix}\begin{pmatrix}0 & \tilde{L}_-^*\\ \tilde{L}_+^* & 0\end{pmatrix}\right]\begin{pmatrix}1\\ -\xi e^{i\xi\theta_{\mathrm{h}}}\end{pmatrix}\approx \\ \approx& \frac{\xi\hbar^2e^2v^2}{\varepsilon_0\Omega^2}\frac{\sin\left[\left(\varepsilon_{\mathrm{c}}-\varepsilon_{\mathrm{v}}-\omega\right)\frac{T}{2\hbar}\right]}{\left(\varepsilon_{\mathrm{c}}-\varepsilon_{\mathrm{v}}-\omega\right)/2}\begin{pmatrix}1 & \xi e^{-i\xi\theta}\end{pmatrix}\sigma_z\begin{pmatrix}1\\ -\xi e^{i\xi\theta}\end{pmatrix}\left(\tilde{l}_y^*l_x-\tilde{l}_x^*l_y\right)= \\ =& \frac{\xi\hbar^2e^2v^2}{\varepsilon_0\Omega^2}\frac{\sin\left[\left(\varepsilon_{\mathrm{c}}-\varepsilon_{\mathrm{v}}-\omega\right)\frac{T}{2\hbar}\right]}{\left(\varepsilon_{\mathrm{c}}-\varepsilon_{\mathrm{v}}-\omega\right)/2}\left(\boldsymbol{l}\times\tilde{\boldsymbol{l}}^*\right)_z.\end{aligned} \tag{3.11}$$

Notice that the ket-bra structure $\sum_v |s_v\rangle\langle s_v|$ in between the photon fields generates the identity between the two photon fields in Eq. (3.7), and because they contain σ_x and σ_y matrices, their commutator naturally generates the third Pauli matrix, σ_z. In semiconductors lacking spinor structure, the same procedure leads to the commutator of two scalars in Eq. (3.11), which gives zero. This is the reason why contact interaction dominates ERS in most semiconductors [76].

In order to obtain the Raman probability per unit of time, $w(\omega,\tilde{\boldsymbol{q}})$, we compute the amplitude squared and take the limit $T\to\infty$. As in Fermi's golden rule [84], this operation generates a Delta in energy, together with the factor $2\pi/\hbar$. Integrat-

ing such expression over all possible electronic excitations yields

$$
\begin{aligned}
w(\omega, \tilde{\boldsymbol{q}}) = \sum_{\xi,\sigma} \lim_{T\to\infty} \frac{1}{T} \int \frac{\mathrm{d}\boldsymbol{p}}{(2\pi\hbar)^2} \left| \langle s_\mathrm{f}| \, \mathcal{R}^\mathrm{c}_\mathrm{em} + \mathcal{R}^\mathrm{L}_\mathrm{em} \, |s_\mathrm{i}\rangle \right|^2 = \qquad (3.12)\\
= 4\frac{\hbar^4 e^4 v^4}{\varepsilon_\mathrm{o}^2 \Omega^2} \left(\frac{1}{\Omega^2} \Xi_\mathrm{s} + \frac{1}{2(6\gamma_\mathrm{o})^2} \Xi_\mathrm{o} \right) \int \frac{2\pi p \, \mathrm{d}p}{(2\pi\hbar)^2} f_\mathrm{h}(1 - f_\mathrm{e}) \frac{2\pi}{\hbar} \delta(\varepsilon_\mathrm{e} - \varepsilon_\mathrm{h} - \omega) = \\
= \frac{\hbar e^4 v^2}{\varepsilon_\mathrm{o}^2 \Omega^2} \left(\frac{1}{\Omega^2} \Xi_\mathrm{s} + \frac{1}{2(6\gamma_\mathrm{o})^2} \Xi_\mathrm{o} \right) \omega \, \Theta(\omega - 2\mu),
\end{aligned}
$$

Above, the filling factors for the conduction (f_e) and valence (f_h) band, which were introduced ad hoc, originate from the evaluation of the bra-ket after the construction of the electron field in second quantisation, omitted here to shorten the notation. At $T = 0$ K this leads to Pauli blocking of excitations $< 2\mu$, which is captured by the Heavyside function $\Theta(\omega - 2\mu)$. The polarisation factors,

$$
\Xi_\mathrm{s} = |\boldsymbol{l} \times \tilde{\boldsymbol{l}}^*|^2, \qquad (3.13a)
$$

$$
\Xi_\mathrm{o} = 1 + (\boldsymbol{l} \times \boldsymbol{l}^*) \cdot (\tilde{\boldsymbol{l}} \times \tilde{\boldsymbol{l}}^*), \qquad (3.13b)
$$

determine the intensities with respect to the polarisation of the incident beam and detected light. In terms of circular polarisation, the factor Ξ_s (Ξ_o) is 1 when the polarisations of the incoming and outgoing photons are the same (opposite) and 0 otherwise. In terms of linear polarisation, the term Ξ_s (Ξ_o) is 1 for processes when the polarisation of the scattered light is perpendicular (parallel) to the polarisation of the incoming beam.

Although the expression in Eq. (3.12) does not depend on $\tilde{\boldsymbol{q}}$ after the assumption of negligible photon momentum, w formally expresses the angle-resolved ERS probability per unit of time. In contrast, the angle-integrated probability per unit

of time divided by the incoming photon flux represents the spectral density

$$g(\omega) = \frac{1}{c}\int \frac{\mathrm{d}\tilde{\boldsymbol{q}}\mathrm{d}\tilde{q}_z}{(2\pi\hbar)^3}\, w(\omega)\,\delta\left(\tilde{\Omega} - c\sqrt{\tilde{\boldsymbol{q}}^2 + q_z^2}\right) = \tag{3.14}$$
$$= \left(\frac{e^2}{\varepsilon_0 2\pi\hbar c}\frac{v}{c}\right)^2 \omega\,\Theta(\omega - 2\mu)\left(\frac{1}{\Omega^2}\Xi_s + \frac{1}{2(6\gamma_0)^2}\Xi_0\right).$$

In Fig. 3.1.2 we present the theoretical plots at zero temperature. Finally, we estimate the number of ERS events per incoming photon, or quantum efficiency I, by integrating the expression above over a range of Raman shifts. For neutral graphene, the quantum efficiency for ERS processes that results in Raman shifts below $\omega_0 \approx 0.2$ eV is

$$I = \int_0^{\omega_0} \mathrm{d}\omega g(\omega) \approx \left(\frac{e^2}{\varepsilon_0 2\pi\hbar c}\frac{v}{c}\right)^2 \frac{\omega_0^2}{2\Omega^2} \sim 10^{-12}. \tag{3.15}$$

3.1.2 Intra-band transitions

In this type of electron transitions, the electron and hole state belong to the same band, which is only possible when the Fermi level μ is shifted from the CNP. We are going to consider that the Fermi level is in the conduction band, such that band indices of the electron and hole are $\beta_e = \beta_h = +1$. Considering that the momentum transfer from the photon to the electron is negligible, we have $\theta_e \approx \theta_h$. Notice that, under this approximation, the final state is a Fermi sea with one scattered photon with energy $\tilde{\Omega} = \Omega$, polarisation $\tilde{\boldsymbol{l}}$ and momentum $(\tilde{\boldsymbol{q}}, \tilde{q}_z)$. Introducing these changes in Eq. (3.6) gives

$$\langle s_f|\,\mathcal{R}^c_{em}\,|s_i\rangle = \frac{\hbar^2 e^2}{2\varepsilon_0\sqrt{\Omega\tilde{\Omega}}}\frac{\sin\left[(\varepsilon_e - \varepsilon_h - \omega)\frac{T}{2\hbar}\right]}{\varepsilon_e - \varepsilon_h - \omega}\delta\left(\frac{\boldsymbol{p}_h - \boldsymbol{p}_e}{\hbar}\right) \tag{3.16}$$
$$\times\left\{\frac{\xi\beta v^2}{3\gamma_0}\left[(-l_x\tilde{l}_x^* + l_y\tilde{l}_y^*)\sin\theta + (l_x\tilde{l}_y^* + l_y\tilde{l}_x^*)\cos\theta\right] - \frac{2\gamma_n v^2}{\gamma_0^2}\boldsymbol{l}\cdot\tilde{\boldsymbol{l}}^*\right\}.$$

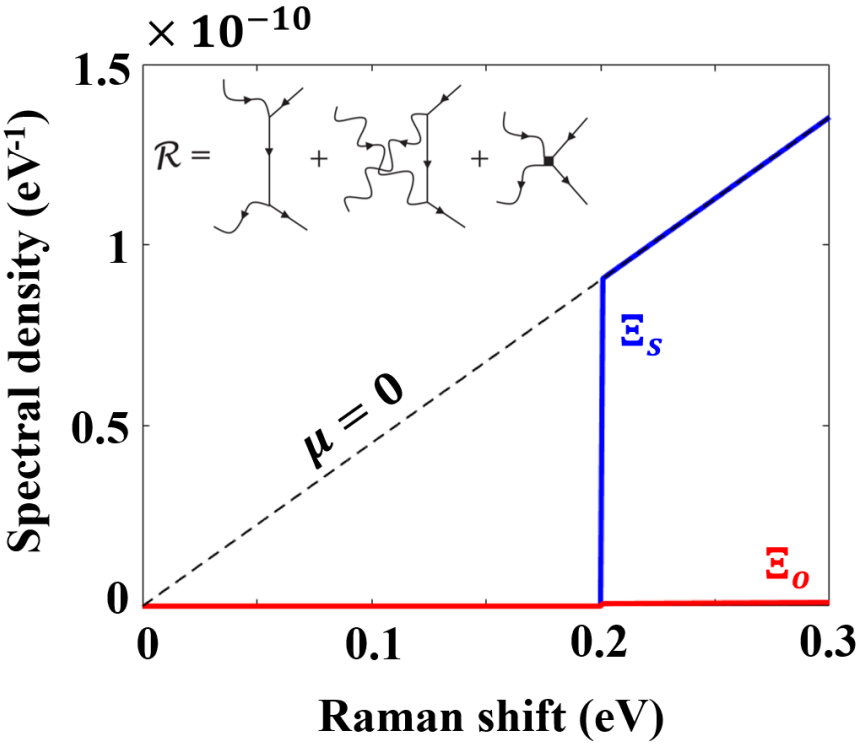

Figure 3.1.2: ERS Spectral density of graphene, with Fermi level $\mu = 0.1$ eV and incident photon energy $\Omega = 2$ eV, in cross-linear (blue) and parallel-linear polarisation (red). In black dashed line, we represent the spectral density in graphene with $\mu = 0$ eV in cross-linear polarisation, to highlight the spectral loss due to the Pauli blocking. The inset presents the two contributions to the ERS in terms of Feynman diagrams. The first two diagrams correspond to two-steps processes and is proportional to Ξ_s, while the third diagram to the contact interaction and is proportional to Ξ_o.

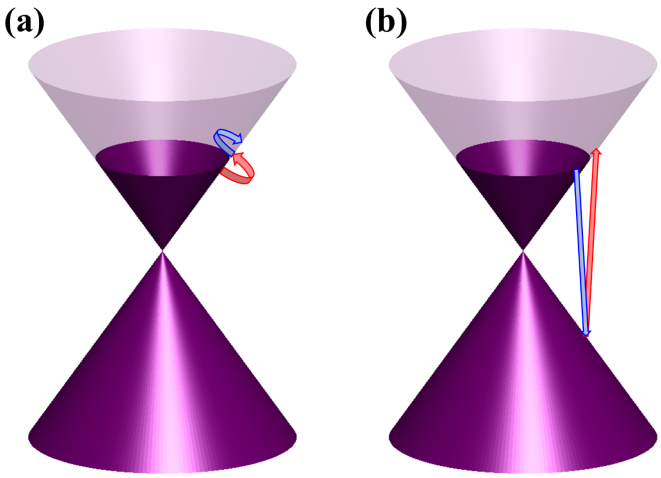

Figure 3.1.3: Intra-band two-steps process. The red and blue arrows represent the annihilation and destruction of an electron at a time t_1 and t_2, respectively. In each step, one electron is annihilated and created at the verge of the Fermi $+\mu$ (a), or at $-\mu$ and $+\mu$ in the valence and conduction bands. The photon absorption/emission (not shown) happens at t_1 or t_2.

Computing the contribution from the contact interaction to the ERS amplitude for intraband transitions, therefore, only requires to change the band index of the hole. In contrast, to compute the contribution to the ERS amplitude from the two-steps processes, we also need to change the two possible intermediate virtual states $|s_v\rangle$ in Eq. (3.7), as depicted in Fig. 3.1.3. The time integrals in Eq. (3.9) generate prefactors similar to those in the round brackets of Eqs. (3.10). Inserting the first constant term, 1, into Eq. (3.11), we obtain a factor proportional to $(1\xi e^{-i\xi\theta})\sigma_z(1\xi e^{-i\xi\theta})^\dagger = 0$. Conversely, inserting the second term generates factors proportional to $(\varepsilon_e - \varepsilon_h)/\Omega = 0$ and $2\mu/\Omega$, in the two processes depicted by Figs.

3.1.3a and 3.1.3b, respectively. Introducing these values in Eq. (3.7) yields

$$
\begin{aligned}
\langle s_f|\,\mathcal{R}^{L}\,|s_i\rangle = &+\frac{2i}{2\mu-\Omega}\frac{\hbar^2e^2v^2}{2\varepsilon_o\sqrt{\Omega\tilde{\Omega}}}\frac{\sin\left[(\varepsilon_e-\varepsilon_h-\omega)\frac{T}{2\hbar}\right]}{\varepsilon_e-\varepsilon_h-\omega} \\
&\times\begin{pmatrix}1 & -\xi e^{-i\xi\theta}\end{pmatrix}\begin{pmatrix}0 & \tilde{L}_-^*\\ \tilde{L}_+^* & 0\end{pmatrix}\begin{pmatrix}1\\ \xi e^{i\xi\theta}\end{pmatrix}\begin{pmatrix}1 & \xi e^{-i\xi\theta}\end{pmatrix}\begin{pmatrix}0 & L_-\\ L_+ & 0\end{pmatrix}\begin{pmatrix}1\\ -\xi e^{i\xi\theta}\end{pmatrix} \\
&+\frac{2i}{2\mu+\tilde{\Omega}}\frac{\hbar^2e^2v^2}{2\varepsilon_o\sqrt{\Omega\tilde{\Omega}}}\frac{\sin\left[(\varepsilon_e-\varepsilon_h-\omega)\frac{T}{2\hbar}\right]}{\varepsilon_e-\varepsilon_h-\omega} \\
&\times\begin{pmatrix}1 & -\xi e^{-i\xi\theta}\end{pmatrix}\begin{pmatrix}0 & L_-\\ L_+ & 0\end{pmatrix}\begin{pmatrix}1\\ \xi e^{i\xi\theta}\end{pmatrix}\begin{pmatrix}1 & \xi e^{-i\xi\theta}\end{pmatrix}\begin{pmatrix}0 & \tilde{L}_-^*\\ \tilde{L}_+^* & 0\end{pmatrix}\begin{pmatrix}1\\ -\xi e^{i\xi\theta}\end{pmatrix} \\
\approx&\frac{4i\mu\hbar^2e^2v^2}{\varepsilon_o\Omega^3}\frac{\sin\left[(\varepsilon_e-\varepsilon_h-\omega)\frac{T}{2\hbar}\right]}{(\varepsilon_e-\varepsilon_h-\omega)/2} \\
&\times\left[\boldsymbol{l}\cdot\tilde{\boldsymbol{l}}^*-\cos(2\theta)(\tilde{l}_x^*l_x-\tilde{l}_y^*l_y)-\sin(2\theta)(\tilde{l}_x^*l_y+\tilde{l}_y^*l_x)\right].
\end{aligned}
\tag{3.17}
$$

As in the previous section, we derive the Raman probability for each electronic transition at $\boldsymbol{p}$ summing amplitudes from contact interaction and two-steps processes, and taking the limit $T\to\infty$. We then integrate all of them over all possible $\boldsymbol{p}$ to extract the angle-resolved Raman probability,

$$
\begin{aligned}
w(\omega) =&\sum_{\xi,\sigma}\lim_{T\to\infty}\frac{1}{T}\int\frac{d\boldsymbol{p}}{(2\pi\hbar)^2}\left|\langle s_f|\,\mathcal{R}_{em}^{c}+\mathcal{R}_{em}^{L}\,|s_i\rangle\right|^2= \\
=&\frac{4\hbar e^4v^4}{\varepsilon_o^2\Omega^2}\int p\,dp\,f_h(1-f_e)\delta(\varepsilon_e-\varepsilon_h-\omega) \\
&\times\left\{\left[\left(\frac{4\mu}{\Omega^2}\right)^2+\left(\frac{\gamma_n}{\gamma_o^2}\right)^2\right]\Xi_s'+\left[\frac{1}{2}\left(\frac{4\mu}{\Omega^2}\right)^2+\frac{1}{2}\left(\frac{1}{6\gamma_o}\right)^2\right]\Xi_o\right\},
\end{aligned}
\tag{3.18}
$$

where, following the notation in [85], we introduce the polarisation factor

$$
\Xi_s' = |\boldsymbol{l}\cdot\tilde{\boldsymbol{l}}^*|^2. \tag{3.19}
$$

The filling factors in Eq. (3.18) are not well defined, as both electrons and holes line on the edge of the Fermi sea at $T=0$ K. Therefore, the integral on p cannot be

evaluate unless we relax the condition of no momentum transfer. This was already calculated in [80], where authors claimed that such consideration would result in a small peak at $\omega < \Omega v/c$, the quantum efficiency of which is around $I \sim 10^{-15}$. Such value is about three orders of magnitude smaller than the Raman signal coming from inter-band transitions, and it would contribute to a very small peak at zero energy in Fig. 3.1.2. However, we will use the result in Eq. (3.18) in chapter 3, as the opening of a gap around the Fermi level allows vertical transitions with a finite Raman shift.

3.2 Experimental evidence for ERS in graphene

To conclude this chapter, we put the theoretical work above in its experimental context. Firstly, to study how strong these signals are, and therefoe, how feasible it is to measure them, we need to compare the quantum efficiency associated to ERS with that of a manifestly detectable feature in graphene. In particular, D. Basko gave the estimate $I_G \sim 10^{-11}$ for the quantum efficiency of the G peak [71], about one order of magnitude greater than the quantum efficiency for inter-band transitions, a difference that is largely due to the strongly off-resonant nature of ERS signals [80]. Additionally, ERS signals are spread over a broad range of frequencies, rather than being concentrated in peaks, which makes experimental confirmation of ERS a challenge.

In 2011 the first confirmation of ERS was reported, under a magnetic field [86], a technique often referred to as *magneto-Raman* [87]. The application of a magnetic field leads to the discretisation of the dispersion of graphene in Landau levels [88], which effectively concentrates the linear ERS signal that originates from inter-band transitions in a set of peaks, as shown in Fig. 3.2.1 in graphene and graphite. The dependence of the position of the resulting peaks on the magnetic field, alongside with the change in intensity with the polarisation, revealed that these features were electronic in nature. Without magnetic fields, it is also possible to explore ERS signals. In [90], they probe these excitations by tracking the

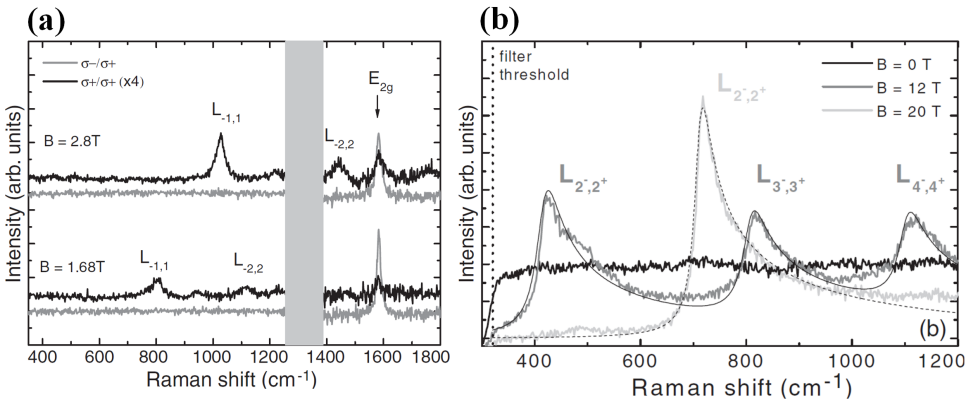

Figure 3.2.1: (a) Source [86] Fig. 4. Polarisation-resolved Raman spectra of graphene in the presence of two different magnetic fields. This figure, showing two purely electronic transitions between Landau levels, was the first confirmation of ERS in graphene. (b) Source [89] Fig. 2 b. ERS in bluk graphite in the presence of different magnetic fields.

ERS signal loss upon the application of a gate voltage. They observed intensity depletion in an energy range $\sim$ 0.35 eV under the application of a gate voltage, which is a signature of Pauli blocking (Fig. 3.2.2). Even without gating graphene, it is possible to observe ERS. In [91], the authors reported a linear trend in the spectra of monolayer graphene in cross linear configuration, which unambiguously identifies these type of excitations as ERS. Interestingly, they also reported the emergence of a peak at $\sim$ 10 meV after annealing the sample, shown here in Fig. 3.2.3. They claimed that the opening of a gap around the Fermi level enables the intra-band transitions responsible for such feature in the spectrum, and concluded that Raman has the potential to study gaps in the dispersion of graphene. This statement inspired the first project in this thesis, devoted to study spectral changes under the presence of a superconducting gap in graphene.

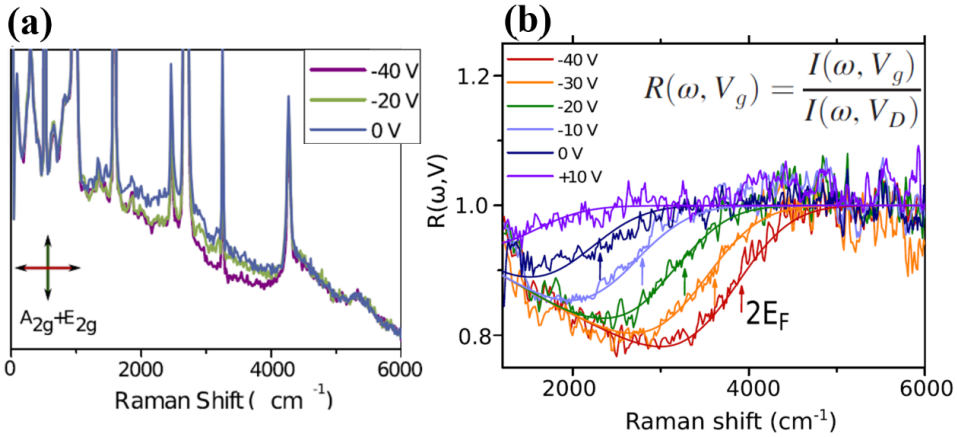

Figure 3.2.2: Source: [90] Figs. 1 and 2.(a) Raman spectra of graphene in cross-linear polarisation for three different gate voltages. As the gate voltage decreases, the Fermi level μ shifts to lower levels in the valence band and we observe Pauli blocking ERS for energies $\omega < 2\mu$. (b) highlights such spectral loss by comparing the ratio between Raman spectra with different gate voltages and the Raman spectrum with $\mu = 0$. All the spectra were measured at T=30 K.

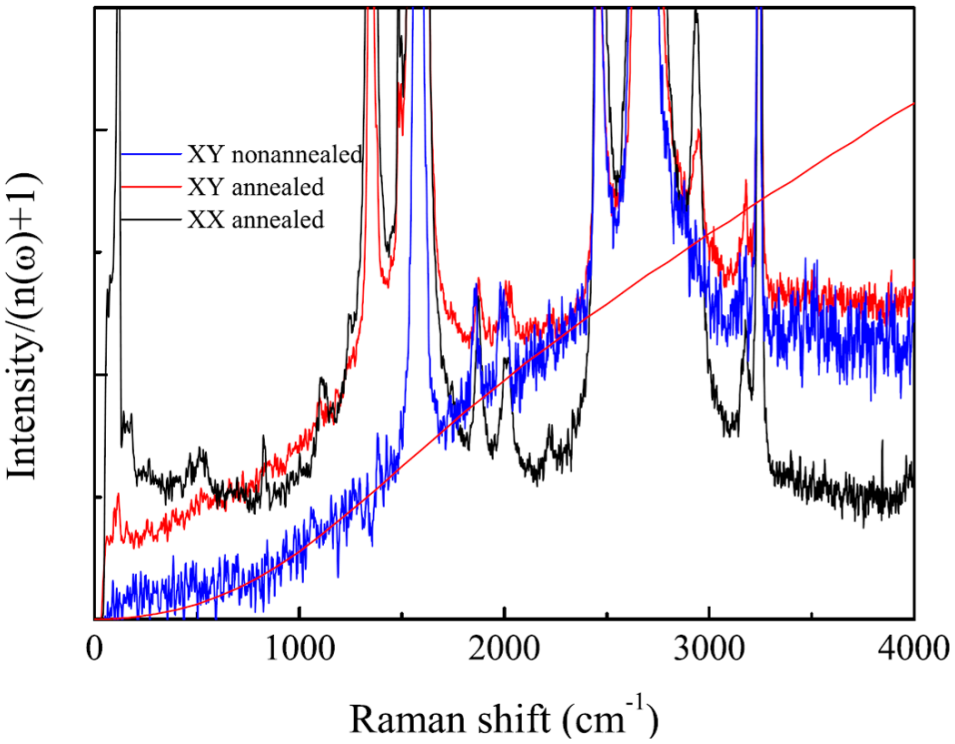

Figure 3.2.3: Source [91] Fig. 6. Raman spectra of graphene on cobalt in cross and parallel linear polarisation. The theoretical ERS signal of graphene in solid red line ($\mu = 60$ meV and $T = 300$ K) matches the experiment in the range of our approximation $\omega < 0.3$ eV. Here ERS is observed without gate voltage or applying a magnetic field.

An ounce of action is worth a ton of theory

Ralph Waldo Emerson

4

Electronic Raman scattering in superconducting graphene

For the modest price of a layer of carbons, graphene offers a zoo of interesting properties. Yet among them, one is notably missing in pristine graphene: superconductivity. This phenomenon, discovered in 1911 by H.K. Onnes, typically originates from electron-phonon coupling, which introduces a weak effective attraction between any two electrons with opposite spins and momenta [92], often referred to as Cooper pairs. Below a critical temperature T_c, where such interaction dominates thermal fluctuations, a superconducting order emerges and the material features zero resistance and perfect diamagnetism [93]. In pristine graphene, superconductivity is not present due to its vanishing density of states at the CNP.

However, a huge potential for applications, relying on the combined physics of Dirac electrons and Cooper pairs, could be unlocked inducing superconduc-

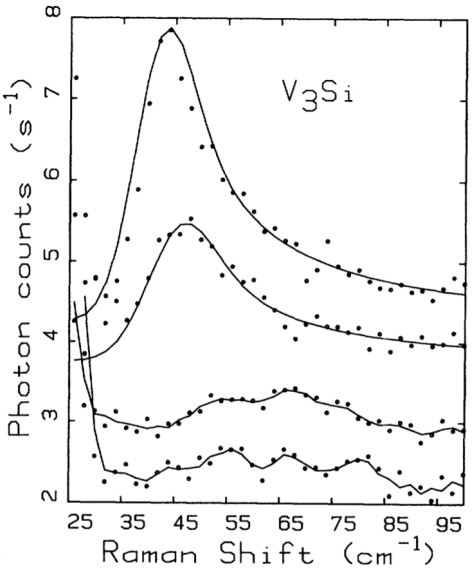

Figure 4.0.1: Source: [100] Fig. 6. Raman spectra of V_3Si measured at 1.8 K (upper two curves) and at 40 K (lower two curves). The peak of the top two curves is a signature for a superconducting order.

tivity in graphene. A few applications proposed in the literature include devices that measure valley-polarised currents [94], nano-meter scale transistors [95] or logic gates for quantum computers [96]. These applications have triggered a significant research output aimed to induce superconductivity in graphene, which was achieved by proximity [95], and doping graphene with alkali metals [97–99]. In all these cases, they employed invasive spectroscopies to study the superconducting order, such as tunnelling spectroscopy, or sophisticates techniques like ARPES, or superconducting quantum interference device (SQUID) magnetometers, that often require expensive equipment.

On the other hand, experimentalists have measured superconducting gaps in materials using electronic Raman scattering for almost 50 years [100–107]. In some cases, a peak was observed in the low energy Raman spectra providing experimental evidences for a superconducting order and valuable information, such as the size of the gap or even the type of superconductivity. However, this tech-

nique, to the best of our knowledge, has not been employed in superconducting graphene, and the present chapter aims to cover the theory. In the next section, we introduce a BCS-like pairing interaction in the Hamiltonian in Eq. (2.12). Such order induces an isotropic gap in the Dirac dispersion, around the Fermi surface. As a consequence, the Raman spectrum features a peak, the position of which gives insight into the superconducting order, and its shape is proportional to the density of states around the Fermi level. We conclude this chapter with some comments on the feasibility of its experimental detection.

4.1 Superconductivity in graphene

In this section, we follow previous works to describe superconductivity in graphene [108]. The best framework to study interacting systems like superconductivity is the second quantization [109], which has not been introduced yet and therefore, such formalism is the starting point of our discussion. The second-quantised version of the Hamiltonian in Eq. (2.5), including all electrons in graphene and shifted away from the CNP by μ, is written as

$$\hat{\mathcal{H}}_{\mathrm{G}} = \sum_{\boldsymbol{k},\sigma} \left[\gamma_{\mathrm{o}} \left(f(\boldsymbol{k}) \hat{c}^{\dagger}_{A,\boldsymbol{k},\sigma} \hat{c}_{B,\boldsymbol{k},\sigma} + h.c. \right) + \sum_{L=A,B} \left(\gamma_n f^n(\boldsymbol{k}) - \mu \right) \hat{c}^{\dagger}_{L,\boldsymbol{k},\sigma} \hat{c}_{L,\boldsymbol{k},\sigma} \right] . \tag{4.1}$$

The operators above $\hat{c}_{L,\boldsymbol{k},\sigma}$ ($\hat{c}^{\dagger}_{L,\boldsymbol{k},\sigma}$) annihilates (creates) an electron in a state given by a Bloch wave function of Eq. (2.4), belonging to lattice site L ($L = A, B$), and they obey the anti-commutation rules

$$\left\{ \hat{c}^{\dagger}_{L,\boldsymbol{k},\sigma}, \hat{c}_{L',\boldsymbol{k}',\sigma'} \right\} = \hat{c}^{\dagger}_{L,\boldsymbol{k},\sigma} \hat{c}_{L',\boldsymbol{k}',\sigma'} + \hat{c}_{L',\boldsymbol{k}',\sigma'} \hat{c}^{\dagger}_{L,\boldsymbol{k},\sigma} = \delta_{L,L'} \delta_{\boldsymbol{k}\boldsymbol{k}'} \delta_{\sigma,\sigma'} \tag{4.2a}$$

$$\left\{ \hat{c}_{L,\boldsymbol{k},\sigma}, \hat{c}_{L',\boldsymbol{k}',\sigma'} \right\} = \left\{ \hat{c}^{\dagger}_{L,\boldsymbol{k},\sigma}, \hat{c}^{\dagger}_{L',\boldsymbol{k}',\sigma'} \right\} = 0. \tag{4.2b}$$

We focus our study in the linear regime of graphene dispersion around the $\boldsymbol{K}_\xi$ valleys, where the Hamiltonian in Eq. (2.12) now takes the form

$$\hat{\mathcal{H}}_{\mathrm{L}} = \sum_{\xi} \sum_{\boldsymbol{p},\sigma} v(\xi p_x - i p_y) \hat{c}^{\boldsymbol{K}_\xi\,\dagger}_{A,\boldsymbol{p},\sigma} \hat{c}^{\boldsymbol{K}_\xi}_{B,\boldsymbol{p},\sigma} + h.c. + \mu \left(\hat{c}^{\boldsymbol{K}_\xi\,\dagger}_{A,\boldsymbol{p},\sigma} \hat{c}^{\boldsymbol{K}_\xi}_{A,\boldsymbol{p},\sigma} + \hat{c}^{\boldsymbol{K}_\xi\,\dagger}_{B,\boldsymbol{p},\sigma} \hat{c}^{\boldsymbol{K}_\xi}_{B,\boldsymbol{p},\sigma} \right), \tag{4.3}$$

and we can obtain expressions analogous to Eqs. (2.14) to write Hamiltonian above in terms of the eigenvectors of the graphene,

$$\hat{\mathcal{H}}_{\mathrm{L}} = \sum_{\xi} \sum_{\beta,\boldsymbol{p},\sigma} (\beta v p - \mu) \hat{c}^{\boldsymbol{K}_\xi\,\dagger}_{\beta,\boldsymbol{p},\sigma} \hat{c}^{\boldsymbol{K}_\xi}_{\beta,\boldsymbol{p},\sigma} \tag{4.4a}$$

$$\hat{c}^{\boldsymbol{K}_\xi}_{\beta,\boldsymbol{p},\sigma} = \frac{1}{2} \left(\hat{c}^{\boldsymbol{K}_\xi}_{A,\boldsymbol{p},\sigma} + \beta \xi e^{i\xi\theta} \hat{c}^{\boldsymbol{K}_\xi}_{B,\boldsymbol{p},\sigma} \right). \tag{4.4b}$$

This time, the operators $\hat{c}^{\boldsymbol{K}_\xi}_{\beta,\boldsymbol{p},\sigma}$ and $\hat{c}^{\boldsymbol{K}_\xi\,\dagger}_{\beta,\boldsymbol{p},\sigma}$ annihilate and create an electron with momentum $\boldsymbol{p}$ measured from the $\boldsymbol{K}_\xi$ in the valence ($\beta = -1$) or conduction ($\beta = +1$) with spin σ, respectively, and obey the anti-commutation rules in Eq. (4.2). One advantage of this notation is that it allows us to read clearly quantum states in our system. For example, at zero Kelvin, the ground state $|\mathrm{FS}\rangle$, defined as such many-body quantum state that minimises the total energy $\langle \mathrm{FS}| \hat{\mathcal{H}}_{\mathrm{L}} |\mathrm{FS}\rangle$, is a Fermi sea of electrons satisfying the condition $\beta v p - \mu < 0$,

$$|\mathrm{FS}\rangle = \prod_{\beta p < \frac{\mu}{v}} \hat{c}^{\boldsymbol{K}_\xi \dagger}_{\beta,\boldsymbol{p},\sigma} |\mathrm{vac}\rangle \,, \tag{4.5}$$

with $|\mathrm{vac}\rangle$ being the quantum state representing the vacuum of electrons.

In a typical type-I BCS superconductor, the Fermi surface consists of one electron or hole pocket, and the pairing interaction introduces the field

$$\hat{\mathcal{H}}_{\mathrm{SC}} = -g \sum_{\boldsymbol{k},\boldsymbol{k}'} \hat{\Phi}^\dagger_{\boldsymbol{k}} \hat{\Phi}_{\boldsymbol{k}'} \tag{4.6}$$

$$\hat{\Phi}_{\boldsymbol{k}} = \hat{c}_{\boldsymbol{k},\uparrow} \hat{c}_{-\boldsymbol{k},\downarrow},$$

which is manifestly a spin singlet: changing sign under inversion of all spins. How-

ever, trying to introduce this type of pairing order the Hamiltonian in Eq. (4.4) is not as simple, as the Fermi surface in graphene consists of two disconnected electron ($\mu > 0$) or hole ($\mu < 0$) circular pockets around the two inequivalent $\boldsymbol{K}_\xi$ points. This extra degree of freedom makes room for two types of pairing fields when we map the electronic wave-number $\boldsymbol{k}$ in Eq. (4.6), measured from the Γ-point, on a state in the valley $\boldsymbol{K}_\xi$ with momentum $\boldsymbol{p}$,

$$\hat{\Phi}_{A_1,\boldsymbol{p}} = \hat{c}^{\boldsymbol{K}_+}_{\beta,-\boldsymbol{p},\downarrow}\hat{c}^{\boldsymbol{K}_-}_{\beta,+\boldsymbol{p},\uparrow} + \hat{c}^{\boldsymbol{K}_-}_{\beta,-\boldsymbol{p},\downarrow}\hat{c}^{\boldsymbol{K}_+}_{\beta,+\boldsymbol{p},\uparrow}, \tag{4.7a}$$

$$\hat{\Phi}_{B_1,\boldsymbol{p}} = \hat{c}^{\boldsymbol{K}_+}_{\beta,-\boldsymbol{p},\downarrow}\hat{c}^{\boldsymbol{K}_-}_{\beta,+\boldsymbol{p},\uparrow} - \hat{c}^{\boldsymbol{K}_-}_{\beta,-\boldsymbol{p},\downarrow}\hat{c}^{\boldsymbol{K}_+}_{\beta,+\boldsymbol{p},\uparrow}. \tag{4.7b}$$

The subscripts in each wave function label irreducible representation of the group C''_{6v} (point group of graphene crystal C_{6v} plus primitive translations), to which they belong [71]. The first type of pairing is spin singlet and valley triplet, as it changes sign under the inversion of spins while being invariant under inversion of valley index. Conversely, the second type pairing is spin triplet and valley singlet, featuring opposite sign changes under inversion of spins or valley index, respectively. Each pairing defines an order parameter $\Delta_{\Lambda,\boldsymbol{p}} = g\,\langle \mathrm{GS}|\,\hat{\Phi}_{\Lambda,\boldsymbol{p}}\,|\mathrm{GS}\rangle$ ($\Lambda = A_1, B_1$), where $|\mathrm{GS}\rangle$ represents the to-be-determined ground state, and its dependence on $\boldsymbol{p}$ characterises the superconducting state. For example, type-I superconductors have an s-wave pairing order, as Δ is constant and positive across the Fermi surface. Conversely, in unconventional superconductors, the order parameter can change sign at different points (nodes) in the Fermi surface. The number of nodes often defines the superconducting state: two nodes corresponds to a p-wave superconductivity, four nodes to a d-wave superconductivity... Some studies suggest that graphene can host these types of unconventional superconductivity, [108, 110, 111], but the pairing orders we proposed in Eq. (4.6) do not contain nodes around $\boldsymbol{K}_\xi$ and they are constant across the Fermi surface, $\Delta_{\Lambda,\boldsymbol{p}} = \Delta_\Lambda$. In particular, the superconducting order Δ_{A_1} is positive in both Fermi pockets around $\boldsymbol{K}_\pm$, and it is the so-called extended s-wave (Fig. 4.1.1a). The order parameter Δ_{B_1} does not contain nodes within each Fermi pocket, yet it is still considered an f-wave superconductor, as it changes sign six times across the boundaries of the first Brillouin zone

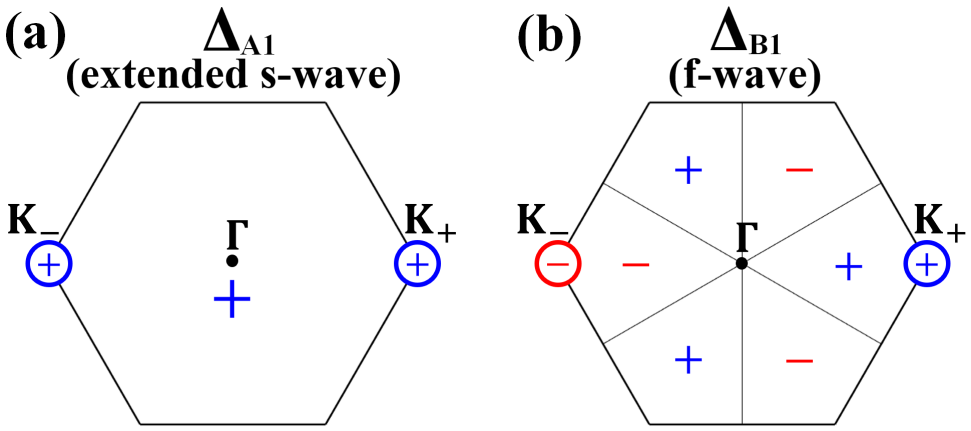

Figure 4.1.1: Pictorial representation of the sign of the two pairing orders Δ_{A_1} and Δ_{B_1}. (a) The extended s-wave is positive and isotropic across the Fermi surface, whereas (b) the f-wave changes sign along the lines that connects opposite M points.

(Fig. 4.1.1b).

The total Hamiltonian, $\hat{\mathcal{H}} = \hat{\mathcal{H}}_L + \hat{\mathcal{H}}_{SC}$, cannot be diagonalised, as it contains products of four electron operators. To circumvent this problem, we perform a mean-field approximation [112] and to illustrate this explicitly we rewrite the pairing perturbation as

$$\begin{aligned}\hat{\mathcal{H}}_{SC} &= -g\left[\left(\hat{\Phi}^{\dagger}_{\Lambda} - \Delta^{*}_{\Lambda}/g\right) + \Delta^{*}_{\Lambda}/g\right]\left[\left(\hat{\Phi}_{\Lambda} - \Delta_{\Lambda}/g\right) + \Delta_{\Lambda}/g\right] = \\ &= -\Delta_{\Lambda}\hat{\Phi}^{\dagger}_{\Lambda} - \Delta^{*}_{\Lambda}\hat{\Phi}_{\Lambda} + \frac{|\Delta_{\Lambda}|^{2}}{g} - g\left(\hat{\Phi}^{\dagger}_{\Lambda} - \Delta^{*}_{\Lambda}/g\right)\left(\hat{\Phi}_{\Lambda} - \Delta_{\Lambda}/g\right).\end{aligned} \tag{4.8}$$

In the expression above, the round brackets $(\hat{\Phi}_{\Lambda} - \Delta_{\Lambda}/g)$ represents the quantum fluctuations of the two-electrons wave function around its mean value. The mean-field approach relies on the assumption that these fluctuations are small, and neglects the fourth term in the second line of Eq. (4.8), which is quadratic in fluc-

tuations. In doing so, our Hamiltonian takes the form

$$\hat{\mathcal{H}} = \sum_{\beta,\boldsymbol{p}} \left[\sum_{\xi,\sigma} \varepsilon_{\boldsymbol{p},\beta} \hat{c}^{\boldsymbol{K}_\xi\,\dagger}_{\beta,\boldsymbol{p},\sigma} \hat{c}^{\boldsymbol{K}_\xi}_{\beta,\boldsymbol{p},\sigma} - \Delta_\Lambda \left(\hat{c}^{\boldsymbol{K}_+\,\dagger}_{\beta,-\boldsymbol{p},\downarrow} \hat{c}^{\boldsymbol{K}_-\,\dagger}_{\beta,\boldsymbol{p},\uparrow} + \lambda \hat{c}^{\boldsymbol{K}_-\,\dagger}_{\beta,-\boldsymbol{p},\downarrow} \hat{c}^{\boldsymbol{K}_+\,\dagger}_{\beta,\boldsymbol{p},\uparrow} \right) + h.c. \right], \tag{4.9}$$

where we introduce $\varepsilon^{\boldsymbol{K}_\xi}_{\boldsymbol{p},\beta} = \beta v p - \mu$, and $\lambda = +1$ ($\lambda = -1$) generates the pairing with A1 (B1) symmetry. To diagonalise the resulting Hamiltonian, we need a basis that accounts for terms with two creation or two annihilation operators. Such basis, often called the Nambu representation [113], contains both electron annihilation and creation operators as follows

$$\hat{A}_{\beta,\boldsymbol{p}} = \begin{pmatrix} \hat{c}^{\boldsymbol{K}_+}_{\beta,\mathbf{p},\uparrow} \\ \hat{c}^{\boldsymbol{K}_-\,\dagger}_{\beta,-\mathbf{p},\downarrow} \\ \hat{c}^{\boldsymbol{K}_-}_{\beta,\mathbf{p},\uparrow} \\ \hat{c}^{\boldsymbol{K}_+\,\dagger}_{\beta,-\mathbf{p},\downarrow} \end{pmatrix}, \tag{4.10}$$

which re-expresses the Hamiltonian as

$$\hat{\mathcal{H}} = \sum_{\beta,\mathbf{p}} \hat{A}^\dagger_{\beta,\mathbf{p}} \mathcal{M} \hat{A}_{\beta,\mathbf{p}}, \tag{4.11}$$

$$\mathcal{M} = \begin{pmatrix} \varepsilon^{\boldsymbol{K}_+}_{\boldsymbol{p},\beta} & -\Delta_\Lambda & 0 & 0 \\ -\Delta^*_\Lambda & -\varepsilon^{\boldsymbol{K}_-}_{-\boldsymbol{p},\beta} & 0 & 0 \\ 0 & 0 & \varepsilon^{\boldsymbol{K}_-}_{\boldsymbol{p},\beta} & -\lambda\Delta_\Lambda \\ 0 & 0 & -\lambda\Delta^*_\Lambda & -\varepsilon^{\boldsymbol{K}_+}_{\boldsymbol{p},\beta} \end{pmatrix}.$$

Notice that, in the Hamiltonian above, the first and third diagonal terms generate the electron number operator $\hat{c}^{\boldsymbol{K}_\xi\,\dagger}_{\beta,\boldsymbol{p},\uparrow} \hat{c}^{\boldsymbol{K}_\xi}_{\beta,\boldsymbol{p},\uparrow}$, which counts the number of occupied states, while the second and fourth diagonal terms generate these the hole number operator $\hat{c}^{\boldsymbol{K}_\xi}_{\beta,-\boldsymbol{p},\downarrow} \hat{c}^{\boldsymbol{K}_\xi\,\dagger}_{\beta,-\boldsymbol{p},\downarrow}$, which counts the number of holes, and introduces a minus sign in the second and fourth diagonal terms of Eq. (4.11).

The eigenvalues of the Hamiltonian in Eq. (4.11) are the quasiparticle the four-fold degenerate dispersion

$$E_{\beta,\boldsymbol{p}} = \sqrt{\varepsilon^2_{\beta,\boldsymbol{p}} + \Delta^2_\lambda}. \tag{4.12}$$

On the other hand, the matrix $\mathcal{M}$ is Hermitian and therefore it can be diagonalised by a unitary transformation $\mathcal{U}^\dagger_{\beta,\boldsymbol{p}}\mathcal{M}\mathcal{U}_{\beta,\boldsymbol{p}}$, often referred to as Bogoliubov transformation [114],

$$\mathcal{U}^s_{\mathbf{p}} = \begin{pmatrix} u_{\beta,\mathbf{p}} & v_{\beta,\mathbf{p}} & 0 & 0 \\ -v_{\beta,\mathbf{p}} & u_{\beta,\mathbf{p}} & 0 & 0 \\ 0 & 0 & u_{\beta,\mathbf{p}} & \lambda v_{\beta,\mathbf{p}} \\ 0 & 0 & -\lambda v_{\beta,\mathbf{p}} & u_{\beta,\mathbf{p}} \end{pmatrix}, \tag{4.13}$$

expressed in terms of the Bogoliubov coefficients

$$u_{\beta,\boldsymbol{p}} = \frac{1}{\sqrt{2}}\sqrt{1 + \frac{\varepsilon_{\beta,\boldsymbol{p}}}{E_{\beta,\boldsymbol{p}}}}, \tag{4.14a}$$

$$v_{\beta,\boldsymbol{p}} = \frac{1}{\sqrt{2}}\sqrt{1 - \frac{\varepsilon_{\beta,\boldsymbol{p}}}{E_{\beta,\boldsymbol{p}}}}. \tag{4.14b}$$

This transformation allows us to define the Bogoliubov quasiparticles

$$\begin{pmatrix} \hat{\gamma}^{1\,\dagger}_{\beta,\boldsymbol{p}} \\ \hat{\gamma}^{2}_{\beta,\boldsymbol{p}} \\ \hat{\gamma}^{3\,\dagger}_{\beta,\boldsymbol{p}} \\ \hat{\gamma}^{4}_{\beta,\boldsymbol{p}} \end{pmatrix} = \begin{pmatrix} u_{\beta,\boldsymbol{p}} c^{K_+\,\dagger}_{\beta,\boldsymbol{p},\uparrow} + v_{\beta,\boldsymbol{p}} c^{K_-}_{\beta,-\boldsymbol{p},\downarrow} \\ u_{\beta,\boldsymbol{p}} c^{K_-}_{\beta,-\boldsymbol{p},\downarrow} - v_{\beta,\boldsymbol{p}} c^{K_+\,\dagger}_{\beta,\boldsymbol{p},\uparrow} \\ u_{\beta,\mathbf{p}} c^{K_-\,\dagger}_{\beta,\boldsymbol{p},\uparrow} + \lambda v_{\beta,\boldsymbol{p}} c^{K_+}_{\beta,-\boldsymbol{p},\downarrow} \\ u_{\beta,\mathbf{p}} c^{K_+}_{\beta,-\boldsymbol{p},\downarrow} - \lambda v_{\beta,\boldsymbol{p}} c^{K_-\,\dagger}_{\beta,\boldsymbol{p},\uparrow} \end{pmatrix}. \tag{4.15}$$

These quasiparticles are admixtures of electrons and holes, with equal weights around the Fermi surface ($u_{\beta,\boldsymbol{p}} = v_{\beta,\boldsymbol{p}} = 1/\sqrt{2}$) and with a strong hole-like ($u_{\beta,\boldsymbol{p}} = 0$) or electron-like ($v_{\beta,\boldsymbol{p}} = 0$) character well below or above the Fermi level, respectively.

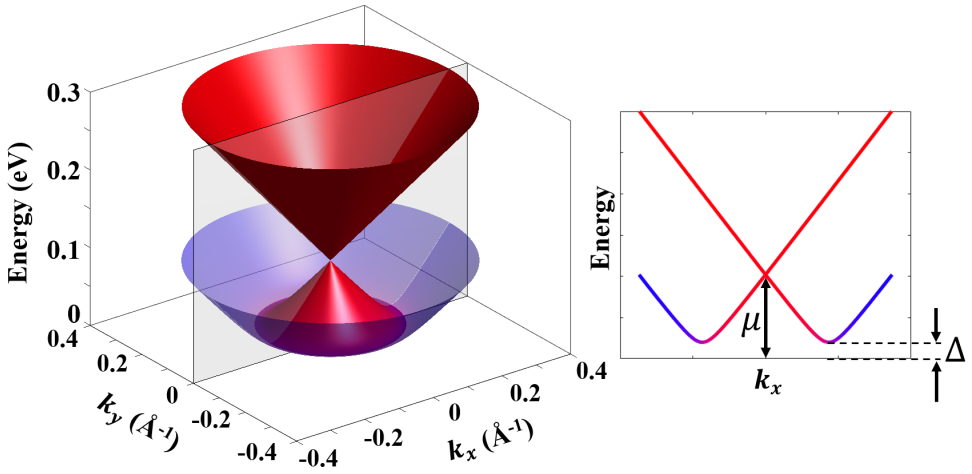

Figure 4.1.2: Quasiparticle spectrum around the $\boldsymbol{K}_+$ point. For illustration purposes, we chose a superconducting gap of $\Delta = 20$ meV, in graphene with $\mu = 100$ meV. We plot in blue (red) quasiparticle states with electron (hole) character, for which $v_{\beta,\boldsymbol{p}} \approx 0$ and $u_{\beta,\boldsymbol{p}} \approx 1$ ($v_{\beta,\boldsymbol{p}} \approx 1$ and $u_{\beta,\boldsymbol{p}} \approx 0$). States at the bottom of the dispersion, shown in violet, have values for the Bogoliubov coefficients $v_{\beta,\boldsymbol{p}} \approx u_{\beta,\boldsymbol{p}} \approx 1/\sqrt{2}$.

Finally, we study the ground state of this superconducting system $|\mathrm{GS}\rangle$ in terms of electronic operators. We notice that, after the transformation in Eq. (4.15), the Hamiltonian reads

$$\hat{\mathcal{H}} = \sum_{\beta,\mathbf{p}} \sum_{j=1}^{4} E_{\beta,\mathbf{p}} \hat{\gamma}^{j\,\dagger}_{\beta,\mathbf{p}} \hat{\gamma}^{j}_{\beta,\mathbf{p}}. \tag{4.16}$$

Now we can read again the ground state of the system as such state that minimises the energy. This time, because $E_{\beta,\boldsymbol{p}} > 0$, such state is defined as a quasiparticle vacuum. We can construct it in terms of electronic states assuming that it vanishes under the application of a quasiparticle annihilation operator,

$$\hat{\gamma}^{j}_{\beta,\mathbf{p}} |\mathrm{GS}\rangle = 0, \qquad j = 1, 2, 3, 4. \tag{4.17}$$

We can construct an ansatz for the ground state as consisting of a linear combination of no electrons and two paired of electronic operators, which converts the

condition above in a set of four equations. The resulting ground state is

$$|\mathrm{GS}\rangle = \prod_{\mathbf{p}} \left(u_{\beta,\mathbf{p}} + v_{\beta,\mathbf{p}} \hat{c}^{K+\dagger}_{\mathbf{p},\uparrow} \hat{c}^{K-\dagger}_{-\mathbf{p},\downarrow}\right) \left(u_{\beta,\mathbf{p}} + \lambda v_{\beta,\mathbf{p}} \hat{c}^{K-\dagger}_{\mathbf{p},\uparrow} \hat{c}^{K+\dagger}_{-\mathbf{p},\downarrow}\right) |\mathrm{vac}\rangle \,. \tag{4.18}$$

As expected, the ground state for the extended s-wave ($\lambda = +1$) is identical to that of a type-I superconductor in the framework of the BCS theory [92].

4.2 Theoretical description of ERS in superconducting graphene

In this section we study the ERS features in doped graphene ($\mu \sim 100$ meV) affected by the superconducting order described in the previous section. Because such orders typically induce gaps in the dispersion of ~ 1 meV [98], inter-band features are expected to be similar to those described in the previous chapter, while intra-band contributions potentially represent a truly new change in the electronic Raman spectrum. The total Hamiltonian is

$$\hat{\mathcal{H}} = \hat{\mathcal{H}}_{\mathrm{L}} + \hat{\mathcal{H}}_{\mathrm{SC}} + \hat{\mathcal{V}}(\boldsymbol{r}, t), \tag{4.19}$$

where the third term in the equation above is the second-quantised form of the light-matter interaction term, which, as in the previous chapter, is obtained by replacing $\boldsymbol{P} \to \boldsymbol{p} - e\boldsymbol{A}$ in Eq. (4.1). In the previous chapter, the electronic part of final quantum state $\langle s_{\mathrm{f}}|$ contained one electron-hole pair on a Fermi sea of electrons, while in this chapter, such electron-hole pair is created on the ground state of the superconducting system, a quasiparticle vacuum. The interband and intra band transitions, are now given by

$$|s_{\mathrm{f}}\rangle^{\mathrm{inter}} = \hat{c}^{\boldsymbol{K}_\xi\,\dagger}_{+1,\boldsymbol{p}_{\mathrm{e}},\sigma} \hat{c}^{\boldsymbol{K}_\xi}_{-1,\boldsymbol{p}_{\mathrm{h}},\sigma} |\mathrm{GS}\rangle \,, \tag{4.20a}$$

$$|s_{\mathrm{f}}\rangle^{\mathrm{intra}} = \hat{c}^{\boldsymbol{K}_\xi\,\dagger}_{+1,\boldsymbol{p}_{\mathrm{e}},\sigma} \hat{c}^{\boldsymbol{K}_\xi}_{+1,\boldsymbol{p}_{\mathrm{h}},\sigma} |\mathrm{GS}\rangle \,. \tag{4.20b}$$

We need to express the electronic operators in the equation above in terms of quasiparticle operators, inverting the relation in Eq. (4.15),

$$\begin{pmatrix} \hat{c}^{K_+}_{\beta,\boldsymbol{p}\uparrow} \\ \hat{c}^{K_-\dagger}_{\beta,-\boldsymbol{p}\downarrow} \\ \hat{c}^{K_-}_{\beta,\uparrow} \\ \hat{c}^{K_+\dagger}_{\beta,-\downarrow} \end{pmatrix} = \begin{pmatrix} u_{\beta,\boldsymbol{p}}\hat{\gamma}^{1}_{\beta,\boldsymbol{p}} - v_{\beta,\boldsymbol{p}}\hat{\gamma}^{2\,\dagger}_{\beta,\boldsymbol{p}} \\ u_{\beta,\boldsymbol{p}}\hat{\gamma}^{2\,\dagger}_{\beta,\boldsymbol{p}} + v_{\beta,\boldsymbol{p}}\hat{\gamma}^{1}_{\beta,\boldsymbol{p}} \\ u_{\beta,\boldsymbol{p}}\hat{\gamma}^{3}_{\beta,\boldsymbol{p}} - \lambda v_{\beta,\boldsymbol{p}}\hat{\gamma}^{4\,\dagger}_{\beta,\boldsymbol{p}} \\ u_{\beta,\boldsymbol{p}}\hat{\gamma}^{4\dagger}_{\beta,\boldsymbol{p}} + \lambda v_{\beta,\boldsymbol{p}}\hat{\gamma}^{3}_{\beta,\boldsymbol{p}} \end{pmatrix}. \tag{4.21}$$

The two terms in Eq. (4.20) lead to different spectroscopic changes in the Raman spectrum and, as in the previous chapter, they will be studied separately in the following two sections.

4.2.1 Inter-band transitions

In inter-band transitions, the band indices take the values $\beta_i = -1$ and $\beta_f = +1$. Therefore we re-express (4.20a) in terms of quasiparticle operators using the relations in Eq. (4.21)

$$|s_f\rangle^{\text{inter}}_1 = +u_{+,\boldsymbol{p}}\hat{\gamma}^{1\,\dagger}_{+,\boldsymbol{p}}\hat{\gamma}^{2\,\dagger}_{-,-\boldsymbol{p}}\,|\text{GS}\rangle\,, \tag{4.22a}$$

$$|s_f\rangle^{\text{inter}}_2 = -u_{+,\boldsymbol{p}}\hat{\gamma}^{2\dagger}_{+,-\boldsymbol{p}}\hat{\gamma}^{1\dagger}_{-,\boldsymbol{p}}\,|\text{GS}\rangle\,, \tag{4.22b}$$

$$|s_f\rangle^{\text{inter}}_3 = +\lambda u_{+,\boldsymbol{p}}\hat{\gamma}^{3\dagger}_{+,\boldsymbol{p}}\hat{\gamma}^{4\dagger}_{-,-\boldsymbol{p}}\,|\text{GS}\rangle\,, \tag{4.22c}$$

$$|s_f\rangle^{\text{inter}}_4 = -\lambda u_{+,\boldsymbol{p}}\hat{\gamma}^{4\dagger}_{+,-\boldsymbol{p}}\hat{\gamma}^{3\dagger}_{-,\boldsymbol{p}}\,|\text{GS}\rangle\,, \tag{4.22d}$$

where we take the factor $v_{-,\boldsymbol{p}} \approx 1$. The excited states consist of the creation of two quasiparticles, and have energy

$$\omega = \sqrt{\varepsilon^2_{+,\boldsymbol{p}} + \Delta^2_\Lambda} + \sqrt{\varepsilon^2_{-,\boldsymbol{p}} + \Delta^2_\Lambda} \approx |\Delta_\Lambda| + \sqrt{v^2p^2 + \Delta^2_\Lambda}. \tag{4.23}$$

We compute the matrix elements ${}^{\text{inter}}_{j}\langle s_f|\mathcal{R}^c_{em} + \mathcal{R}^L_{em}\,|\text{GS}\rangle$ as before, and calculate their amplitude squared to calculate the Raman probability. Integrating over all

points in reciprocal space we get

$$
\begin{aligned}
w(\omega) =& \sum_{j} \lim_{T\to\infty} \frac{1}{T} \int \frac{d\boldsymbol{p}}{(2\pi\hbar)^2} \left| {}^{\text{inter}}_{j}\langle s_f | \mathcal{R}^{c}_{em} + \mathcal{R}^{L}_{em} | GS\rangle \right|^2 = \qquad (4.24)\\
=& 4\frac{\hbar e^4 v^4}{\varepsilon_o^2 \Omega^2} \left(\frac{1}{\Omega^2}\Xi_s + \frac{1}{2(6\gamma_o)^2}\Xi_o \right) \int p\, dp\, u^2_{+,\boldsymbol{p}} \delta(E_{+,\boldsymbol{p}} + E_{-,\boldsymbol{p}} - \omega) =\\
=& \frac{\hbar e^4 v^2}{\varepsilon_o^2 \Omega^2} \left(\frac{1}{\Omega^2}\Xi_s + \frac{1}{2(6\gamma_o)^2}\Xi_o \right) \left(\omega + \frac{\Delta^2}{2\mu - \omega} \right) \Theta\left(\omega - 2\mu - |\Delta|\right),
\end{aligned}
$$

and integrating over all possible scattered angles, we find the spectral density,

$$
\begin{aligned}
g(\omega) =& \frac{1}{c} \int \frac{d\tilde{\boldsymbol{q}} d\tilde{q}_z}{(2\pi\hbar)^3} w(\omega) \delta\left(\tilde{\Omega} - c\sqrt{\tilde{q}^2 + \tilde{q}_z} \right) = \qquad (4.25)\\
=& \left(\frac{e^2}{2\pi\hbar c} \frac{v}{c} \right)^2 \left(\frac{1}{\Omega^2}\Xi_s + \frac{1}{2(6\gamma_o)^2}\Xi_o \right) \left(\omega + \frac{\Delta^2}{2\mu - \omega} \right) \Theta\left(\omega - 2\mu - |\Delta|\right).
\end{aligned}
$$

Comparing the equation above with Eq. (3.14), we find that superconductivity does not introduce significant changes to interband contributions. We make that apparent in Fig. 4.2.1, where we show the contribution to the ERS spectrum of graphene (black dashed line) and superconducting graphene (solid line).

4.2.2 Intra-band transitions

Intraband excitations lead to final states in Eq. (4.20b), which in terms of Bogoliubov quasiparticles take the form

$$
\begin{aligned}
|s_f\rangle^{\text{intra}}_1 &= \left(+u_{+,\boldsymbol{p}} v_{+,\boldsymbol{p}} \hat{\gamma}^{1\,\dagger}_{+,\boldsymbol{p}} \hat{\gamma}^{2\,\dagger}_{+,-\boldsymbol{p}} + v^2_{+,\boldsymbol{p}} \right) |GS\rangle \qquad (4.26a)\\
|s_f\rangle^{\text{intra}}_2 &= \left(-u_{+,\boldsymbol{p}} v_{+,\boldsymbol{p}} \hat{\gamma}^{2\dagger}_{+,-\boldsymbol{p}} \hat{\gamma}^{1\dagger}_{+,\boldsymbol{p}} + v^2_{+,\boldsymbol{p}} \right) |GS\rangle \qquad (4.26b)\\
|s_f\rangle^{\text{intra}}_3 &= \left(+\lambda u_{+,\boldsymbol{p}} v_{+,\boldsymbol{p}} \hat{\gamma}^{3\dagger}_{+,\boldsymbol{p}} \hat{\gamma}^{4\dagger}_{+,-\boldsymbol{p}} + v^2_{+,\boldsymbol{p}} \right) |GS\rangle \qquad (4.26c)\\
|s_f\rangle^{\text{intra}}_4 &= \left(-\lambda u_{+,\boldsymbol{p}} v_{+,\boldsymbol{p}} \hat{\gamma}^{4\dagger}_{+,-\boldsymbol{p}} \hat{\gamma}^{3\dagger}_{+,\boldsymbol{p}} + v^2_{+,\boldsymbol{p}} \right) |GS\rangle . \qquad (4.26d)
\end{aligned}
$$

The first term in these states generates an excited state, consisting of the creation of two quasiparticles, and has energy

$$\omega = 2E_{+,\boldsymbol{p}} = 2\sqrt{(v p - \mu)^2 + \Delta^2}, \tag{4.27}$$

while second term does not affect the quasiparticle vacuum. The Raman probability and the spectral density are

$$\begin{aligned} w(\omega) = &\sum_{j} \lim_{T\to\infty} \frac{1}{T} \int \frac{\mathrm{d}\boldsymbol{p}}{(2\pi\hbar)^2} \left| {}^{\text{intra}}_{j}\langle \text{exc}|\mathcal{R}^{c}_{em} + \mathcal{R}^{L}_{em}|\text{GS}\rangle \right|^2 = \\ =&\frac{4\hbar e^4 v^4}{\varepsilon_o^2 \Omega^2} \int p\, \mathrm{d}p\, u^2_{+,\boldsymbol{p}}\, v^2_{+,\boldsymbol{p}} \delta(2E_{+,\boldsymbol{p}} - \omega) \\ &\times \left\{ \left[\left(\frac{4\mu}{\Omega^2}\right)^2 + \left(\frac{\gamma_n}{\gamma_o^2}\right)^2 \right] \Xi'_s + \left[\frac{1}{2}\left(\frac{4\mu}{\Omega^2}\right)^2 + \frac{1}{2}\left(\frac{1}{6\gamma_o}\right)^2 \right] \Xi_o \right\} = \\ =&\frac{4\hbar e^4 v^2}{\varepsilon_o^2 \Omega^2} \frac{\mu\Delta^2}{\omega\sqrt{\omega^2 - 4\Delta^2}} \left\{ \left[\left(\frac{4\mu}{\Omega^2}\right)^2 + \left(\frac{\gamma_n}{\gamma_o^2}\right)^2 \right] \Xi'_s + \right. \\ &\left. + \left[\frac{1}{2}\left(\frac{4\mu}{\Omega^2}\right)^2 + \frac{1}{2}\left(\frac{1}{6\gamma_o}\right)^2 \right] \Xi_o \right\}, \end{aligned} \tag{4.28}$$

$$\begin{aligned} g(\omega) = \left(\frac{e^2 v}{\varepsilon_o \pi \hbar c^2}\right)^2 &\frac{\mu\Delta^2}{\omega\sqrt{\omega^2 - 4\Delta^2}} \left\{ \left[\left(\frac{4\mu}{\Omega^2}\right)^2 + \left(\frac{\gamma_n}{\gamma_o^2}\right)^2 \right] \Xi_o + \right. \\ &\left. + \left[\frac{1}{2}\left(\frac{4\mu}{\Omega^2}\right)^2 + \frac{1}{2}\left(\frac{1}{6\gamma_o}\right)^2 \right] \Xi_s \right\}. \end{aligned} \tag{4.29}$$

In Figs. 4.2.1, 4.2.2 and 4.2.3, we present our findings. This type of contribution generates a new feature in the Raman spectrum, an asymmetric peak at $2\Delta_\Lambda$, which is approximately insensitive to the polarisation of incindent/detected light and increases with the third power of the Fermi level. Interestingly, the height of the peak is proportional to $\sqrt{\Delta}$, which can be explained by evaluating explicitly the functional dependence of the spectral density at $2\Delta + \delta^+$ [85].

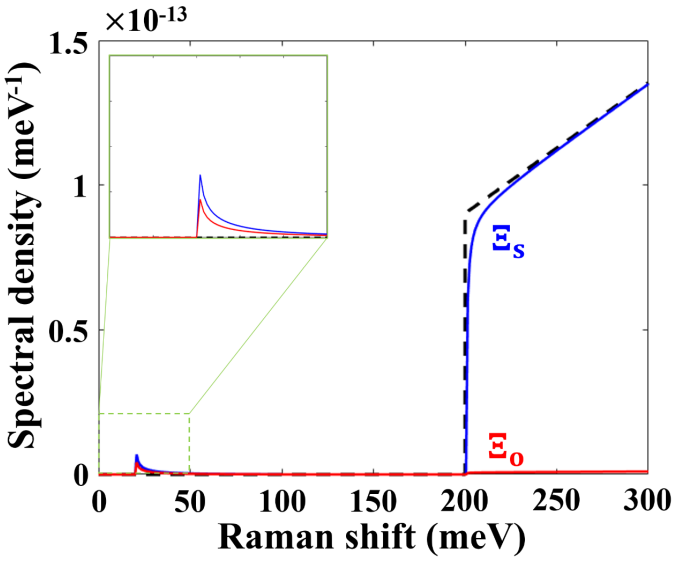

Figure 4.2.1: Spectral densty of superconducting graphene for cross-linear (blue) and parallel-linear (red) polarisation, with $\mu = 100$ meV, and $\Delta = 10$ meV.

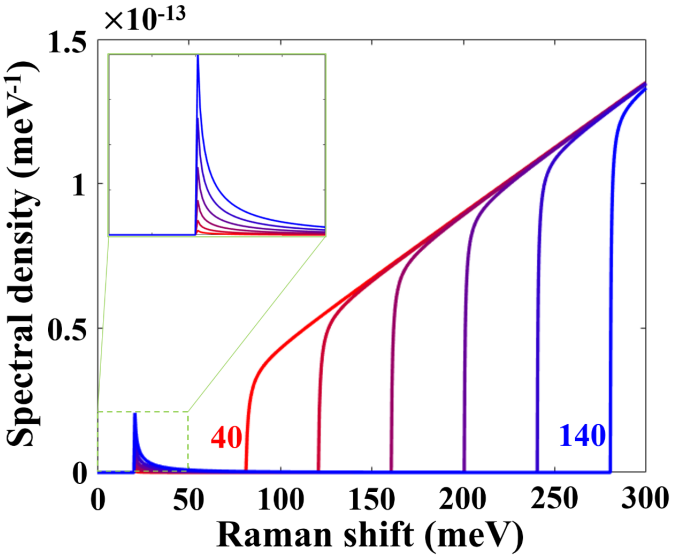

Figure 4.2.2: Spectral densty of superconducting graphene in cross-linear polarisation, with $\Delta = 10$ meV and μ ranging from 40 meV to 100 meV.

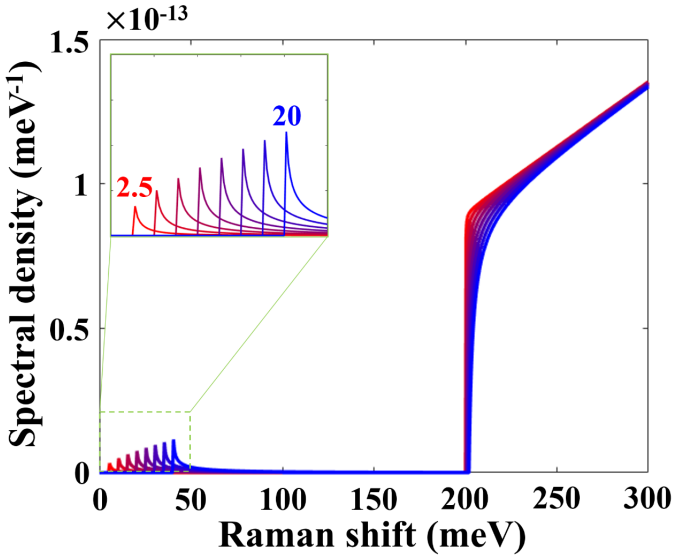

Figure 4.2.3: Spectral densty of superconducting graphene in cross-linear polarisation, with $\mu = 100$ meV and Δ ranging from 2.5 meV to 20 meV.

4.3 Experimental evidence for ERS in superconducting graphene

Hitherto, there has been no experimental evidence of signatures of superconductivity in the Raman spectrum of graphene, nor the induced features presented in this chapter. Therefore, it is worth discussing here the feasibility of detecting Raman spectral changes induced by the presence of a superconducting order in graphene. Electronic inter-band transitions in superconducting graphene leave step-like signatures, barely different from their non-superconducting counterpart. One could attempt to study their differences by subtracting the spectra corresponding to the superconducting and normal state. However, switching on and off a superconducting state at the same temperature could not be as simple as changing a gate voltage, and other phonon-mediated features may also emerge in the Raman spectrum at energy scales $\sim$ 0.1 meV. Our hopes for detecting superconductivity actually rely on electronic intra-band transitions. They give rise to a new peak in the Raman spectrum. Its position is near the origin, which prevents any competition

with stronger Raman signals. Furthermore, its shape is strongly connected with the quasiparticle dispersion, which would pave a non-invasive way to observe and study superconductive orders in graphene. However, there are several challenges that experimentalist would face. Firstly, this Raman signal is weak. We estimate its quantum efficiency for typical values $\Omega \sim 2$ eV, $\mu \sim 100$ meV and $\Delta \sim 10$ meV, as

$$I = \int_{2\Delta}^{\infty} \mathrm{d}\omega g(\omega) = \left(\frac{e^2 v^2}{\varepsilon_0 \pi \hbar c^2}\right)^2 \frac{\mu\Delta}{2} \left(\frac{4\mu}{\Omega^2}\right)^2 \arctan\left(\sqrt{x^2-1}\right)\Big|_1^{\infty} \approx 6 \cdot 10^{-14}, \tag{4.30}$$

which is about three orders of magnitude weaker than the intensity of the G-peak. Secondly, several studies point out that laser-induced heating can raise the temperature in the sample by tens of degrees, which could potentially destroy any superconducting order [115].

Regardless of its experimental observation, the value we obtained for the quantum efficiency is one order of magnitude higher than intra-band transitions in normal graphene [80]. This is due to the emergence of new saddle points in the dispersion, as shown in Fig. 4.1.2, which tend to concentrate electrons at certain energies, yielding sharp peaks in the density of states. However, these saddle points, which originate from the electronic coupling, are not exclusive to superconducting graphene. In fact, as we shall see, the dispersion of rhombohedral graphite is rather similar to the quasiparticle spectrum here. This idea inspired the next chapter, devoted to study of ERS features on graphite.

Persistence is to the character of man as carbon is to steel.

Napoleon Hill

5

Electronic Raman scattering in graphite

Before the advent of graphene, the scientific community had already made significant efforts to understand the physical properties of its bulk counterpart, graphite, for more than seven decades. This material is comprised of vertically stacked layers of graphene, bound together by the van der Waals interactions. They originate from the vertical hybridization of p_z orbitals, which couples adjacent layers with a strength about one order of magnitude weaker than the coupling produced by their in-plane hybridisation, yet it introduces important changes in the Dirac Hamiltonian of graphene at energy scales $\sim$ 0.1 eV. Furthermore, such vertical staking is not unique. Owing to its layered structure, the stacking order stands as an additional degree of freedom in multi-layer graphene. For two layers (bilayer graphene), the most energetically favourable arrangement is such that half of the atoms in each layer lie directly opposite to a carbon atom in the other layer while the other half find themselves in the centre of the hexagonal rings (Fig. 5.0.1).

The two possible arrangements, namely AB or BA stacking, are equivalent to each other, as they are related by symmetry operations. However, trying to stack a third layer in the same way leads to two different stacking orders, depending on the position of the new layer with respect the first one. The stacking in which the atoms in the third layer are directly above those in the first one is referred to as Bernal, or ABA (Fig. 5.0.2a). In contrast, the configuration where the unpaired half of the atoms of the second layer lie directly below half of the third layer is known as rhombohedral, or ABC stacking (Fig. 5.0.2b). Notice that rhombohedral trilayer graphite, unlike its Bernal counterpart, is not mirror symmetric with respect to the plane of the second graphene layer, but it is symmetric under inversion with respect to the centre of the hexagons of the second layer [116].

While this difference may look subtle, it leads to profound discrepancies in their stability. As a matter of fact, Bernal graphite is thermally more stable, accounting for more than the 90 % of the naturally occurring graphite, whereas rhombohedral graphite is commonly found as a stacking fault in Bernal-stacked films [117]. Arguably, the most striking differences become apparent in the low-energy electronic dispersion of N-layers Bernal and rhombohedral graphite. The former consists of $2N$ parabolic bands arising from the $\boldsymbol{K}_{\pm}$ points (two of them are linear for odd number of layers), half of them split from the origin of energies. The latter, in contrasts, features $2(N-1)$ gapped bulk bands hosting saddle points in a trigonally warped circle around the $\boldsymbol{K}_{\pm}$ points and two nearly flat bands at the neutrality point, the extension of which increases with the number of layers. Moreover, their topological nature confines these flat bands to the outermost layers, which has fuelled hopes of finding strongly correlated phenomena in graphite, including magnetism [118, 119], charge density waves [120, 121], or superconductivity [122, 123].

On the experimental side, we have witnessed important advances towards controlling the stacking order of graphitic films over the last decade [124]. In this context, relying on non-invasive spectroscopic techniques that provide information about the number of layers and characterise the stacking is of paramount importance. Optical absorption is a well studied method in graphite [125] that allows

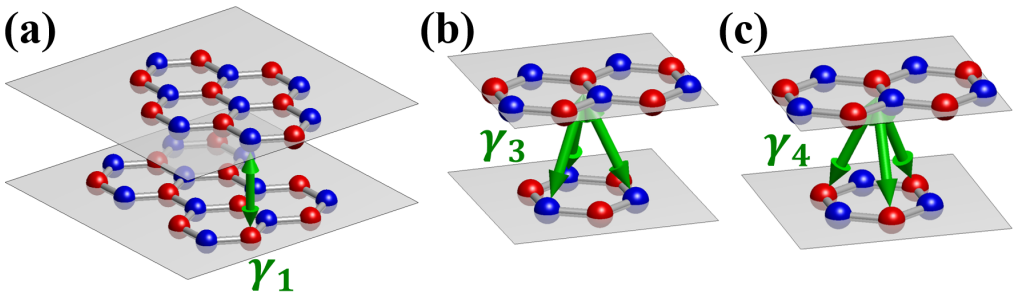

Figure 5.0.1: (a) Pictorial representation of the atomic structure of bilayer graphene, highliting the dimer sites, coupled by γ_1. The blue (red) balls represent the positions of the A (B) sub-lattice sites. In (b) and (c), the green arrows connect the sites coupled by γ_3 and γ_4, respectively.

us to count the number of layers, each of them absorbing about $\sim$ 2.3% of the incoming light [25]. However, this method is less reliable for graphitic films with more than $\sim$10 layers, and the energy resolution at energy scales $\sim$ 0.1 eV is still not good enough to discern stacking differences [67]. Experimentalists have also used Raman spectra to distinguish these two configurations, relying on the different type of phonon excitations that lead to changes in the shape of the 2D band [117, 126]. Nonetheless, these differences are subtle, which makes difficult the interpretation of results without ambiguity.

This chapter is devoted to study the electronic contributions to the Raman spectra of both Bernal and rhombohedral graphite. We first describe, in section 5.1, the electronic properties of N-layers Bernal and rhombohedral graphite using the tight binding formulation with the Slonczewski–Weiss–McClure (SWMcCLure) parametrisation [127, 128]. In section 5.2, we demonstrate that this leads to significant differences in the electronic contribution to the Raman spectra between crystals of the same thickness but with different layer arrangement: while the ERS signal is essentially featureless for ABA stacking, for ABC a series of peaks appears due to off-resonant electron-hole excitations from the n-th valence band to the n-th conduction band [129]. We finish discussing the experimental evidences that support our calculations.

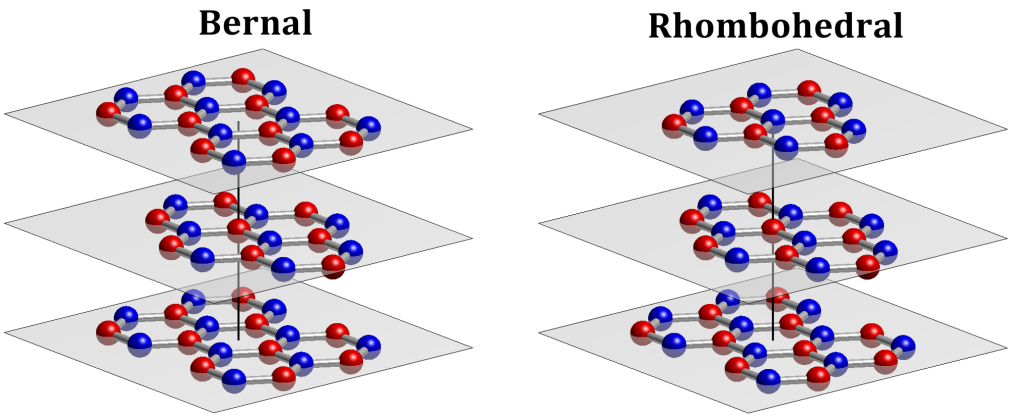

Figure 5.0.2: Pictorial representation of the atomic structure of Bernal and rhombohedral trilayer graphene. To guide the eye, we draw a vertical line from the centre of one hexagonal ring in the bottom-most layer. In Bernal stacking, it crosses the centre of another hexagonal ring from the top layer, whilst in rhombohedral, it crosses an atomic site of the A sub-lattice from the top layer.

5.1 Electronic dispersion of graphite

As we discussed in the second chapter, the main assumption behind the tight binding model is that the atomic orbitals of carbon atoms can be used as building blocks for the entire wave function of the crystal. This assumption, which provides a good picture for the description of the electronic properties in monolayer graphene, also holds for the interlayer description in graphite. The Bloch functions for N-layer graphite now take the form

$$\left|\varphi^{n}_{\lambda,\boldsymbol{k}}(\boldsymbol{r})\right\rangle = \sum_{\boldsymbol{R}} e^{i\boldsymbol{k}\cdot(\boldsymbol{R}+\boldsymbol{C}^{\mathrm{X}}_{n}+\Delta_{\lambda})}\varphi_{z}(\boldsymbol{r}-\boldsymbol{C}^{\mathrm{X}}_{n}-\Delta_{\lambda}-\boldsymbol{R}). \tag{5.1}$$

In this expression, the vectors Δ_{λ} and $\boldsymbol{R}$ were introduced in Eq. (2.4) of chapter 2, while the vector $\boldsymbol{C}^{\mathrm{X}}_{n}$, with X = ABA or ABC for Bernal and rhombohedral graphite, respectively, establishes the centre of the unit cell in the crystal in the

layer $n \in [1, N]$. For each configuration, they take the form

$$\boldsymbol{C}_n^{\mathrm{ABA}} = \left(0, a\frac{\mod\ (n-1,2)}{2}, (n-1)h_0\right), \tag{5.2a}$$

$$\boldsymbol{C}_n^{\mathrm{ABC}} = \left(0, a\frac{\mod\ (n-1,3)}{2}, (n-1)h_0\right). \tag{5.2b}$$

In these definitions, the operation $\mod\ (l, m)$ is the remainder after the division of l by m, and $h_0 \approx 3.35$Å is the interlayer distance.

To construct the Hamiltonian for graphite, we only take into account hybridisation on consecutive layers. Using the basis $\left\{\left|\varphi^1_{A,\boldsymbol{k}}(\boldsymbol{r})\right\rangle \left|\varphi^1_{B,\boldsymbol{k}}(\boldsymbol{r})\right\rangle \dots \left|\varphi^N_{B,\boldsymbol{k}}(\boldsymbol{r})\right\rangle\right\}$, the Hamiltonian of N-layers graphite reads

$$\mathcal{H}^{\mathrm{X}}_{\mathrm{N}}(\boldsymbol{k}) = \begin{pmatrix} \mathcal{H}_{\mathrm{G}}(\boldsymbol{k}) & \mathcal{T}^{\mathrm{X}}_{1,2}(\boldsymbol{k}) & 0 & \cdots & 0 & 0 \\ \mathcal{T}^{\mathrm{X}\,\dagger}_{1,2}(\boldsymbol{k}) & \mathcal{H}_{\mathrm{G}}(\boldsymbol{k}) & \mathcal{T}^{\mathrm{X}}_{2,3}(\boldsymbol{k}) & \cdots & 0 & 0 \\ 0 & \mathcal{T}^{\mathrm{X}\,\dagger}_{2,3}(\boldsymbol{k}) & \mathcal{H}_{\mathrm{G}}(\boldsymbol{k}) & \cdots & 0 & 0 \\ \vdots & \vdots & \vdots & \ddots & \vdots & \vdots \\ 0 & 0 & 0 & \cdots & \mathcal{H}_{\mathrm{G}}(\boldsymbol{k}) & \mathcal{T}^{\mathrm{X}}_{N-1,N}(\boldsymbol{k}) \\ 0 & 0 & 0 & \cdots & \mathcal{T}^{\mathrm{X}\,\dagger}_{N-1,N}(\boldsymbol{k}) & \mathcal{H}_{\mathrm{G}}(\boldsymbol{k}) \end{pmatrix}. \tag{5.3}$$

While the diagonal 2×2 block $\mathcal{H}_{\mathrm{G}}(\boldsymbol{k})$ describes the intralayer coupling and is the same for both types of configuration, the interlayer couplings $\mathcal{T}^{\mathrm{X}}_{n,n+1}(\boldsymbol{k})$ take different expressions in each configuration,

$$\mathcal{T}^{\mathrm{ABC}}_{\mathrm{i,i+1}}(\boldsymbol{k}) = \mathcal{T}(\boldsymbol{k}) \equiv \begin{pmatrix} \gamma_4 f(\boldsymbol{k}) & -\gamma_3 f^*(\boldsymbol{k}) \\ \gamma_1 & \gamma_4 f(\boldsymbol{k}) \end{pmatrix}, \tag{5.4a}$$

$$\mathcal{T}^{\mathrm{ABA}}_{\mathrm{i,i+1}}(\boldsymbol{k}) = \begin{cases} \mathcal{T}(\boldsymbol{k}) & \text{for i odd,} \\ \mathcal{T}^\dagger(\boldsymbol{k}) & \text{for i even.} \end{cases} \tag{5.4b}$$

The parameter $\gamma_1 = \left\langle \varphi^i_{B,\boldsymbol{k}}(\boldsymbol{r}) \right| \mathcal{H}^{\mathrm{X}}_{\mathrm{N}} \left| \varphi^{i+1}_{A,\boldsymbol{k}}(\boldsymbol{r}) \right\rangle \approx 0.39$ eV accounts for the coupling between atomic orbitals in the structure that lie directly on top of/beneath each other. Because it is the largest interlayer coupling constant, the atomic orbitals

bound by such hybridisation are often referred to as dimer sites. The other two coupling constants in Eq. (5.4) accounts for the skew AA, AB, and BB interlayer hybridisation, and they are defined as

$$\gamma_3 = -\left\langle \varphi^i_{A,\boldsymbol{k}}(\boldsymbol{r}) \right| \mathcal{H}^{\mathrm{X}}_{\mathrm{N}} \left| \varphi^{i+1}_{B,\boldsymbol{k}}(\boldsymbol{r}) \right\rangle , \tag{5.5a}$$

$$\gamma_4 = \left\langle \varphi^i_{A,\boldsymbol{k}} \right| \mathcal{H}^{\mathrm{X}}_{\mathrm{N}} \left| \varphi^{i+1}_{A,\boldsymbol{k}} \right\rangle = \left\langle \varphi^i_{B,\boldsymbol{k}} \right| \mathcal{H}^{\mathrm{X}}_{\mathrm{N}} \left| \varphi^{i+1}_{B,\boldsymbol{k}} \right\rangle . \tag{5.5b}$$

There is not a strong experimental consensus on the actual value for these parameters in bilayer [130–133], trilayer [134] or graphite [135], so for this chapter we take the parameters used in [129], $\gamma_3 = 0.26$ eV and $\gamma_4 = 0.2$ eV. Notice that other parameters that couple non-adjacent layers, denoted by γ_2 and γ_5 in the literature, are about two orders of magnitude smaller than γ_1 [136], and therefore will not be taken into account in our calculations.

In the spirit of the k dot p approximation, we expand $f(\boldsymbol{k})$ in Eq. (5.4) around the $\boldsymbol{K}_\xi$, and take only linear terms in momentum, $\boldsymbol{p} = \hbar\boldsymbol{k} - \hbar\boldsymbol{K}_\xi$. The resulting interlayer coupling captures the low energy physics of graphite around the CNP and is written as

$$\mathcal{T}(\boldsymbol{p}) \approx \begin{pmatrix} -v_4(\xi p_x - i p_y) & v_3(\xi p_x + i p_y) \\ \gamma_1 & -v_4(\xi p_x - i p_y) \end{pmatrix} , \tag{5.6}$$

where we introduce $v_{3,4} = \frac{\sqrt{3}a}{2\hbar}\gamma_{3,4}$. Again, we neglect the overlap between atomic orbitals centred at different positions, $\left\langle \varphi^n_\lambda \right| \left. \varphi^m_{\lambda'} \right\rangle = \delta_{n,m}\delta_{\lambda,\lambda'}$, and the eigenvalue problem of the Schrödinger equation comes down to the diagonalisation of the matrix in Eq. (5.3), which we perform numerically.

Our discussion starts with the simplest form of graphite, bilayer graphene. Its electronic dispersion, shown in Fig. 5.0.1(a), consists of four parabolic bands around $\boldsymbol{K}_\xi$, two of them emerging from the charge neutrality point and the other two shifted by $\pm\gamma_1$, a consequence of the coupling between the dimer sites. Accordingly, we observe step-like features in the density of states at $E = \pm\gamma_1$. The effect of the other coupling constants is more subtle, but give rise to noteworthy features in the

dispersion at energies $\sim$ 1 meV. In particular, γ_3 introduces a trigonal warping in all four parabolic bands and is also responsible for the emergence of three replicas of the Dirac cone around $\boldsymbol{K}_\xi$, which changes the topology of the constant energy contours at $\sim$ 1 meV. This peculiarity is referred to as a Lifshitz transition [137] and has been a topic of intense research in bilayer graphene [138–141], among other reasons, because it results in saddle points in the dispersion and sharp peaks in the density of states. In turn, γ_4 introduces electron-hole asymmetry in the dispersion, widening the parabolic valence bands and narrowing those in the conduction side. This difference in the parabolic constants in the bands translates into a step-like feature in the density of states at the charge neutrality point (Fig. 5.0.1b). Adding a third layer to this system yields two qualitatively different electronic dispersions around the $\boldsymbol{K}_\xi$ valleys. The ABA configuration features two parabolic and two linear bands emerging from the charge neutrality point, and the latter with a Fermi velocity equal to that of monolayer graphene. There are one conduction and one valence band, emerging from $\pm\sqrt{2}\gamma_1$, outside of the energy range presented in Fig. (5.0.2a). ABC stacking, on the other hand, exhibits two cubic bands, emerging from the origin, and two pairs of bands crossing at $\pm\gamma_1$. Interestingly, the second conduction and valence bands feature a Mexican-hat like dispersion, with saddle points in a circle around the $\boldsymbol{K}_\xi$ point, which enhances the density of states with the formation of van Hove singularities.

We present the dispersion, together with the density of states, of a graphitic film with 10 layers in both Bernal and rhombohedral configuration in Fig. 5.1.3. In general, Bernal-stacked graphite has $\lfloor \frac{N}{2} \rfloor$ parabolic bands emerging from the charge neutrality point and $\lfloor \frac{N}{2} \rfloor$ parabolic bands shifted from it, in both the valence and conduction side ($\lfloor x \rfloor$ denotes the largest integer less or equal than x). Additionally, for N odd, the dispersion contains two Dirac-like bands with Fermi velocity exactly equal to v. On the other hand, the electronic spectrum of rhombohedral-stacked graphite contains one pair of bands almost dispersionless around the charge neutrality point, in a trigonally warped circle of radius γ_1/v around $\hbar\boldsymbol{K}_\xi$. Interestingly,

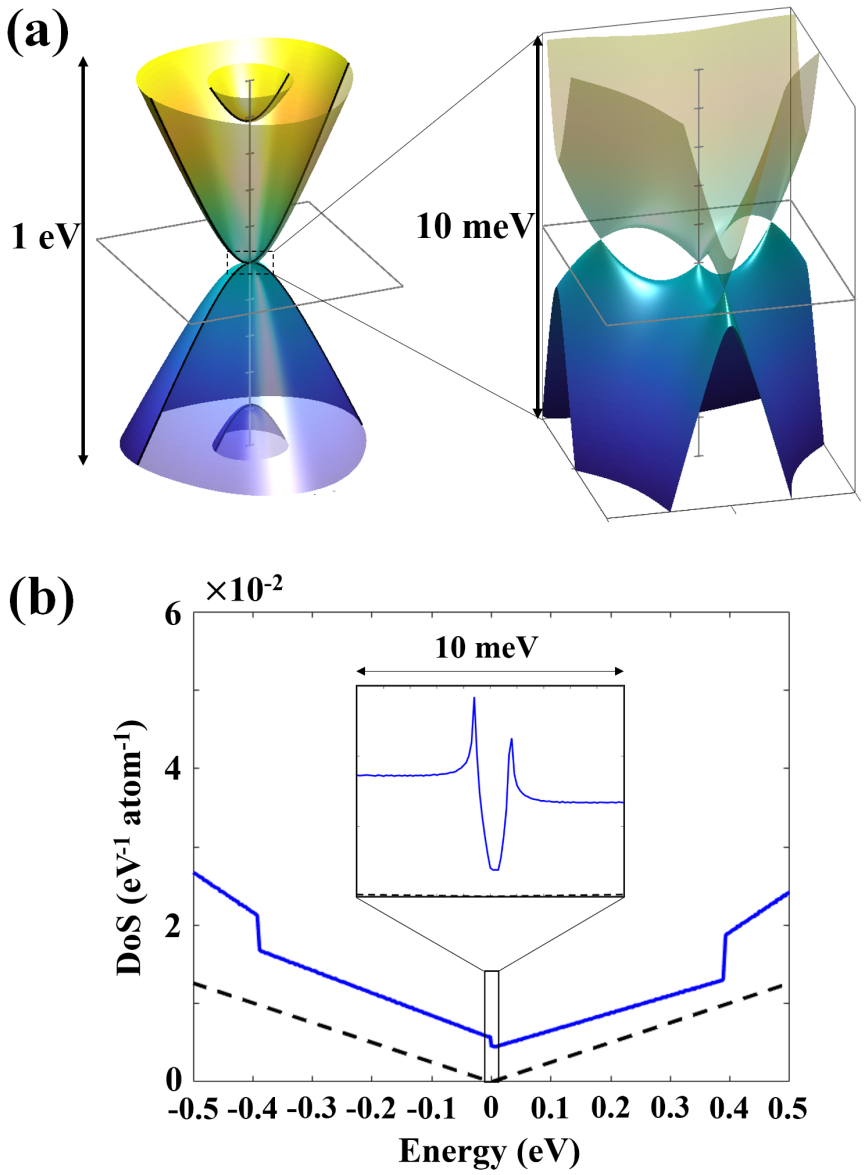

Figure 5.1.1: (a) Band structure of Bernal bilayer graphene around the $\boldsymbol{K}_+$ valley, on the left (right) within an energy window of 1 eV (10 meV) and a square in reciprocal space $10^{-1}\,\text{Å}^{-1} \times 10^{-1}\,\text{Å}^{-1}$ ($6 \cdot 10^{-3}\,\text{Å}^{-1} \times 6 \cdot 10^{-3}\,\text{Å}^{-1}$), and the marks on the z-axis represent intervals of 100 meV (1 meV). (b) Density of states of Bernal bilayer graphene (blue solid line) together with that of monolayer graphene (in dashed black lines). In the inset, the two vHSs, which originate from the saddle points in the low-energy dispersion, are a consequence of the Lifshitz transition.

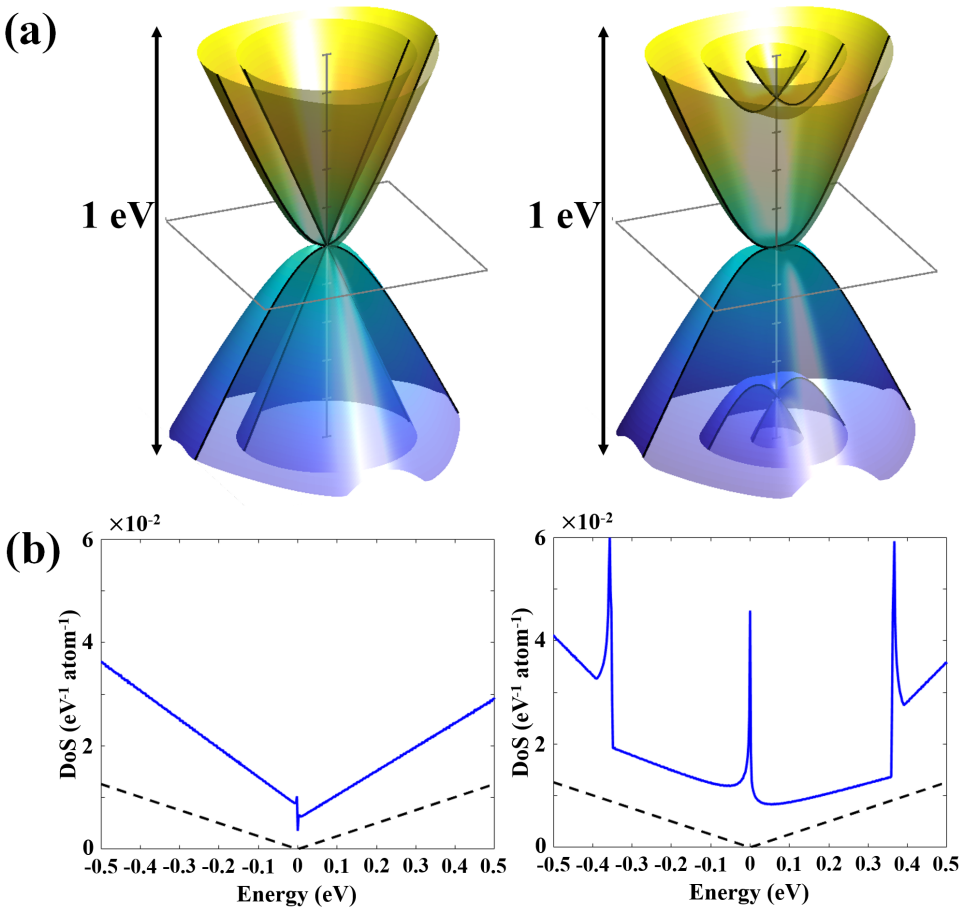

Figure 5.1.2: (a) Band structure of ABA (left) and ABC (right) trilayer graphene around the $\boldsymbol{K}_+$ valley, within an energy window of 1 eV and a square in reciprocal space 10^{-1} Å^{-1} × 10^{-1} Å^{-1}. Notice that the electron-hole asymmetry caused by γ_4 becomes apparent with the chosen values for energy and wavenumber window: while the conduction band fits, the lowest part of the valence band exceeds slightly the square perimeter. (b) Density of states for ABA (left) and ABC (right) trilayer graphene (solid blue line), alongside with the density of states of monolayer graphene (dashed lines). The electron-hole asymmetry increases the number of states in the valence side in both configurations.

the amplitude of the eigenvectors associated with these flat bands is confined in the outermost layers. This can be shown approximating the Hamiltonian of rhombohedral graphite for values of $|\boldsymbol{p}| \ll \gamma_1/v$,

$$\mathcal{H}^{\mathrm{ABC}} \approx \begin{pmatrix} 0 & 0 & 0 & 0 & \cdots & 0 & 0 & 0 \\ 0 & 0 & \gamma_1 & 0 & \cdots & 0 & 0 & 0 \\ 0 & \gamma_1 & 0 & 0 & \cdots & 0 & 0 & 0 \\ 0 & 0 & 0 & 0 & \cdots & 0 & 0 & 0 \\ \vdots & \vdots & \vdots & \vdots & \ddots & \vdots & \vdots & \vdots \\ 0 & 0 & 0 & 0 & \cdots & 0 & \gamma_1 & 0 \\ 0 & 0 & 0 & 0 & \cdots & \gamma_1 & 0 & 0 \\ 0 & 0 & 0 & 0 & \cdots & 0 & 0 & 0 \end{pmatrix}, \tag{5.7}$$

which contains two eigenvectors with zero energy with amplitude in the A sublattice of the top layer and B sublattice of the bottom layer, the only two non-dimer sites of the structure. The remaining $N-1$ pairs of bands cross at $\pm\gamma_1$ and the amplitude of their eigenvectors spans all the layers, which confirms their status as bulk bands. From this set, one finds $\lfloor \frac{N-1}{2} \rfloor$ bands featuring a Mexican-hat like dispersion, with saddle points in a trigonally warped circle around $\boldsymbol{K}_\xi$. One can estimate the energy position of the van Hove singularities by neglecting γ_3 and γ_4. In this case, saddle points of the first bulk bands around the CNP are located at the edges of the bands, in a circle around $\hbar\boldsymbol{K}_\xi$. For large number of layers, the radius of such circle is $p_0 = \gamma_1/v$, and one can study the dispersion at these points by evaluating

the eigenvalues of the Hamiltonian in Eq. (5.3) at $\boldsymbol{p} = (p_0, 0)$,

$$\mathcal{H} \approx \begin{pmatrix} 0 & \gamma_1 & 0 & 0 & \cdots & 0 & 0 & 0 \\ \gamma_1 & 0 & \gamma_1 & 0 & \cdots & 0 & 0 & 0 \\ 0 & \gamma_1 & 0 & \gamma_1 & \cdots & 0 & 0 & 0 \\ 0 & 0 & \gamma_1 & 0 & \cdots & 0 & 0 & 0 \\ \vdots & \vdots & \vdots & \vdots & \ddots & \vdots & \vdots & \vdots \\ 0 & 0 & 0 & 0 & \cdots & 0 & \gamma_1 & 0 \\ 0 & 0 & 0 & 0 & \cdots & \gamma_1 & 0 & \gamma_1 \\ 0 & 0 & 0 & 0 & \cdots & 0 & \gamma_1 & 0 \end{pmatrix}, \tag{5.8}$$

which can be analytically diagonalised giving energies [142]

$$E_\beta^n(\boldsymbol{p}_0) = 2\beta\gamma_1 \sin\left[\frac{(2n+1)\pi}{2(2N+1)}\right], \tag{5.9}$$

with $\beta = \pm 1$ labelling the conduction ($\beta = +1$) and valence($\beta = -1$) and $n \in [1, 2, \ldots, N/2]$ ($(N-1)/2$ for odd N). The shape of each of these bands is tantalisingly similar to the quasiparticle spectrum obtained in the previous chapter, which feeds expectations for finding enhanced ERS due to electronic transitions.

5.2 Theoretical description of ERS in graphite

To determine the scattering amplitude for electronic Raman processes in graphite, we proceed as in previous chapters and replace $\boldsymbol{p} \to \boldsymbol{p} - e\boldsymbol{A}$ in Eq. (5.3) to obtain the light-matter interaction term

$$\mathcal{V}(\boldsymbol{r}, t) = \frac{e}{\hbar} \begin{pmatrix} \mathcal{H}_G(\boldsymbol{A}) & \mathcal{T}_{1,2}(\boldsymbol{A}) & \cdots & 0 \\ \mathcal{T}_{1,2}^\dagger(\boldsymbol{A}) & \mathcal{H}_G(\boldsymbol{A}) & \cdots & 0 \\ \vdots & \vdots & \ddots & \vdots \\ 0 & 0 & \cdots & \mathcal{H}_G(\boldsymbol{A}) \end{pmatrix}. \tag{5.10}$$

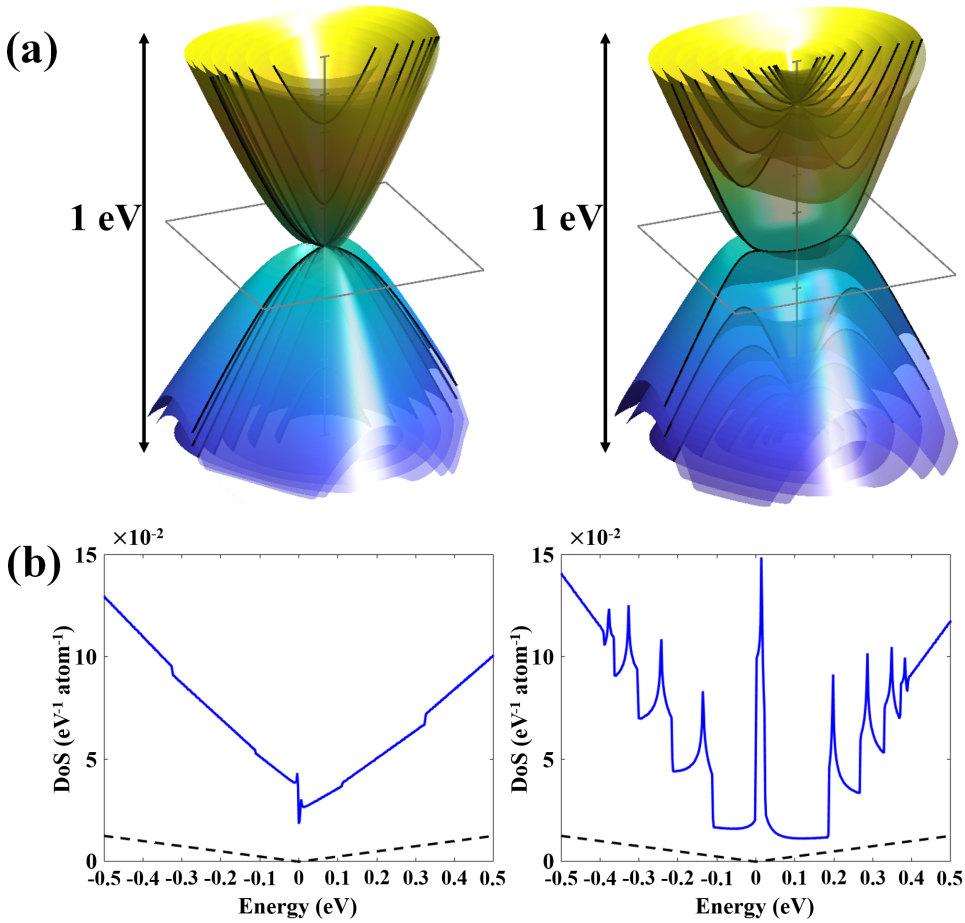

Figure 5.1.3: (a) Band structure of 10-layers Bernal (left) and 10 layers rhombohedral graphite (right) within an energy window of 1 eV in a 10^{-1}Å$^{-1} \times 10^{-1}$Å^{-1} square around the $\boldsymbol{K}_+$ point. As described in the text, rhombohedral graphite features two nearly flat bands around the origin. (b) Density of states of 10-layers Bernal (left) and rhombohedral (right) graphite, in solid blue lines. For comparison, the density of states for monolayer graphene is also displayed in black dashed lines. The flat bands result in a strong contribution to the density of states around the charge neutrality point.

We demonstrated in chapter 3 that the two-steps processes are responsible for the leading contribution to the ERS in graphene. Graphite inherits such property and therefore we only take linear terms in $\boldsymbol{A}$ into account in the equation above. Furthermore, because the diagonal 2×2 blocks are proportional to v, one order of magnitude larger than the coefficients v_3 and v_4, we can neglect the off-diagonal 2×2 blocks, which reduces the structure of the light-matter interaction term to

$$\mathcal{V}^{\mathrm{L}}(\boldsymbol{r}, t) = ev\boldsymbol{I}_N \otimes \sigma \cdot \boldsymbol{A}, \tag{5.11}$$

where $\boldsymbol{I}_N$ is the N-dimensional identity matrix. We discussed in chapter 2 that, in a two-steps process, the absorption of the incoming photon can take place at times t_1 or t_2, while the scattered one is emitted at t_2 or t_1, respectively. The difference in energy between these photons, $\omega = \Omega - \tilde{\Omega}$, is equal to the excitation energy of the resulting electron-hole pair left in the crystal, $E_{\mathrm{e}}^{+} - E_{\mathrm{h}}^{-}$, "e" and "h" being the band index of the electron and the hole, respectively. Between t_1 and t_2, the virtual quantum state of the system is characterised by absence of photons and by one intermediate electronic state. For the two-band dispersion of pristine graphene, such virtual electronic state could be a Fermi sea of electrons or the Fermi sea with an electron-hole pair. However the band structure of graphite has N fully occupied valence bands, and N empty conduction bands, which enables $2N$ intermediate virtual states. This introduces a subtlety that requires the use of second quantization. This time, for the sake of simplicity, we denote $\hat{c}_{\beta b}$ ($\hat{c}^{\dagger}_{\beta b}$) as the operator that destroys (creates) one electron in band "b" in the valence ($\beta = -$) or conduction ($\beta = +$) band. When the intermediate state contains a hole in the band "h" and one electron in the band "v" (left side of Fig. 5.2.1), the order of electronic operators follows $\hat{c}^{\dagger}_{+\mathrm{e}}\hat{c}_{+v}\hat{c}^{\dagger}_{+v}\hat{c}_{-\mathrm{h}}$. Furthermore, when the intermediate quantum state is the Fermi sea, the ERS process follows the same order, $\hat{c}^{\dagger}_{+\mathrm{e}}\hat{c}_{-\mathrm{h}}\hat{c}^{\dagger}_{-\mathrm{h}}\hat{c}_{-\mathrm{h}}$. Conversely, when the intermediate state contains one electron in the band "e" and one hole in the band $v \neq \mathrm{h}$ (right side of Fig. 5.2.1), such order is $\hat{c}^{\dagger}_{-v}\hat{c}_{-\mathrm{h}}\hat{c}^{\dagger}_{+\mathrm{e}}\hat{c}_{-v}$. Importantly, the latter swaps the order in which the final electron-hole pair is created-annihilated, which results in a relative minus sign, due to the anticommutative na-

ture of fermions. The Raman amplitude, therefore, is given by

$$\begin{aligned}
\langle s_{\mathrm{f}}|\,\mathcal{R}^{\mathrm{L}}\,|s_{\mathrm{i}}\rangle &= \sum_{\nu}\frac{1}{i\hbar}\int_{-\frac{T}{2}}^{\frac{T}{2}}\langle s_{\mathrm{f}}|\,\mathcal{V}(\boldsymbol{r}_2,t_2)\,|s_\nu\rangle\,\frac{1}{i\hbar}\int_{-\frac{T}{2}}^{t_2}\langle s_\nu|\,\mathcal{V}(\boldsymbol{r}_1,t_1)\,|s_{\mathrm{i}}\rangle = \qquad (5.12)\\
&= -\frac{e^2v^2}{2\varepsilon_0\sqrt{\Omega\tilde{\Omega}}}\sum_{\mathrm{v}}\int_{-\frac{T}{2}}^{\frac{T}{2}}\mathrm{d}t_2 e^{\frac{i}{\hbar}(E_{\mathrm{e}}^{+}-E_{\mathrm{v}}^{+})t_2}\int_{-\frac{T}{2}}^{t_2}\mathrm{d}t_1 e^{\frac{i}{\hbar}(E_{\mathrm{v}}^{+}-E_{\mathrm{h}}^{-})t_1}\delta\left(\frac{\boldsymbol{p}_{\mathrm{i}}-\boldsymbol{p}_{\mathrm{f}}}{\hbar}\right)\\
&\langle +,\mathrm{e}|\left[e^{\frac{i}{\hbar}\tilde{\Omega}t_2}(\boldsymbol{I}_N\otimes\sigma\cdot\tilde{\boldsymbol{l}}^{*})\,|+,\nu\rangle\,\langle +,\nu|\,(\boldsymbol{I}_N\otimes\sigma\cdot\boldsymbol{l})e^{-\frac{i}{\hbar}\Omega t_1}\right.\\
&\qquad\left.+e^{-\frac{i}{\hbar}\Omega t_2}(\boldsymbol{I}_N\otimes\sigma\cdot\boldsymbol{l})\,|+,\nu\rangle\,\langle +,\nu|\,(\boldsymbol{I}_N\otimes\sigma\cdot\tilde{\boldsymbol{l}}^{*})e^{\frac{i}{\hbar}\tilde{\Omega}t_1}\right]|-,\mathrm{h}\rangle\,+\\
&\qquad-\frac{e^2v^2}{2\varepsilon_0\sqrt{\Omega\tilde{\Omega}}}\int_{-\frac{T}{2}}^{\frac{T}{2}}\mathrm{d}t_2 e^{\frac{i}{\hbar}(E_{\mathrm{e}}^{+}-E_{\mathrm{h}}^{-})t_2}\int_{-\frac{T}{2}}^{t_2}\mathrm{d}t_1 e^{\frac{i}{\hbar}(E_{\mathrm{h}}^{-}-E_{\mathrm{h}}^{-})t_1}\delta\left(\frac{\boldsymbol{p}_{\mathrm{i}}-\boldsymbol{p}_{\mathrm{f}}}{\hbar}\right)\\
&\langle +,\mathrm{e}|\left[e^{\frac{i}{\hbar}\tilde{\Omega}t_2}(\boldsymbol{I}_N\otimes\sigma\cdot\tilde{\boldsymbol{l}}^{*})\,|-,\mathrm{h}\rangle\,\langle -,\mathrm{h}|\,(\boldsymbol{I}_N\otimes\sigma\cdot\boldsymbol{l})e^{-\frac{i}{\hbar}\Omega t_1}\right.\\
&\qquad\left.+e^{-\frac{i}{\hbar}\Omega t_2}(\boldsymbol{I}_N\otimes\sigma\cdot\boldsymbol{l})\,|-,\mathrm{h}\rangle\,\langle -,\mathrm{h}|\,(\boldsymbol{I}_N\otimes\sigma\cdot\tilde{\boldsymbol{l}}^{*})e^{\frac{i}{\hbar}\tilde{\Omega}t_1}\right]|-,\mathrm{h}\rangle\\
&\qquad+\frac{e^2v^2}{2\varepsilon_0\sqrt{\Omega\tilde{\Omega}}}\sum_{\nu\neq\mathrm{h}}\int_{-\frac{T}{2}}^{\frac{T}{2}}\mathrm{d}t_2 e^{\frac{i}{\hbar}(E_{\nu}^{-}-E_{\mathrm{h}}^{-})t_2}\int_{-\frac{T}{2}}^{t_2}\mathrm{d}t_1 e^{\frac{i}{\hbar}(E_{\mathrm{e}}^{+}-E_{\nu}^{-})t_1}\delta\left(\frac{\boldsymbol{p}_{\mathrm{i}}-\boldsymbol{p}_{\mathrm{f}}}{\hbar}\right)\\
&\langle -,n_\nu|\left[e^{\frac{i}{\hbar}\tilde{\Omega}t_2}(\boldsymbol{I}_N\otimes\sigma\cdot\tilde{\boldsymbol{l}}^{*})\,|-,\mathrm{h}\rangle\,\langle +,\mathrm{e}|(\boldsymbol{I}_N\otimes\sigma\cdot\boldsymbol{l})e^{-\frac{i}{\hbar}\Omega t_1}\right.\\
&\qquad\left.+\;e^{-\frac{i}{\hbar}\Omega t_2}(\boldsymbol{I}_N\otimes\sigma\cdot\boldsymbol{l})\,|-,\mathrm{h}\rangle\,\langle +,\mathrm{e}|(\boldsymbol{I}_N\otimes\sigma\cdot\tilde{\boldsymbol{l}}^{*})e^{\frac{i}{\hbar}\tilde{\Omega}t_1}\right]|-,\nu\rangle\,.
\end{aligned}$$

Above, we introduced the notation $|\beta,b\rangle$ to denote an eigenvector of the Hamiltonian in Eq. (5.3) in the band defined by β and "b". Notice that the third term carries opposite sign due to the aforementioned swapped order of electron creation and annihilation operators. The two terms inside each squared bracket accounts for the two possible orders in which the incident and outgoing photon are absorbed and emitted, respectively. After the integration over time t_1, we obtain factors proportional to $(\pm\Omega+\Delta E)^{-1}$, where ΔE is an energy difference between two electronic states belonging to different bands in the spectrum. Typically, the laser beam used in Raman experiments is $\Omega\sim 2$ eV, about one order of magnitude larger than such difference around the $\boldsymbol{K}_\xi$ points. Therefore, we approximate the resulting prefactors in the integrals over t_1 as $\pm\Omega^{-1}$, which is equivalent to take

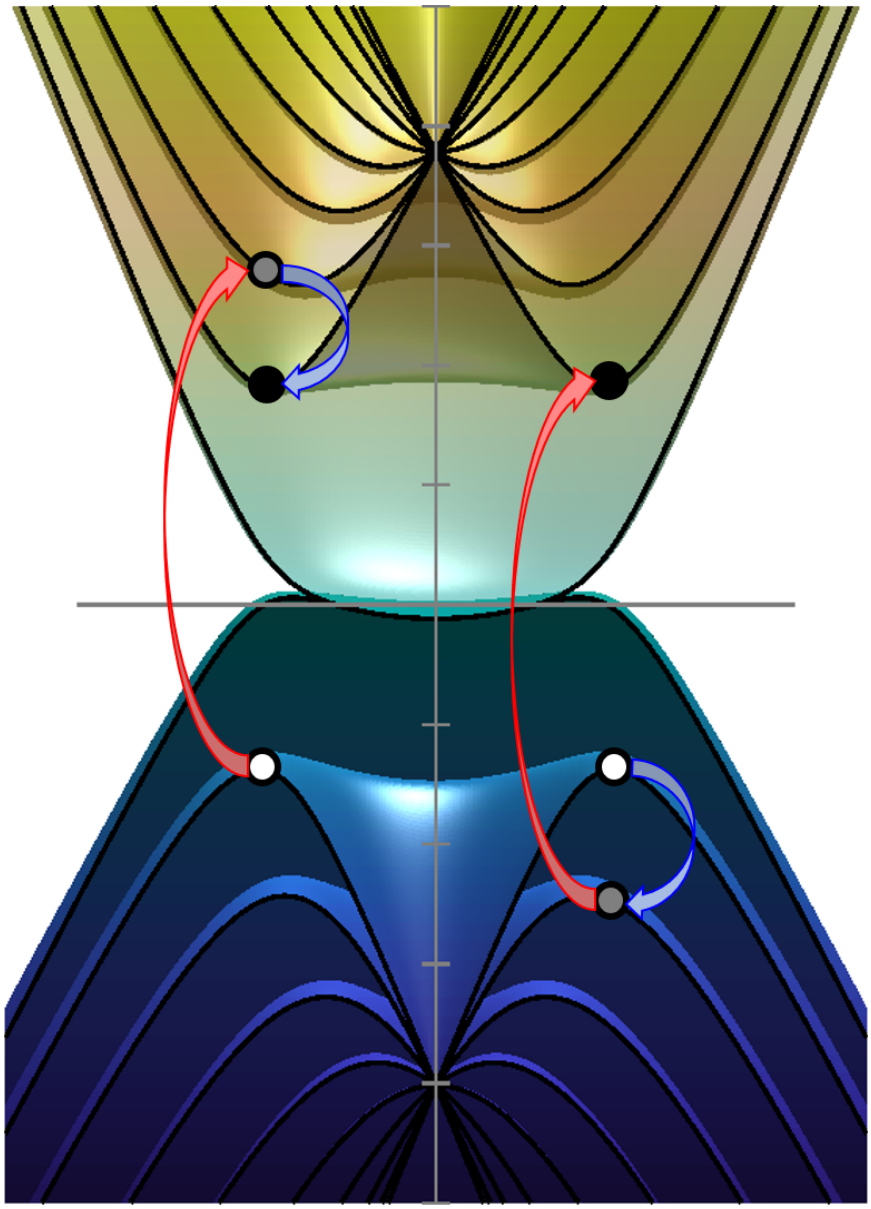

Figure 5.2.1: Pictorial representations of two types of two-steps processes resulting in a hole in the first bulk valence band and one electron in the first bulk conduction band. Red and blue arrows represent electronic transitions at t_1 and t_2, respectively. In the vertical axis, ticks mark energy distances of 100 meV. The horizontal line represents the Fermi level.

the exponential factors in lines two, five, and eight equal to 1. Moreover, we can reorder the brackets in the last two lines of Eq. (5.13), which results in a projection over the electronic states $|-,\nu\rangle$,

$$\begin{aligned}\langle s_f|\,\mathcal{R}^L\,|s_i\rangle = &-\frac{e^2v^2}{\varepsilon_0\sqrt{\Omega\tilde{\Omega}}}\frac{\sin\left[(E_e^+-E_h^--\omega)\frac{T}{2\hbar}\right]}{E_e^+-E_h^--\omega}\\ &\sum_{\nu=1}^{N}\sum_{\beta=\pm1}\langle+,n_e|\left[-(\boldsymbol{I}_N\otimes\sigma\cdot\tilde{\boldsymbol{l}}^*)\,|\beta,\nu\rangle\,\langle\beta,\nu|\,(\boldsymbol{I}_N\otimes\sigma\cdot\boldsymbol{l})\frac{1}{\Omega}\right.\\ &\left.+\,(\boldsymbol{I}_N\otimes\sigma\cdot\boldsymbol{l})\,|\beta,\nu\rangle\,\langle\beta,\nu|\,(\boldsymbol{I}_N\otimes\sigma\cdot\tilde{\boldsymbol{l}}^*)\frac{1}{\Omega}\right]|-,n_h\rangle\,.\end{aligned} \tag{5.13}$$

The sum over β and ν now completes the identity in the two terms inside the square bracket, which yields again the commutator of two operators that give the third Pauli matrix

$$\langle s_f|\,\mathcal{R}^L\,|s_i\rangle = \frac{\xi\hbar^2e^2v^2}{\varepsilon_0\Omega^2}\frac{\sin\left[(E_e^+-E_h^--\omega)\frac{T}{2\hbar}\right]}{E_e^+-E_h^--\omega}\,\langle+,n_e|\,\boldsymbol{I}_N\otimes\sigma_z\,|-,n_h\rangle\,(\boldsymbol{l}\times\tilde{\boldsymbol{l}}^*)_z \tag{5.14}$$

This result is central in this chapter, as it provides a simple route to compute the Raman amplitude by computing the matrix element $\boldsymbol{I}_N\otimes\sigma_z$ between the initial and final states, which we compute numerically. This, in turn, allows us to compute the angle-resolved Raman probability and the spectral density $g(\omega)$.

The starting point for our discussions starts in Fig. (5.2.2), showing the ERS spectrum of undoped bilayer graphene. The overall spectrum is linear over the range of energies $\sim$ 0.1 eV, with a step at $\omega \approx 0$. This picture, which is a consequence of the asymptotically linear density of states, only changes at very low energies, where a spike at $\omega \approx 2$ meV emerges, a manifestation of the saddle points caused by the Lifshitz transition. Notice that there is no ERS signal at $\omega = \gamma_1$, which would originate from electronic transitions that connect the top of the first (second) valence band with the bottom of the second (first) conduction band. This is a consequence of the matrix element $\langle+,2|\,\boldsymbol{I}_2\otimes\sigma_z\,|-,1\rangle$ ($\langle+,1|\,\boldsymbol{I}_2\otimes\sigma_z\,|-,2\rangle$), which identically vanishes at $p = 0$ [143].

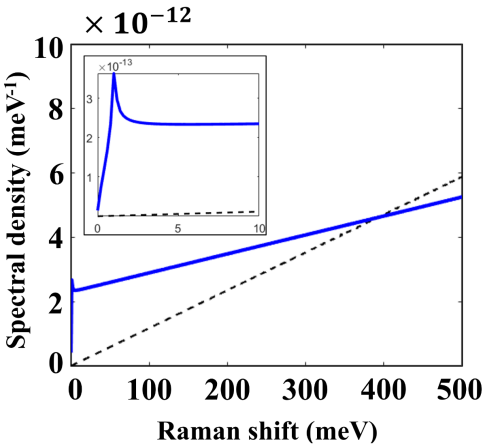

Figure 5.2.2: Spectral density of ERS for bilayer graphene in cross-linear polarisation (solid blue line). The inset represents the low energy ($<$ 10 meV) region, featuring a peak that originates from electronic transitions connecting vHSs around the charge neutrality point, at a Lifshitz transition point. To highlight the effect of the coupling, we present the spectral density of monolayer graphene multiplied by 2, plotted in black dashed line.

Adding a third layer, in either Bernal or rhombohedral configuration, barely changes the overall ERS spectrum in the energy range that we display. Both stacking orders exhibit a kink at low energies, but while in ABA-trilayer graphene there are two pairs of bands touching at the charge neutrality point that are parabolic and linear, in ABC-trilayer graphene there is only one pair of bands with cubic dispersion. As a result, we observe an enhancement of the ERS signal at $\omega \approx 0$ in the latter. The distinctive spectral features in the density of states of ABA and ABC configurations, steps and vHSs, respectively (see Fig. 5.1.2), could only lead to differences in their ERS spectra only at much higher energies around $\sim$ 1 eV.

In Fig. 5.2.4, we simulate the ERS spectra of 10-layers Bernal and rhombohedral graphite. In the Bernal configuration, the electronic transitions between the five bands below and above the neutrality point (plotted in the inset) generate a step at $\omega \approx 0$ followed by a linear trend with a small step at $\omega \sim 220$ meV. This is due to transitions from the first split valence to the first split conduction band, which

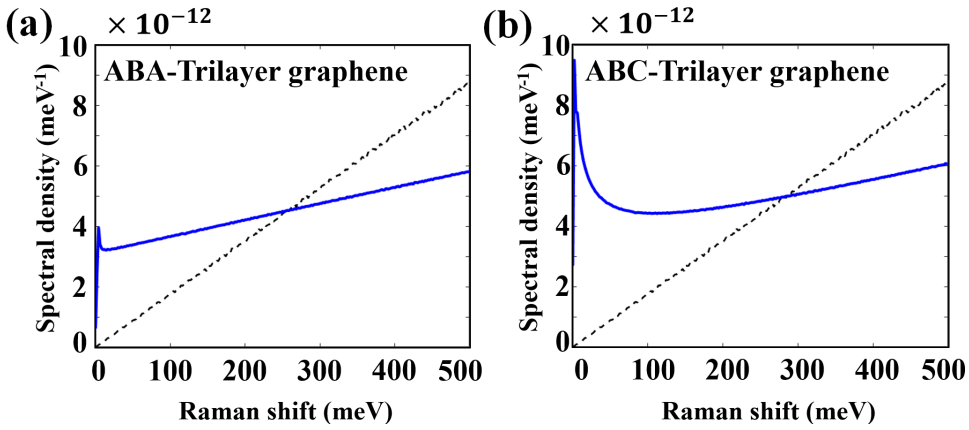

Figure 5.2.3: Spectral density of ERS for Bernal (a) and rhombohedral (b) trilayer graphene in the cross-linear polarisation (solid blue line). Aside from a pek at $\omega \approx 0$, both spectra are featureless. To highlight the effect of the interlayer coupling, we also plot the spectral density of monolayer graphene multiplied by 3 (black dashed lines).

start contributing linearly to the ERS signal. Notice that, as in bilayer graphene, only electronic transitions from the n-th split valence to the n-th split conduction band are allowed. The spectrum of 10-layers rhombohedral graphite is utterly different. It features Pauli blocking at low energies, which is a consequence of the peculiar topology of the Fermi surface at the CNP. The nearly flat conduction band actually crosses the Fermi level, giving rise to a circular electron pocket, and the nearly flat valence band rises, yielding a trigonally warped annulus of holes. The ERS spectrum of rhombohedral graphite contains also a sharp peak at $\omega \approx 350$ meV, which originates from transitions coming from the first bulk valence band to the first bulk conduction band. The shape of the peak is connected to the density of states: it features a step coming from electronic transitions at the band edges and one asymptote positioned at approximately the distance between vHSs (Fig. 5.1.3). For thicker graphitic films, we need to account for absorption effects by multiplying the contribution due to each layer by a factor of $\approx \sqrt{0.98^l}$, l being the number of layers above. As we increase the number of layers, both Bernal and

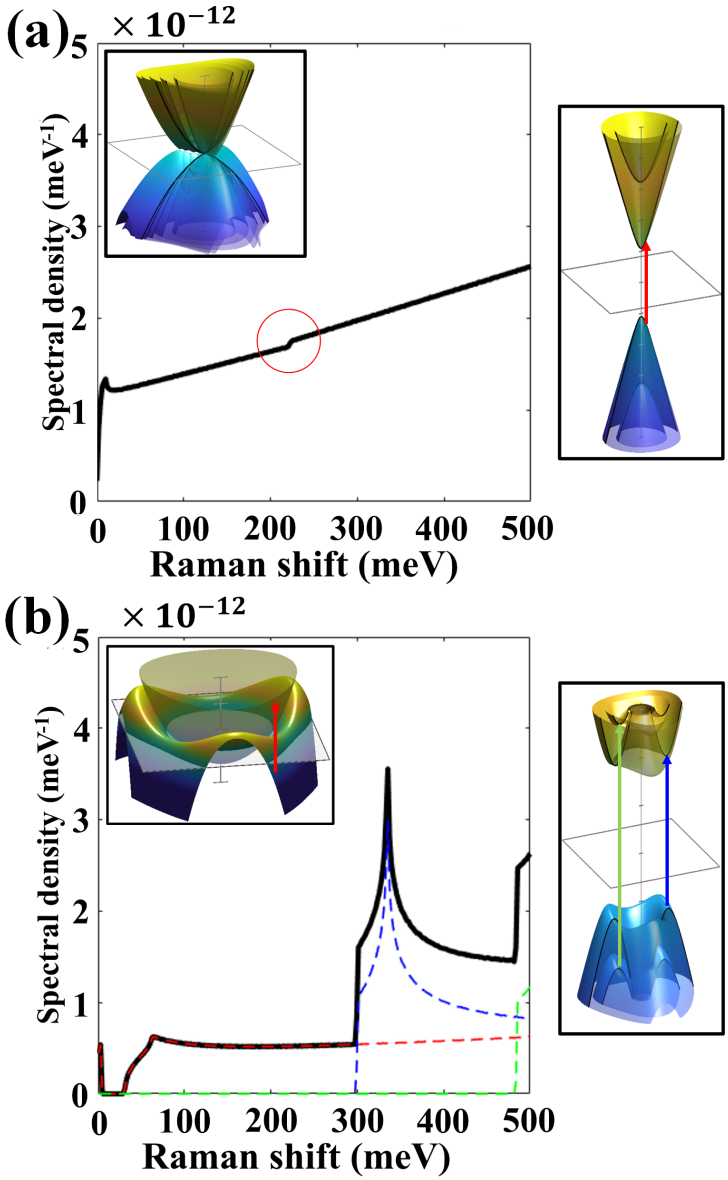

Figure 5.2.4: (a) Spectral density of ERS for 10-layers Bernal graphite in the cross-linear polarisation. This spectrum is essentially linear, with steps-like features corresponding to the creation of electron-hole pairs at the edges of the n-th valence and the n-th conduction bands (right). (b) The spectral density of ERS for 10-layers rhombohedral graphite in cross-linear polarisation. This spectrum originates from transitions between the flat bands (dashed red), first (dashed blue) and second (dashed green) bulk bands. Notice that transitions between flat bands (inset) are partially forbidden due to the Pauli blocking, yielding a step like feature at ~ 50 meV.

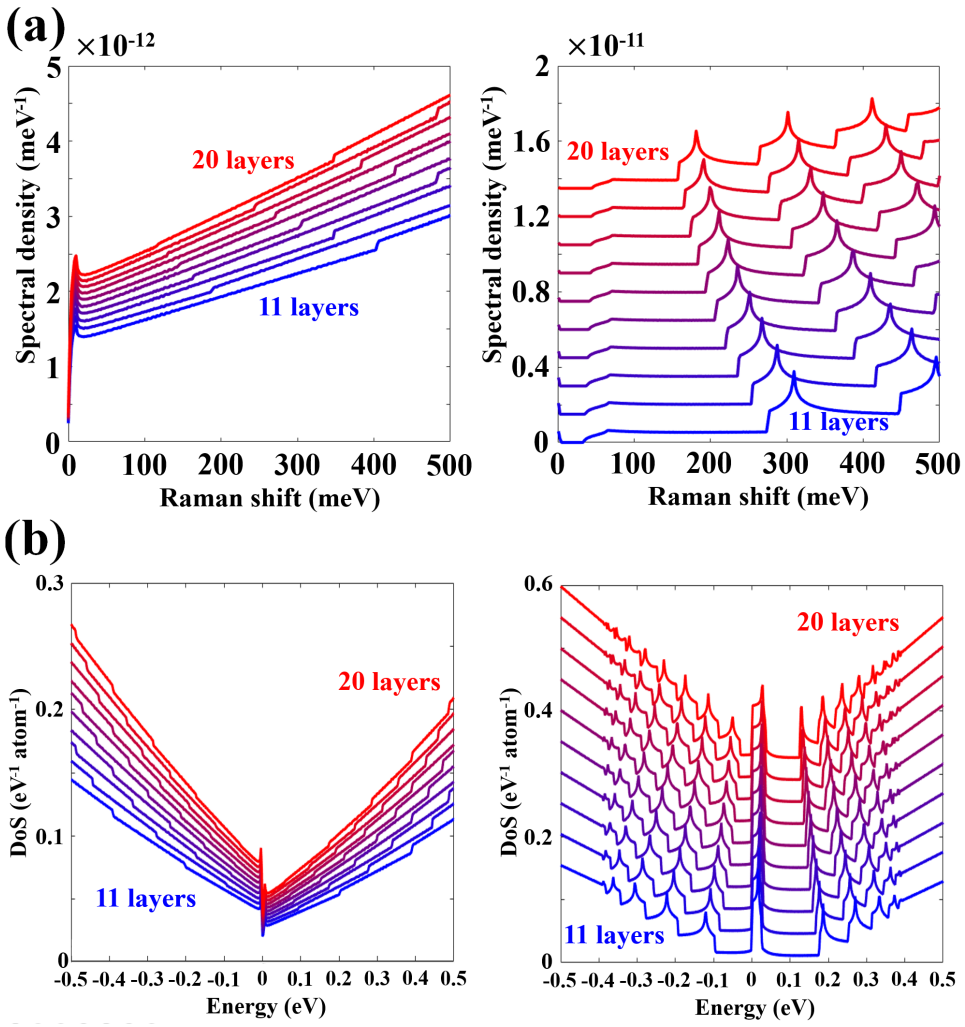

Figure 5.2.5: (a) Raman spectra for Bernal (left) and rhombohedral (right) graphite, with thickness ranging from 11 layers to 20. For the sake of clarity, we shifted each spectrum by $1.5 \cdot 10^{-12}$ meV^{-1} in the rhombohedral configuration. These spectra are in strong connection with their density of states, plotted in (b). For the rhombohedral graphite, each spectrum is shifted by 0.1eV^{-1} atom^{-1}.

rhombohedral graphite display their distinctive features at lower energies.

Despite the differences in the electronic Raman spectra of Bernal and rhombohedral graphite, we find that both split bands around $p \approx 0$ in Bernal graphite and all bands around $p = \gamma_1/v$ of rhombohedral graphite exhibit the same selection rule: only electronic transitions from the n-th valence band to the n-th conduction band can produce a Raman shift. This can be shown analytically by solving the eigenvalue problem of the d-dimensional Hamiltonian

$$H \approx \begin{pmatrix} 0 & \gamma_1 & 0 & \cdots & 0 & 0 \\ \gamma_1 & 0 & \gamma_1 & \cdots & 0 & 0 \\ 0 & \gamma_1 & 0 & \cdots & 0 & 0 \\ \vdots & \vdots & \vdots & \ddots & \vdots & \vdots \\ 0 & 0 & 0 & \cdots & 0 & \gamma_1 \\ 0 & 0 & 0 & \cdots & \gamma_1 & 0 \end{pmatrix}, \tag{5.15}$$

which is the approximate Hamiltonian for the dimer sites (split bands) in Bernal configuration at $p = 0$ (with $d = 2\lfloor \frac{N}{2} \rfloor$) and also the Hamiltonian for rhombohedral graphite at $\boldsymbol{p} = (\gamma_1/v, 0)$ (with $d = 2N$). The eigenvalue problem gives

$$E_a = -2\gamma_1 \cos\left(\frac{a\pi}{d+1}\right) \tag{5.16}$$

$$|a\rangle = \frac{1}{\mathcal{N}} \begin{pmatrix} -\sin(\frac{a\pi}{d+1}) \\ \sin(\frac{2a\pi}{d+1}) \\ \vdots \\ (-1)^k \sin(\frac{ka\pi}{d+1}) \\ \vdots \\ \sin(\frac{da\pi}{d+1}) \end{pmatrix}, \qquad a \in [1, d], \tag{5.17}$$

with $\mathcal{N}$ a normalisation factor. Now the selection rules emerges naturally when computing the bracket $\langle a' | \boldsymbol{I}_{d/2} \otimes \sigma_z | a \rangle = \delta_{a'+a,d+1}$, which in terms of our band indices is $\langle +, n' | \boldsymbol{I}_N \otimes \sigma_z | -, n \rangle = \delta_{n,n'}$.

5.3 Experimental evidence for ERS in graphite

To conclude this chapter, we review the experimental work and establish some connections with our results. For Bernal graphite, we can only expect a quasilinear increase of the Raman intensity at low energies, similar to what is observed in monolayer graphene, as the steps we predict barely increase the ERS contribution over the linear background. This was reported in [91], which is shown here in Figs. 5.3.1 (a) and (b), where they observed such linear trend together with the change in intensity with the polarisation. In the rhombohedral configuration, however, our simulations show a set of peaks, whose quantum efficiency can be numerically estimated as

$$I = \int_{\omega_0}^{\infty} \mathrm{d}\omega g(\omega) \sim 10^{-12}. \tag{5.18}$$

This quantity is about one order of magnitude smaller that the G peak [71], which, as stated in the previous chapters, suggests that it is indeed possible to observe ERS in graphite. In fact, there is one instance in the literature where such peak was detected in a sample of rhombohedral graphite with fifteen layers [144], which is plotted here in Fig. 5.3.1 (c) together with our simulated ERS spectrum in Fig. 5.3.1 (d). Moreover, the step and the position of the peak are in good agreement with our results.

In conclusion, the study of ERS in rhombohedral graphite is important for (at least) two reasons: not only it allows us to confirm its structural phase and characterise the number of layers in the sample, but it has also a potential for narrowing down the values of the hopping parameters by experimental fitting. The benefits of ERS are, of course, not restricted to graphite. This type of scattering is expected to be present in any graphene-based material featuring vHSs in its electronic dispersion, like twisted bilayer graphene.

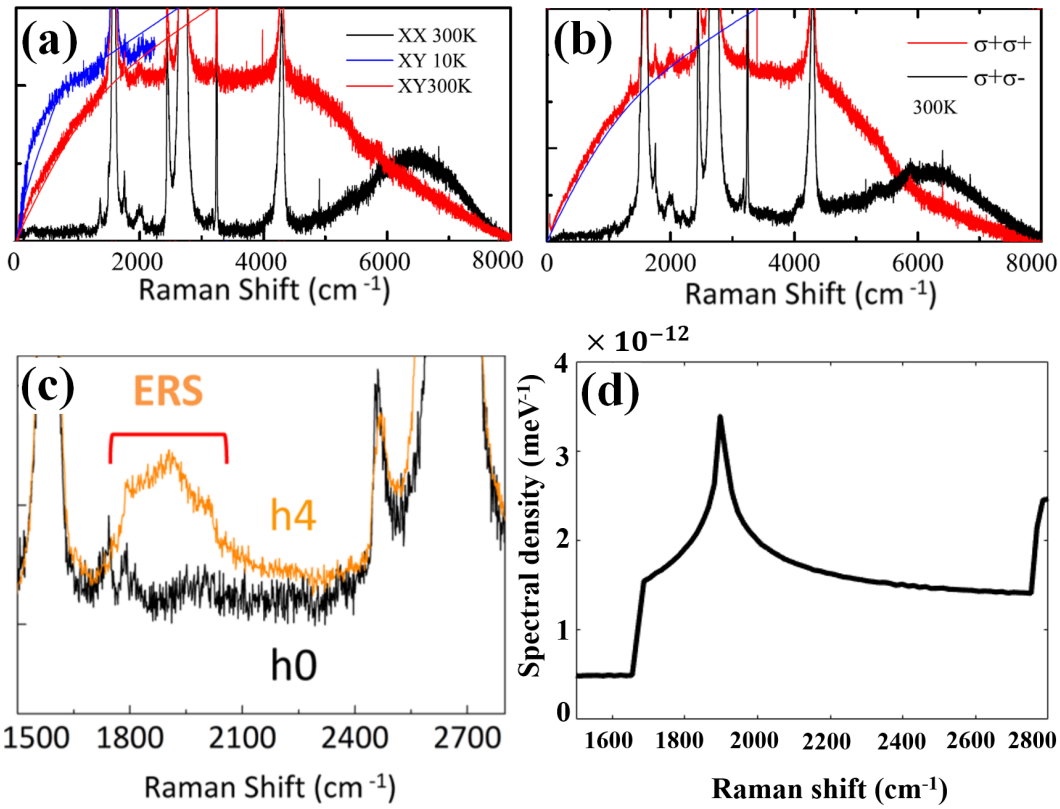

Figure 5.3.1: (a) and (b) Source: [91] Fig. 1. Polarisation resolved Raman spectra for Bernal graphite, with linear (a) and circular (b) polarisation. Authors did not specify the exact number of layers. (c) Source: [144] Fig. 2e. Polarisation resolved Raman spectra of 15 layers rhombohedral graphite in cross-linear (orange) and parallel-linear (black) configuration. The observed peak at $\sim$ 1900 cm^{-1} is a signature of electronic excitations from the first bulk valence band to the first bulk conduction band. (d) Simulated Raman spectrum in cross-linear polarisation for 15 layers rhombohedral graphite. The position of the peak is in good agreement with the experiment.

No story is worth telling without the twists and turns. Make them count instead.

Charlotte Eriksson

6

Electronic Raman scattering in twisted bilayer graphene

The superposition of two periodic structures yields the formation of patterns with a periodicity that can be orders of magnitude larger than that of their constituent components. These patterns were first exploited by the French textile industry, which they called "Moire textile". By pressing two layers of wet textile, they created such patterns, due to the superposition of two similar but imperfect threads, that remain after the fabric dries. However, despite the name of this pattern is etymologically linked to the textile industry, we find a plethora of examples in our everyday life where this phenomenon naturally arises, and sometimes even use this principle for applications: it is used by artists [145], to measure strains [146], to image defects in crystalline metals [147] or even in in the construction of moiré effect beacons for marine navigation [148].

Following the invention of the scanning tunnelling microscope (STM), experimentalists found yet another evidence for this phenomenon naturally occurring in our recently studied material, graphite, when the topmost layer is rotated with respect to the bulk [149]. The coupling between this layer and the bulk is characterised by the beating of two hexagonal graphene lattices. In the resulting triangular superlattice, with a much larger lattice constant, the stacking between the atoms of the top two layers in the structure (AA, AB or BA) also varies across the (moire) supercell, encompassing hundreds or even thousands of carbon atoms for small twist angles. This type of graphene materials is often called turbostratic graphite, and the simplest member of such family, twisted bilayer graphene (tBLG), will be the focus of this chapter.

Scientists have gained a deep understanding of the underlying physics of tBLG over the last decade [150–155]. Theorists predicted the emergence of saddle points in the electronic dispersion, and the consequent vHSs in the density of states. They suspected that tBLG could harbor new strongly correlated orders after tuning the Fermi energy at the level of these vHSs, as it is understood that electron-electron interactions, however weak, can be enhanced by a phenomenon known as nesting [156]. Additionally, as opposed to monolayer graphene, where the concentration needed to shift the Fermi level up to its natural vHS at the M point is about $\sim 10^{15}$ cm^{-2}, in tBLG the electron concentration required to tune the Fermi level at the vHS closest from the charge neutrality point (CNP) is about three orders of magnitude smaller, a level of dilution experimentally achievable by gating. Moreover, as the twist angle decreases, the energy position of these vHSs approaches the CNP and the first conduction and valence bands begin to flatten. At certain twist angles, now known as "magic angles", the first bands below and above the CNP become flat, which further raised hopes for observing strongly correlated phenomena.

In April 2018, we witnessed a *twist* of fate in the history of this material, when a group in Massachusetts institute of technology lead by Pablo Jarillo-Herrero reported superconducting and correlated insulating behaviour in tBLG samples for angles slightly over 1° [157, 158]. Moreover, they found that the phase diagram

of tBLG is phenomenologically similar to that of high-temperature superconductors, which suggests that the underlying mechanisms for such phenomena could be linked. Since then, the interest on this material has been reignited and research groups all around the world have joined forces to answer the open questions that still remain unanswered in the fast-growing field of twisted bilayer graphene.

In this context, the present chapter aims to study the electronic contribution to the Raman spectrum in tBLG. We review in the second section the two most widely used theoretical approaches for tBLG, namely, the tight-binding model and the continuum model. We employ the latter to compute the electronic contribution to the Raman spectrum in small-angle tBLG in the third section, which represents the main body of our results. We observe a qualitative change in the Raman spectra above and below the magic angle, which is in connection with a change in the flatness of the first bands below and above the charge neutrality point. We finish this chapter by putting our work in its experimental context and discussing how attainable is to measure the ERS signatures in the lab.

6.1 Electronic dispersion of tBLG

There are two methods to gain insight into the band structure of tBLG: the tight binding and the continuum model. The former is only valid under the premise of periodicity, needed to define the basis of Bloch functions, whereas the latter works just upon the definition of a moire supercell and therefore does not require commensurateness. In this section we present them using a coordinate system that divides equally the rotation between the two layers, θ, such that the rotated lattice vectors for each layer reads

$$\boldsymbol{a}^{\mathrm{t}}_{1,2} = \mathcal{R}_{+\frac{\theta}{2}}\boldsymbol{a}_{1,2}, \tag{6.1a}$$

$$\boldsymbol{a}^{\mathrm{b}}_{1,2} = \mathcal{R}_{-\frac{\theta}{2}}\boldsymbol{a}_{1,2}, \tag{6.1b}$$

where $\mathcal{R}_{\pm\frac{\theta}{2}}$ is the operator that performs a clockwise rotation of $\pm\frac{\theta}{2}$ and the superscript labels the top (t) and bottom (b) layers, which lie in the plane $z = h_{\mathrm{o}} \approx$

3.35Å and $z = 0$, respectively. The origin of the rotation is a common B atom in an AA stacked bilayer graphene, which is taken as the origin. Such rotation affects in the same manner the reciprocal space, in which the new reciprocal superlattice vectors for the top and bottom layers take the form

$$\boldsymbol{b}^{t}_{1,2} = \mathcal{R}_{+\frac{\theta}{2}}\boldsymbol{b}_{1,2}, \tag{6.2a}$$

$$\boldsymbol{b}^{b}_{1,2} = \mathcal{R}_{-\frac{\theta}{2}}\boldsymbol{b}_{1,2}. \tag{6.2b}$$

6.1.1 Tight binding model

As stated in the second chapter, the tight binding model provides reliable information about the low energy physics of graphene, and because of its simplicity, with the unit cell containing two atomic orbitals, this model is often a good starting point to approach other graphene-based materials. In this context, here we implement the tight-binding model for twisted bilayer graphene, which has been used to explore its electronic and optical properties [159, 160], in good agreement with experiments [161]. However, it comes with a geometrical constraint: arbitrary twist rotations do not necessarily reproduce a periodic (commensurate) structure, which is a requirement to construct Bloch states, by definition. Periodicity is accomplished only for a discrete but infinite set of twist angles θ satisfying the Diophantine equation [162, 163]

$$\cos\theta(m,r) = \frac{3m^2 + 3mr + r^2/2}{3m^2 + 3mr + r^2}, \qquad m, r \in \mathbb{Z}. \tag{6.3}$$

In Fig. 6.1.1, we visualise dependence of θ on r and m. For each value of r, the twist angle decreases monotonically with m. Fig. 6.1.2 shows the pictorial representation of the unit cell in two commensurate structures. Here we highlight the distinction between commensurate unit cell and moire supercell: while the former is defined as an periodic arrangement of atomic positions that repeats itself across the crystal lattice, the latter is defined by the beating of the two hexagonal lattices of graphene. There are always r^2 moire supercells within one commensurate unit

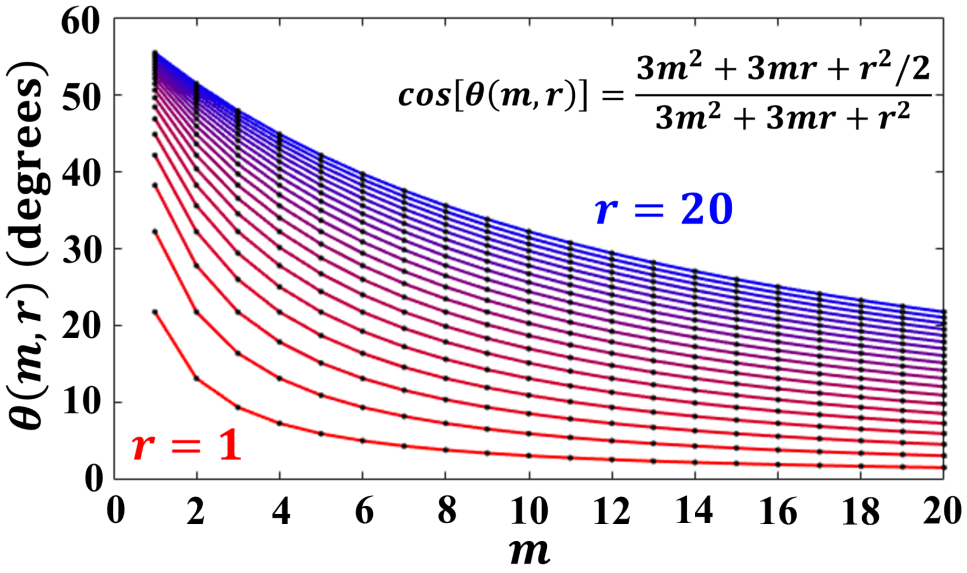

Figure 6.1.1: Representation of the solution for the Diophantine equation (black dots). To guide the eye, we join with different colours the family of solutions with the same r, from $r = 1$ (red) to $r = 20$ (blue).

cell, and the number of atoms within such cell is

$$N(m,r) = 4(3m^2 + 3mr + r^2), \tag{6.4}$$

which span an area

$$A(m,r) = (3m^2 + 3mr + r^2)\frac{\sqrt{3}}{2}a^2. \tag{6.5}$$

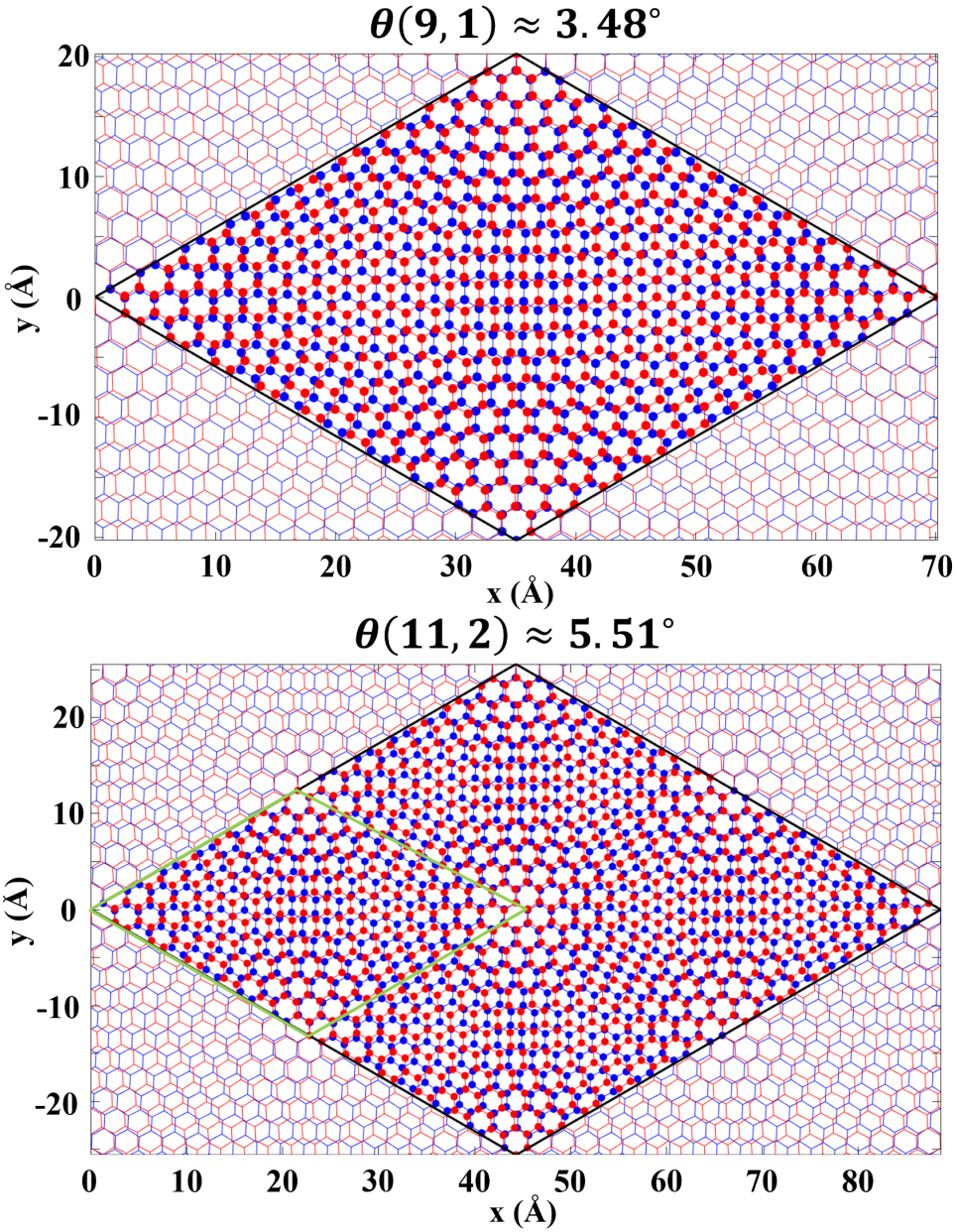

Figure 6.1.2: Pictorial representation of the unit cell of tBLG for two different commensurate angles. Notice that the Moire supercell, defined with the beating of the two hexagonal superlattices and highlighted in green lines, is the commensurate supercell only when $r = 1$.

We are going to choose the superlattice vectors,

$$\boldsymbol{R}_1 = R\left(\frac{\sqrt{3}}{2}, \frac{1}{2}\right), \tag{6.6a}$$

$$\boldsymbol{R}_2 = R\left(\frac{\sqrt{3}}{2}, -\frac{1}{2}\right), \tag{6.6b}$$

$$R = a\sqrt{9m^2 + 9mr + 3r^2}.$$

To apply the tight binding formalism, we now construct the $N(m, r)$-components Bloch basis of our Hamiltonian. In each component, we write the electronic amplitude corresponding to the p_z orbital centred at $\boldsymbol{d}$ within the supercell as

$$\left|\Phi_{\boldsymbol{k}}^{\boldsymbol{d}}(\boldsymbol{r})\right\rangle = \sum_{\boldsymbol{R}} e^{i(\boldsymbol{R}+\boldsymbol{d})\cdot\boldsymbol{k}} \left|\varphi_z(\boldsymbol{r} - \boldsymbol{d} - \boldsymbol{R})\right\rangle \tag{6.7}$$

Above, $\boldsymbol{R} = i\boldsymbol{R}_1 + j\boldsymbol{R}_2$ $(i, j \in \mathbb{Z})$. The wavenumber $\boldsymbol{k}$ is defined in the reciprocal space, which is now periodic along the wavevectors

$$\boldsymbol{G}_1 = \frac{2\pi}{R}\left(+\frac{1}{\sqrt{3}}, 1\right), \tag{6.8a}$$

$$\boldsymbol{G}_2 = \frac{2\pi}{R}\left(-\frac{1}{\sqrt{3}}, 1\right). \tag{6.8b}$$

Our hexagonal superlattice Brillouin zone (sBZ) is centred at the middle point of the Dirac points of the two layers in the $\boldsymbol{K}_+$ valley, $(\mathbf{K}_+^t + \mathbf{K}_+^b)/2$ [inset of Figs. 6.1.3 (a) and 6.1.4 (a)].

To model both the interlayer and intralayer coupling, we employ the Slater-Koster parametrisation [164], which approximates the tunnelling between any two p_z atomic orbitals in the crystal, centred at $\boldsymbol{D}_1$ and $\boldsymbol{D}_2$, as a function of their distance, D, and their relative position $\boldsymbol{D} = \boldsymbol{D}_2 - \boldsymbol{D}_1$, as follows

$$T(\boldsymbol{D}) \equiv \left\langle \varphi_z(\mathbf{r} - \boldsymbol{D}_2)\right| \mathcal{H} \left|\varphi_z(\mathbf{r} - \boldsymbol{D}_1)\right\rangle \approx \tag{6.9}$$
$$\gamma_0 \exp\left(-\frac{D - a_0}{\delta_0}\right)\left[1 - \left(\frac{\boldsymbol{D}\cdot\boldsymbol{e}_z}{D}\right)^2\right] + \gamma_1 \exp\left(-\frac{D - h_0}{\delta_0}\right)\left(\frac{\boldsymbol{D}\cdot\boldsymbol{e}_z}{D}\right)^2.$$

In the equation above, the parameter $\delta_0 \approx 0.26$Å captures the exponentially decaying strength of the coupling. Following previous works [159, 160], we fix that value so that the nearest neighbour coupling, γ_0, is one order of magnitude greater than the next-nearest neighbour coupling, γ_n. Notice that, for two neighbouring atoms lying in the same plane ($D_z = 0, D = a_0$), we recover the usual intralayer coupling for graphene γ_0, whilst for two orbitals lying on top of each other ($D_x = D_y = 0, D_z = h_0$), we have the interlayer coupling constant for bilayer graphene, γ_1.

We compute numerically the eigenvalues of the resulting $N(m,r) \times N(m,r)$ Hamiltonian in a square grid in reciprocal space of 500×500 points around the $\boldsymbol{K}_+$ point. In Figs. 6.1.3 and 6.1.4, we present the band structure along with the density of states of tBLG for commensurate structures with angles $\theta(4,1) \approx 7.3^\circ$ and $\theta(6,1) \approx 5.0^\circ$, respectively. For these structures, the band structure inherits the low-energy dispersion of graphene around $\boldsymbol{K}_+^{\mathrm{t}}$ and $\boldsymbol{K}_+^{\mathrm{b}}$ points, with a reduced Fermi velocity that increases the density of states around the CNP. At the centre of the hexagonal sBZ the Dirac states from both layers hybridise resulting in saddle points on the two bands above and two bands below the CNP, which manifest themselves in the electronic density of states in the form of vHSs. The formation of other vHSs at the M point of graphene dispersion also becomes apparent in the density of states, where the band structures of both layers anti-cross yielding a set of vHSs at $\sim \pm 3$ eV. Another important feature worth mentioning in the low-energy dispersion is the nearly two-fold degeneracy of bands around the CNP, with the blue and red bands being almost a (carbon) copy each other. With the benefit of the hindsight, we know that half of these states are folded from the other valley at $\boldsymbol{K}_-$. Their degeneracy reminds us that both valleys remain effectively uncoupled in tBLG for small angles.

Experiments on tBLG using optical absorption and ARPES [165–167] suggest that the underlying physics of this model is successfully captured by the tight binding model. Furthermore, for a given angle θ_0 that do not reproduce a commen-

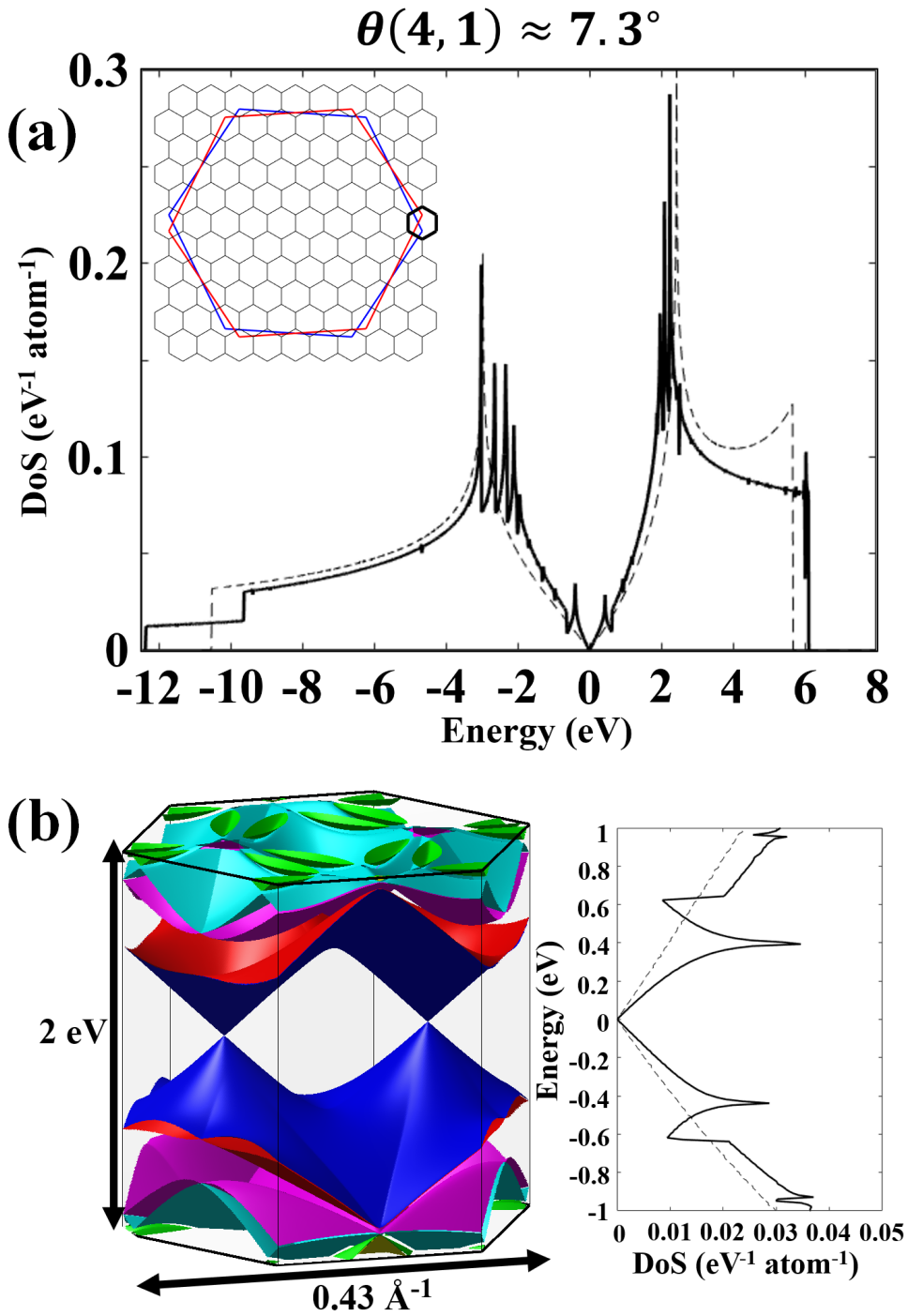

Figure 6.1.3: (a) DoS for tBLG using tight binding model with $\theta(4,1) \approx 7.3^\circ$ (solid lines) and for graphene (dashed lines). (b) Band structure in the first mini Brillouin zone around the $\boldsymbol{K}_+$ point, and DoS within an energy window of 2 eV.

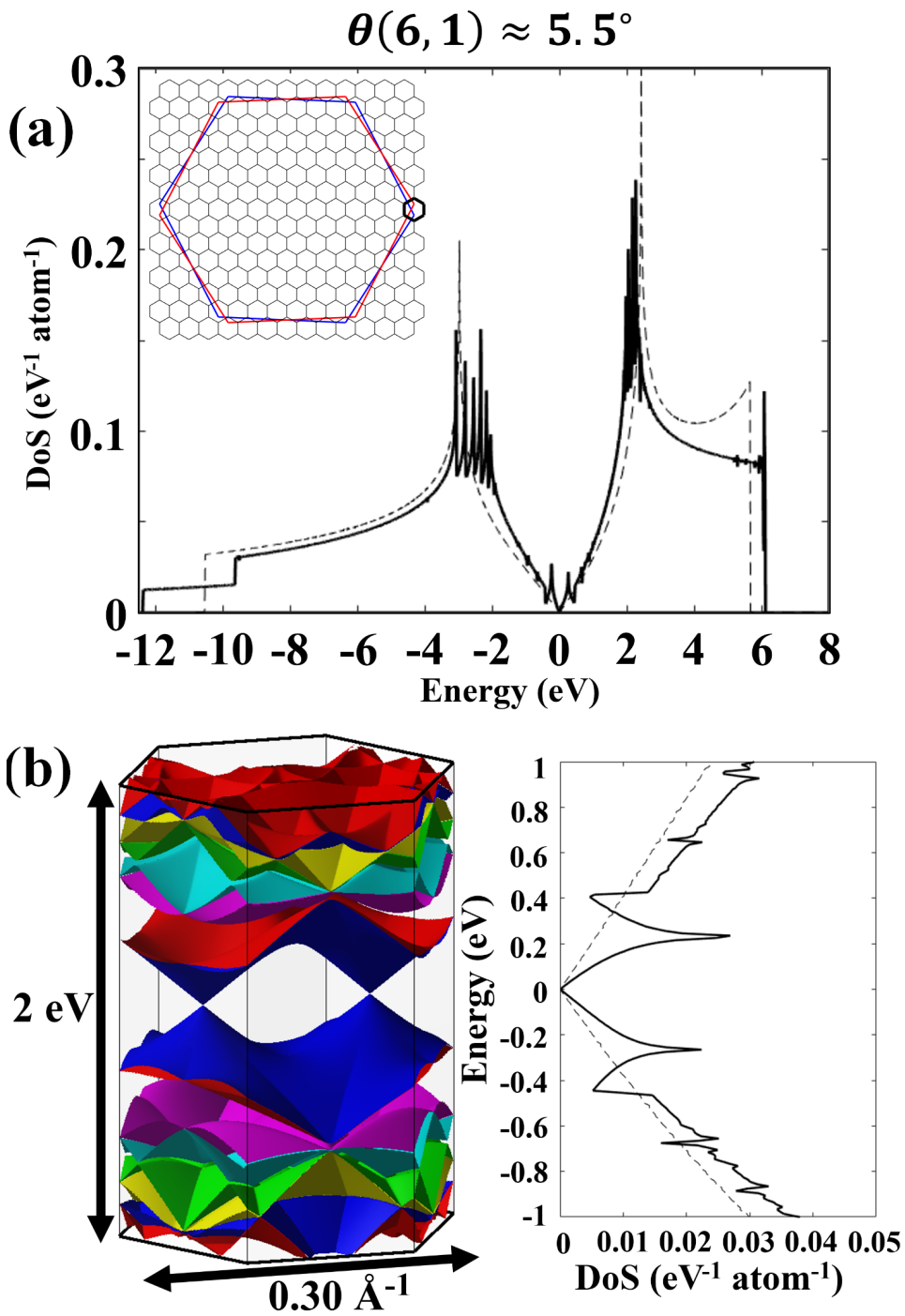

Figure 6.1.4: (a) DoS for tBLG using tight binding model with $\theta(6,1) \approx 5.5^\circ$ (solid lines) and for graphene (dashed lines). (b) Band structure in the first mini Brillouin zone around the $\boldsymbol{K}_+$ point, and DoS within an energy window of 2 eV.

surate structure, we can find a pair (m, r) in Eq. (6.3) such that the difference $|\theta(m, r) - \theta_0|$ is arbitrarily small. However, we encounter an important limiting factor using this method for small angles. The number of atoms, and therefore the dimension of the Hamiltonian, scales as

$$N(m, 1) \approx \frac{4}{\theta^2(m, 1)}, \tag{6.10}$$

where we used $\cos\theta \approx 1 - \frac{\theta^2}{2}$ in Eq. (6.3) (θ in radians). Following the expression above, supercells for commensurate structures with twist angles $\theta_{\mathrm{MA}} \approx 1^\circ$ contain more than 10^4 atoms, which makes it impractical to simulate ERS spectra. Furthermore, tight binding is a rather brute force approach that may limit our understanding of the problem. For example, unfolding bands to the Brillouin zone of graphene is not straightforward, making it hard to interpret the hybridisation of Dirac states. Additionally, we lose the concept of valleys as a good quantum number in the folded scheme. For this reason, the second part of this section is devoted to describe an alternative model that can capture the low energy physics of small-angle tBLG, which is based on the picture for graphene we studied in chapter 2 and comes with the advantage of managing Hamiltonians of dimension $\sim 100 \times 100$.

6.1.2 The continuum model

In the tight binding, the expression in Eq. (6.9) treats jointly both intralayer and interlayer coupling by modelling the tunnelling that couples any two p_z orbitals in the crystal. The continuum model takes a different approach. To describe the electronic transport within each layer, it keeps the Dirac description for monolayer graphene studied in chapter 2, with Dirac states centred at $\boldsymbol{K}_\pm^{\mathrm{t}} = \mathcal{R}_{+\frac{\theta}{2}}\boldsymbol{K}_\pm$ and $\boldsymbol{K}_\pm$ b $= \mathcal{R}_{-\frac{\theta}{2}}\boldsymbol{K}_\pm$ for the top and bottom layer, respectively. We are going to assume that valleys are effectively uncoupled at small angles and focus our discussion on the $\boldsymbol{K}_+$ valley, so as to simplify our notation. We keep the 4×4 Bloch

basis

$$\left|\Phi^{t,b}_{A,B,\boldsymbol{p}}(\boldsymbol{r})\right\rangle = \sum_{i,j} e^{\frac{i}{\hbar}(i\boldsymbol{a}_1^{t,b}+j\boldsymbol{a}_2^{t,b})\cdot(\hbar\boldsymbol{K}_+^{t,b}+\boldsymbol{p})} \left|\varphi_z(\mathbf{r}-\Delta^{t,b}_{A,B})\right\rangle . \tag{6.11}$$

Above, the symbol $\Delta^{t,b}_{A,B}$ gives the position of the atom belonging to the A, B sublattice within the unit cell of the top (t) and bottom (b) layers. The main difference between these two models lies in the description of the inter-layer coupling: instead of modelling the tunnelling between p_z orbitals as in Eq. (6.9), it models the tunnelling between Bloch states $\left\langle \Phi^{t}_{A,B,\boldsymbol{p}'}(\boldsymbol{r})\right| \mathcal{H} \left|\Phi^{b}_{A,B,\boldsymbol{p}}(\boldsymbol{r})\right\rangle$, and takes the beating of the two hexagonal lattices as truly periodic. This allows us to define the moire lattice vectors

$$\boldsymbol{R}_1^m = \frac{a}{2\sin\theta}\left(\sqrt{3}, 1\right), \tag{6.12a}$$

$$\boldsymbol{R}_2^m = \frac{a}{2\sin\theta}\left(\sqrt{3}, -1\right), \tag{6.12b}$$

together with the moire reciprocal vectors in reciprocal space

$$\boldsymbol{G}_1^m = \frac{\sqrt{3}}{2}\Delta K\left(1, \sqrt{3}\right), \tag{6.13a}$$

$$\boldsymbol{G}_2^m = \frac{\sqrt{3}}{2}\Delta K\left(-1, \sqrt{3}\right), \tag{6.13b}$$

with $\Delta K \equiv \left|\boldsymbol{K}_+^t - \boldsymbol{K}_+^b\right|$ being the wavenumber mismatch. To compute the tunnelling between two Bloch states belonging to different layers, we need to re-express $T_\perp(\boldsymbol{r})$ in the reciprocal space [150],

$$T_\perp(\boldsymbol{r}) = \sum_{\boldsymbol{G}^m} t_\perp\left(\boldsymbol{G}^m\right) T_{\boldsymbol{G}^m} e^{i\boldsymbol{G}^m\boldsymbol{r}}, \tag{6.14}$$

where $T_{\boldsymbol{G}^m}$ is a 2×2 matrix accounts for the spatial phase between the different stacking orders. Therefore, the continuum model essentially rewrites our problem: instead of computing the tunnelling between each p_z orbital in the lattice, it requires the evaluation the $t_\perp(\boldsymbol{G}^m)$, with $\boldsymbol{G}^m = i'\boldsymbol{G}_1^m + j'\boldsymbol{G}_2^m$ a moire reciprocal

superlattice vector. This may not seem like an advantage until one notices that, in the expansion of Eq. (6.14), the coefficients $t_\perp(0) = t_\perp(\boldsymbol{G}_1) = t_\perp(\boldsymbol{G}_2) \approx 110$ meV are at least two orders of magnitude larger than any other coefficient, and its value is equal to the Fourier transform of a p_z orbital evaluated at $\boldsymbol{K}_+$ [153]. This is the actual advantage of the continuum model, which allows us to truncate Eq. (6.14) as

$$T_\perp(\boldsymbol{r}) = t_\perp \left[\begin{pmatrix} 1 & 1 \\ 1 & 1 \end{pmatrix} + \begin{pmatrix} e^{i\frac{2\pi}{3}} & 1 \\ e^{i\frac{4\pi}{3}} & e^{i\frac{2\pi}{3}} \end{pmatrix} e^{i\boldsymbol{G}_1^m \cdot \boldsymbol{r}} + \begin{pmatrix} e^{i\frac{4\pi}{3}} & 1 \\ e^{i\frac{2\pi}{3}} & e^{i\frac{4\pi}{3}} \end{pmatrix} e^{i\boldsymbol{G}_2^m \cdot \boldsymbol{r}} \right]. \quad (6.15)$$

To compare the continuum and the tight-biding models, we present in Fig. 6.1.5 the inter-layer coupling strength of a p_z orbital belonging to an atom in the A sub-lattice of the top layer to another p_z orbital belonging to an atom in the A sub-lattice of the bottom layer, which corresponds to the $(1,1)$ element of the matrix in Eq. (6.14). The continuum models capture the same monotony as the tight binding of the coupling strength, reaching maxima at the AA-stacked corners of the superlattice and minima at the AB and BA stacked regions. Some minor discrepancies appear around the AB and BA stacked regions, where the tight binding gives values of $\sim$ 0.2 eV, in agreement with the corresponding γ_4 in the SWMcCLure parametrization for Bernal bilayer graphene, while the continuum model vanishes exactly at these points.

The complete Hamiltonian around the $\boldsymbol{K}_+$ valley is

$$\mathcal{H}(\boldsymbol{r}, \boldsymbol{p}) = \begin{pmatrix} \mathcal{H}_L(\mathbf{p} - \frac{\hbar \Delta \mathbf{K}_+}{2}, \frac{\theta}{2}) & T(\mathbf{r}) \\ T^\dagger(\mathbf{r}) & \mathcal{H}_L(\mathbf{p} + \frac{\hbar \Delta \mathbf{K}_+}{2}, -\frac{\theta}{2}) \end{pmatrix}, \quad (6.16)$$

where we introduce a second argument in the Hamiltonian of monolayer graphene to account for the rotation of Dirac states,

$$\mathcal{H}_L(\boldsymbol{p}, \varphi) = v \begin{pmatrix} 0 & (p_x - ip_y)e^{i\varphi} \\ (p_x - ip_y)e^{-i\varphi} & 0 \end{pmatrix}. \quad (6.17)$$

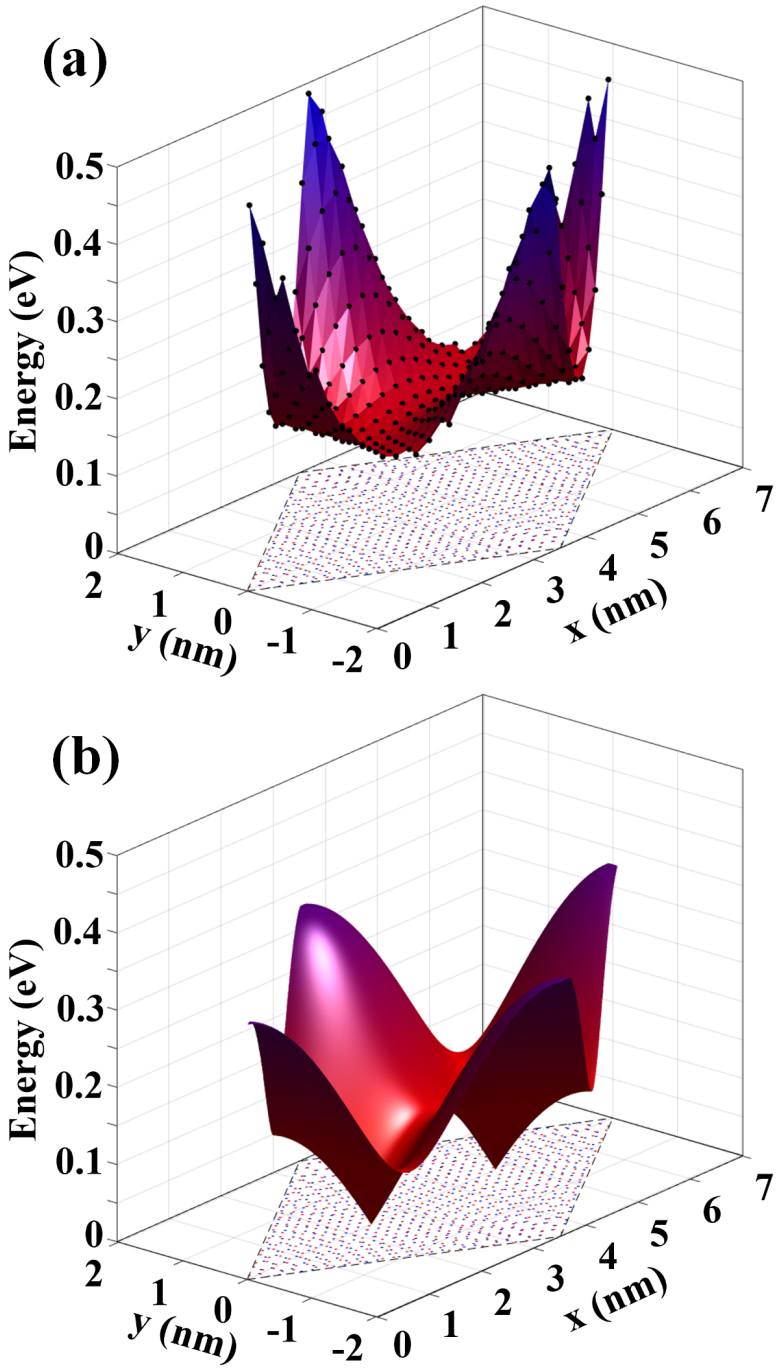

Figure 6.1.5: Pictorial representation of the absolute value of the first component in the matrix $T(\boldsymbol{r})$, (a) with the tight binding model, using in Eq. (6.9) to plot the black dots and interpolating to generate the surface, and (b) with the continuum model using Eq. (6.15)

The evaluation of the off-diagonal elements gives

$$\left\langle \Phi^{\mathrm{t}}_{A,B}(\boldsymbol{p}',\boldsymbol{r})\right| T_{\perp}(\boldsymbol{r}) \left|\Phi^{\mathrm{b}}_{A,B}(\boldsymbol{p},\boldsymbol{r})\right\rangle = t_{\perp}\left[\begin{pmatrix}1 & 1\\ 1 & 1\end{pmatrix}\delta\left(\frac{\boldsymbol{p}'-\boldsymbol{p}}{\hbar}\right)+\right. \tag{6.18}$$
$$+\begin{pmatrix}e^{i\frac{2\pi}{3}} & 1\\ e^{i\frac{4\pi}{3}} & e^{i\frac{2\pi}{3}}\end{pmatrix}\delta\left(\frac{\boldsymbol{p}'-\boldsymbol{p}-\hbar\boldsymbol{G}^m_1}{\hbar}\right)+$$
$$\left.+\begin{pmatrix}e^{i\frac{4\pi}{3}} & 1\\ e^{i\frac{2\pi}{3}} & e^{i\frac{4\pi}{3}}\end{pmatrix}\delta\left(\frac{\boldsymbol{p}'-\boldsymbol{p}-\hbar\boldsymbol{G}^m_2}{\hbar}\right)\right].$$

The Dirac deltas in the interlayer potential above, which originate from integration in space, couple directly one electronic state in the bottom layer with momentum $\boldsymbol{p}$ to three electronic states in the top layer with momenta $\boldsymbol{p}'=\boldsymbol{p}$, $\boldsymbol{p}'=\boldsymbol{p}+\hbar\boldsymbol{G}^m_1$ and $\boldsymbol{p}'=\boldsymbol{p}+\hbar\boldsymbol{G}^m_2$. Each of these three states, in turn, are coupled to other three states in the bottom layer, with momenta $\boldsymbol{p}''=\boldsymbol{p}'$, $\boldsymbol{p}''=\boldsymbol{p}'-\hbar\boldsymbol{G}^m_1$ and $\boldsymbol{p}''=\boldsymbol{p}'-\hbar\boldsymbol{G}^m_2$, which are indirectly coupled to the first electron in the bottom layer with momentum $\boldsymbol{p}$. This makes the diagonalisation of the Hamiltonian in Eq. (6.16) less straightforward, as we first incorporate to our basis in Eq. (6.11) an infinite number of Bloch states centred at every $\boldsymbol{K}^{\mathrm{t,b}}_{+}+\boldsymbol{G}^m$ point to compute the Dirac deltas in Eq. (6.18),

$$\left|\Phi^{\mathrm{t,b}}_{A,B}\left(\boldsymbol{p}-\hbar\boldsymbol{G}^m,\boldsymbol{r}\right)\right\rangle = \sum_{\boldsymbol{G}^m} e^{\frac{i}{\hbar}(\mathrm{i}\boldsymbol{a}^{\mathrm{t,b}}_1+\mathrm{j}\boldsymbol{a}^{\mathrm{t,b}}_2)\cdot\left(\boldsymbol{p}-\hbar\boldsymbol{K}^{\mathrm{t,b}}_{+}-\hbar\boldsymbol{G}^m\right)}\left|\varphi_z(\mathbf{r}-\Delta^{\mathrm{t,b}}_{A,B})\right\rangle. \tag{6.19}$$

However, we can model the mini bands within an energy window ΔE in the first superlattice Brillouin zone by constructing a basis with a large enough number of Bloch states centred around $\boldsymbol{K}^{\mathrm{t,b}}_{+}$. In particular, our model considers the coupling of one state inside the first superlattice Brillouin with momentum $\boldsymbol{p}$ to any of the 37 states in the other layer with momentum $\boldsymbol{p}'=\boldsymbol{p}+\hbar\boldsymbol{G}^m$, satisfying $|\hbar\boldsymbol{G}^m|\leq 6\Delta K$ (Fig. 6.1.6). Such basis is large enough to describe the band structure up to ± 0.5 eV for angles as small as $\theta = 2\arcsin(\frac{\Delta E/v\hbar}{12K})\sim 0.6^{\circ}$.

The continuum model described here may look like a heuristic approach to

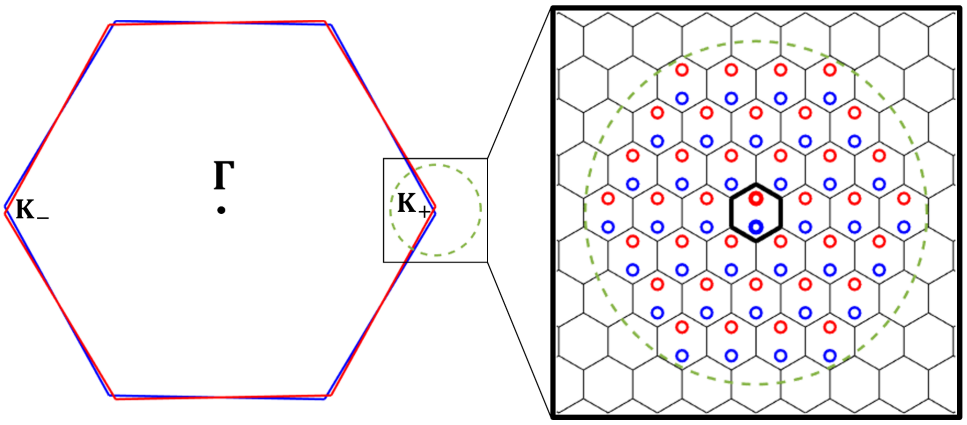

Figure 6.1.6: Pictorial representation of the first Brillouin zone of the top (red) and bottom (blue) graphene layers, rotated $\theta = +1^\circ$ and $\theta = -1^\circ$, respectively. Around the $\boldsymbol{K}_+$ point (left), with thicker lines, we highlight the first mini Brillouin zone, together with the position of the Dirac cones for the top and bottom layers. Outside the first mBZ we plot a circle of radius $6\Delta K$, enclosing the 37 smallest $\boldsymbol{G}^m = i'\boldsymbol{G}^m + j'\boldsymbol{G}^m$ vectors, each of them representing the centre of the 4-component Bloch basis in Eq. (6.19).

the problem, in contrast to the thorough tight binding model. Therefore, we first start by comparing the resulting band structure using both models in Fig. 6.1.7, for a twist angle $\theta(9,1) \approx 3.481^\circ$. Despite the aforementioned differences in $T(\boldsymbol{r})$, these models reproduce the same physics: around the $\boldsymbol{K}^{\mathrm{t}}_+$ and $\boldsymbol{K}^{\mathrm{b}}_+$ points the dispersion resembles that of monolayer graphene with a reduced Fermi velocity, whilst around the centre of the sBZ the hybridization of Dirac states produces band anti-crossing, giving rise to saddle points and sharp peaks in the density of states. This interpretation holds for smaller twist angles $\sim 2^\circ$, with the positions of the saddle points drifting towards the CNP and the Fermi velocity monotonically decreasing (6.1.8). For $\theta \lesssim 1.5^\circ$, however, the band structure exhibit features that cannot be explained by a naive picture of weakly coupled Dirac states (Fig. 6.1.9a). At the so-called magic angle, which we obtain at $\theta_{\mathrm{MA}} = 1.11^\circ$, the renormalised Fermi velocity goes to zero (Fig. 6.1.8), and the first valence and conduction minibands become (nearly) flat (Fig. 6.1.9b). This is one of the key pieces to understand the emergence of strongly correlated phenomena in tBLG at

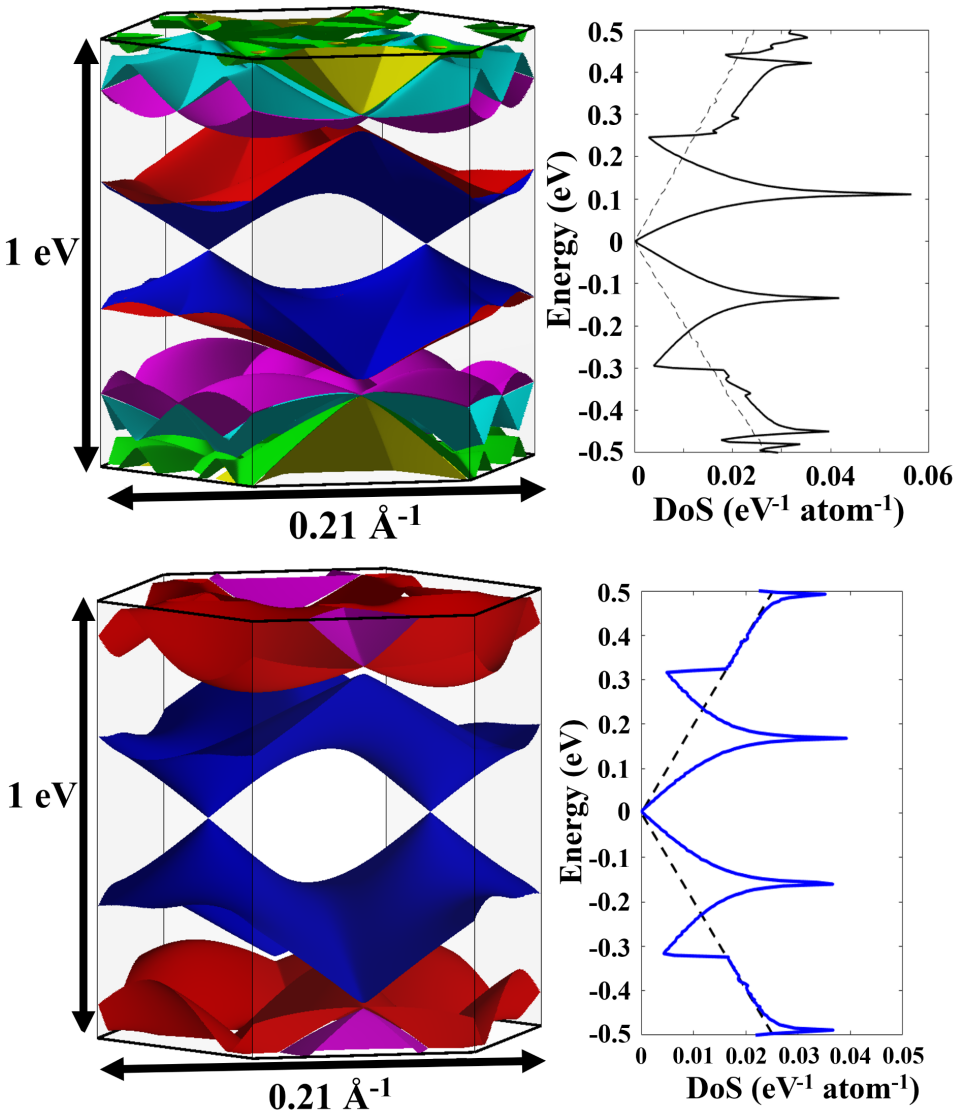

Figure 6.1.7: Band structure and density of states within an energy window of 1 eV, using the tight binding model (top) and the continuum model (bottom). Both model describe qualitatively the same physics, agreeing in the position of vHSs and the shape of the bands. Notice that the duplication of the first bands in the tight binding model (specially remarkable for the blue and red bands) is a consequence of the valley degeneracy.

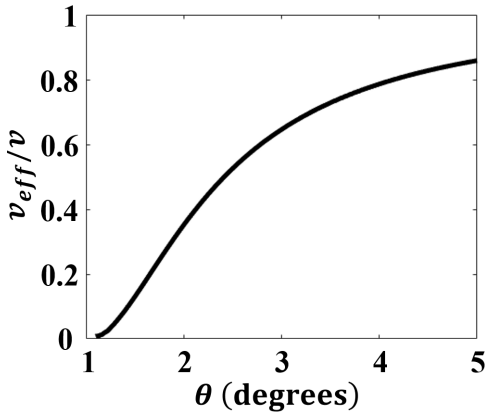

Figure 6.1.8: Ratio between the effective Fermi velocity in tBLG and the Fermi velocity for monolayer graphene, calculated using the continuum model. Below θ_{MA}, the first valence and conduction bands do not feature conical dispersions.

this angle, and is also an indication of electronic states localised in real space, in particular, in the AA stacked regions [168, 169]. At $\theta = 0.9°$, the first minibands warp again (Fig. 6.1.9c), while the vHSs associated to higher bands approach to the CNP. Below such angle, the DoS of tBLG (not shown) resembles that of AB bilayer graphene, due to the increasing areas of AB stacking.

We finish this section by acknowledging the limitations of the continuum model we employ. Firstly, we only include the first-order coefficient in the Fourier expansion to build the interlayer coupling in reciprocal space. Secondly, and arguably more important, this model does not account for lattice relaxation effects. Many articles have highlighted its importance at smaller angles, where the AA-stacked areas significantly reduce and the AB and BA stacked regions enlarge and become separated by thinner domain walls. In fact, recent works suggest that the actual value of the magic angle is lower than 1.11° because of relaxation effects [155, 170]. Our minimal model has the advantage of relying on two parameters, $\gamma_0 \approx 2.7$ eV and $t_\perp \approx 0.11$ eV, but it can provide qualitative trends rather than exact numbers.

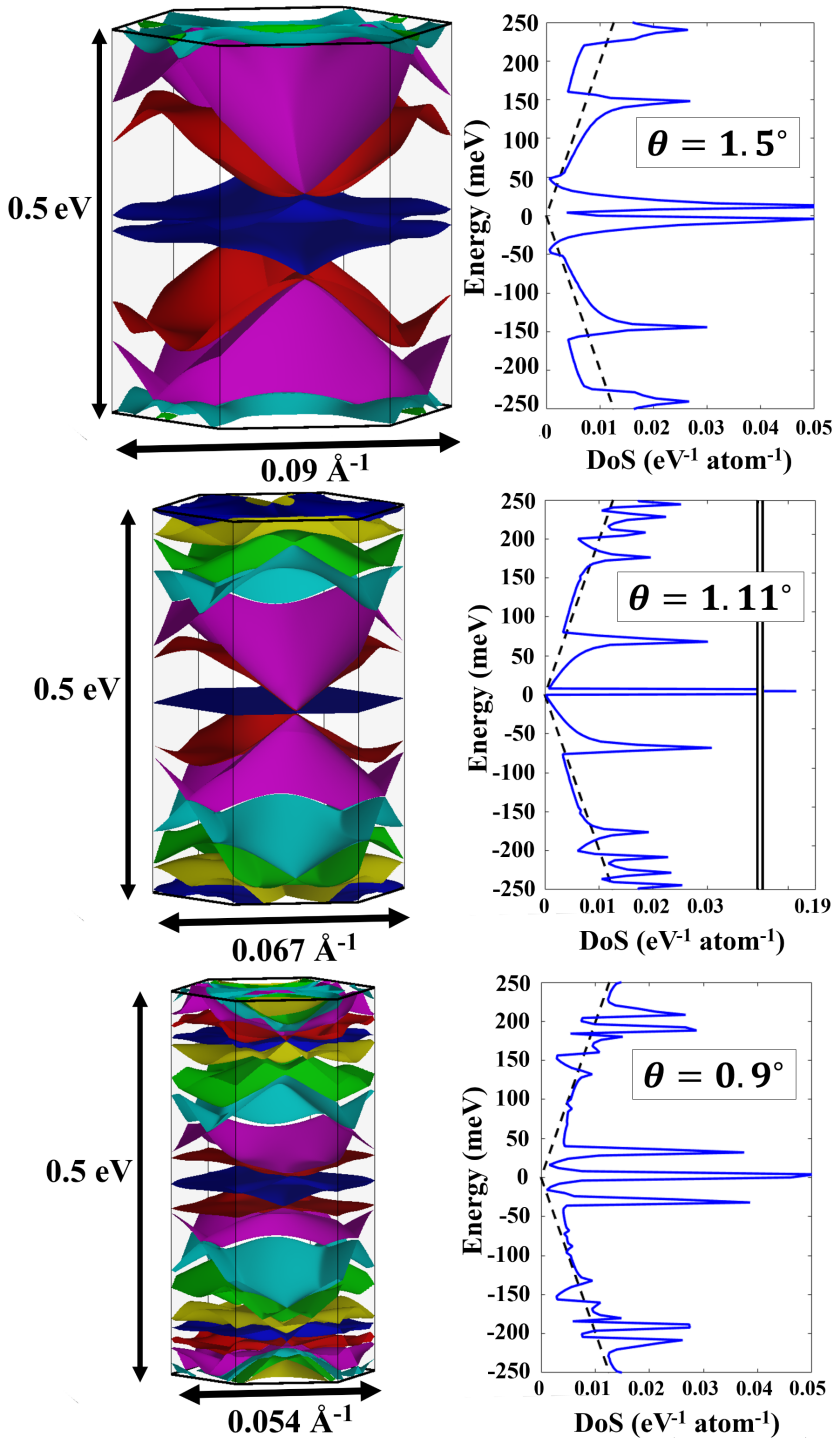

Figure 6.1.9: Band structure and density of states of tBLG for three angles above, at and below $\theta_{\mathrm{MA}} = 1.11^{\circ}$.

6.2 Theoretical description of ERS in tBLG

Here we compute the electronic contributions to the Raman spectrum of tBLG using the continuum model. The aim is to prove that this spectroscopic technique has a potential to characterise this material and extract direct information about its band structure, in particular, the position of vHSs in the density of states. The description of the light-matter interaction is analogous to that of previous chapters: we assume the incident beam of light is normal to the graphene layers and construct the canonical momentum $\boldsymbol{P} \to \boldsymbol{p} - e\boldsymbol{A}$, from which we only take the linear contribution in the photon field. The resulting interaction term,

$$\mathcal{V}(\boldsymbol{r}, t) = -e\boldsymbol{I}_{37} \otimes \begin{pmatrix} \mathcal{H}_{\mathrm{L}}(\boldsymbol{A}, \frac{\theta}{2}) & 0 \\ 0 & \mathcal{H}_{\mathrm{L}}(\boldsymbol{A}, -\frac{\theta}{2}) \end{pmatrix}, \tag{6.20}$$

is treated as a time-dependent perturbation, which contributes to the Raman amplitude in a two-steps process. Proceeding as in chapter 4 with graphite, we calculate the Raman amplitude for a process that leaves a hole in the n_{h}-th miniband below the CNP and one electron in the n_{e}-th miniband above the CNP,

$$\begin{aligned} \langle s_{\mathrm{f}}| \mathcal{R}^{\mathrm{L}}_{\mathrm{em}} |s_{\mathrm{i}}\rangle =& \frac{e^2\hbar^2}{\varepsilon_0\Omega^2} \frac{\sin\left[(E^+_{\mathrm{e}} - E^-_{\mathrm{h}} - \omega)\frac{T}{2\hbar}\right]}{(E^+_{\mathrm{e}} - E^-_{\mathrm{h}} - \omega)/2} \\ &\times \langle +, \mathrm{e}| I_{37} \otimes \left[\begin{pmatrix} \mathcal{H}_{\mathrm{L}}(\boldsymbol{l}, \frac{\theta}{2}) & 0 \\ 0 & \mathcal{H}_{\mathrm{L}}(\boldsymbol{l}, -\frac{\theta}{2}) \end{pmatrix} \begin{pmatrix} \mathcal{H}_{\mathrm{L}}(\tilde{\boldsymbol{l}}^*, \frac{\theta}{2}) & 0 \\ 0 & \mathcal{H}_{\mathrm{L}}(\tilde{\boldsymbol{l}}^*, -\frac{\theta}{2}) \end{pmatrix} \right. \\ &\left. - \begin{pmatrix} \mathcal{H}_{\mathrm{L}}(\tilde{\boldsymbol{l}}^*, \frac{\theta}{2}) & 0 \\ 0 & \mathcal{H}_{\mathrm{L}}(\tilde{\boldsymbol{l}}^*, -\frac{\theta}{2}) \end{pmatrix} \begin{pmatrix} \mathcal{H}_{\mathrm{L}}(\boldsymbol{l}, \frac{\theta}{2}) & 0 \\ 0 & \mathcal{H}_{\mathrm{L}}(\boldsymbol{l}, -\frac{\theta}{2}) \end{pmatrix} \right] |-, \mathrm{h}\rangle \\ =& \frac{e^2\hbar^2 v^2}{\varepsilon_0\Omega^2} \frac{\sin\left[(E^+_{\mathrm{e}} - E^-_{\mathrm{h}} - \omega)\frac{T}{2\hbar}\right]}{(E^+_{\mathrm{e}} - E^-_{\mathrm{h}} - \omega)/2} (\boldsymbol{l} \times \tilde{\boldsymbol{l}}^*)_z \langle +, \mathrm{e}| I_{74} \otimes \sigma_z |-, \mathrm{h}\rangle . \end{aligned} \tag{6.21}$$

We compute numerically the bracket in the equation above, which allows us to compute the spectral density after integrating over all possible directions of scattered light.

In Fig. 6.2.1a we present the spectral density for $\theta = 1.5^\circ$. The main contri-

bution to the electronic Raman signal originates from electronic transitions that leave a hole in the first and second valence band and one electron in the first and second conduction band, respectively. They generate a clear spectroscopic signature, two peaks at $\sim$ 30 meV and $\sim$ 280 meV, which approximately give the distance between the vHSs in the density of states. At the magic angle, when the first bands below and above the CNP become flat, they give rise to a small peak at zero energy, while the second peak gradually approaches the origin. For twist angles below $\theta = 1.11^{\circ}$, ERS keeps track of changes in the band structure: the warping of the first band makes the features associated to it appear at slightly higher energies and the flattening of the second band can be estimated from the width of the red peak. Interestingly, higher order bands do not lead to sharp peaks, but instead they contribute to an almost constant background, a consequence of the enlargement of AB and BA-stacked regions in tBLG.

In Fig. 6.2.2 we present a summary of the Raman spectra for angles ranging from 0.8 to 2 degrees. In this range of energies, we predict two peaks, emerging from the first two bands above and below the neutrality point. There is a strong connection between these two and the density of states: their position is approximately the distance between vHSs, while their shape estimates the band width. It is worth mentioning that, for smaller angles, the size of minibands reduces, which reduces the efficiency of these peaks.

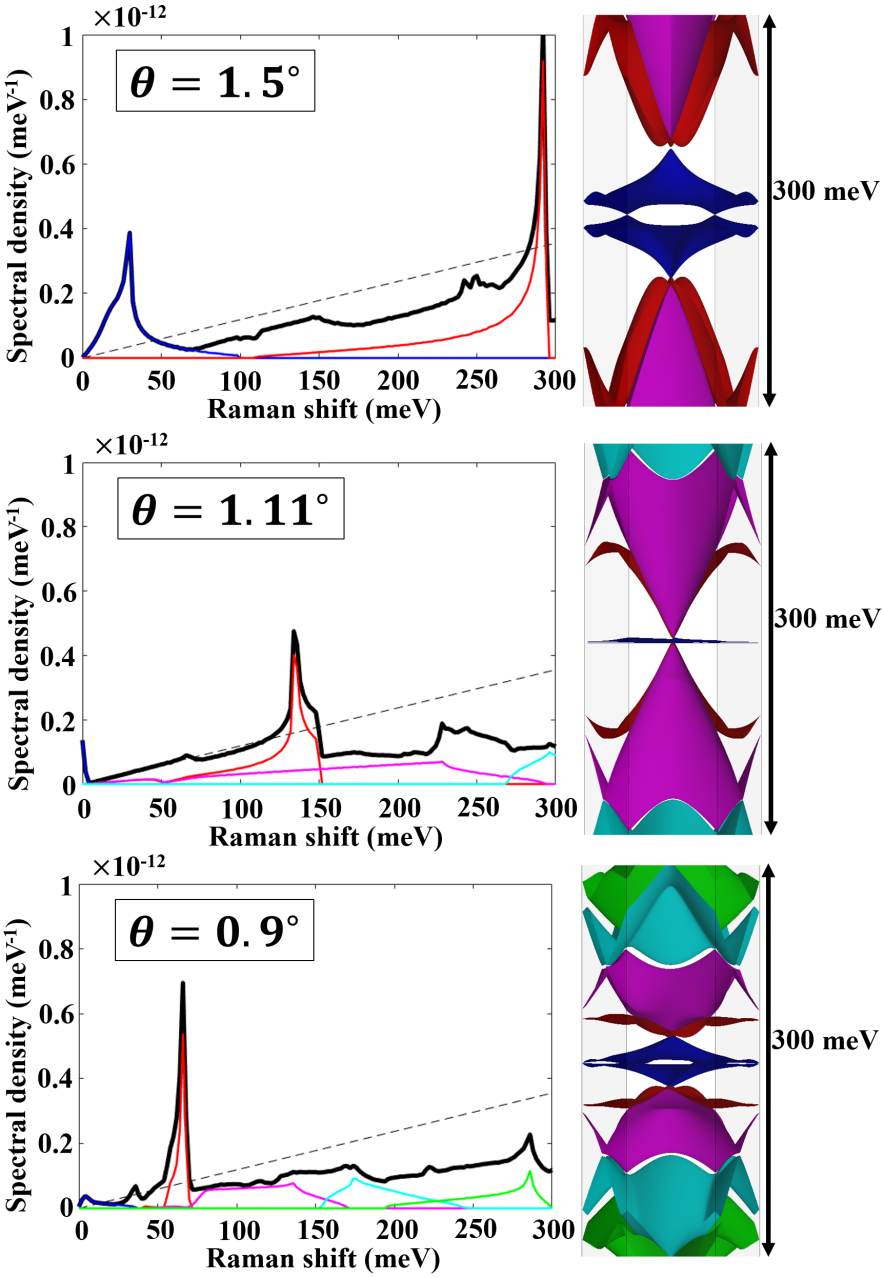

Figure 6.2.1: ERS Spectral density of tBLG for three angles above, at and below $\theta_{\mathrm{MA}} = 1.11^{\circ}$ (black). The blue, red, magenta, cyan and green lines represent Raman features that leave one hole and one electron in the first, second, third, fourth and fifth valence and conduction bands, respectively. To emphasize the link between the position of the Raman peaks and the distance between saddle points of the n-th valence and n-th conduction bands, we show the band structure on the right side.

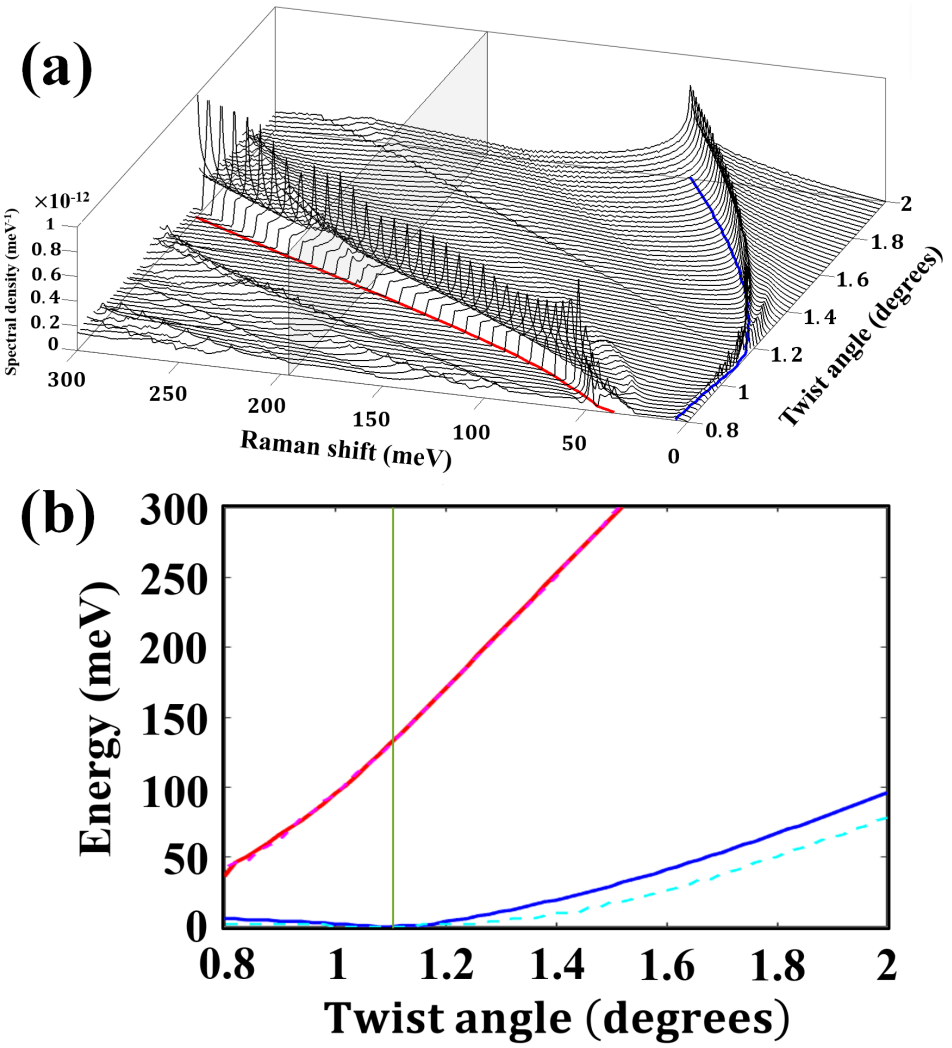

Figure 6.2.2: (a) Spectral density of cross-linear polarisation for tBLG at twist angles ranging from 0.8° to 2°. In the plane $g(\omega) = 0$ we plot the position of the first (blue) peak and second (red) peak in the Raman spectra. They are also plotted in (b), alongside with the distances between vHSs of the first (dashed cian curve) and second (dashed magenta curve) bands below and above the CNP.

6.3 Experimental evidence for ERS in tBLG

Researchers have obtained Raman spectra of tBLG since its fabrication became possible, and they found distinctive features that change with the twist angle. For example, in [171, 172], the authors observed a resonant enhancement (by a factor of $\sim$ 20) of the G peak when the laser frequency matches the distance between vHSs, which typically occurs at $\theta \sim 10^\circ$ (shown here in Fig.6.3.1b). In [173], they report the emergence of breathing modes, phonon-induced features that become Raman active at certain twist angles [Fig. 6.3.1 (a)]. In all these cases, however, the focus was on samples with angles $> 5^\circ$, as samples below $\sim 2^\circ$ are thermally unstable, and it is often necessary to encapsulate them in hexagonal boron nitride [174]. For the few samples with twist angles close to 1.1°, no ERS signals were reported.

Therefore, to the best of our knowledge, the features presented in this chapter stand as predictions, and to give arguments for the feasibility of their experimental observation, we conclude this chapter by computing numerically the quantum efficiency. As in the two previous chapters, we integrate the area underneath the predicted features in Figs. 6.2.1. For both the read and blue peaks, this gives the yield $I \sim 10^{-12}$ above the magic angle and $I \sim 10^{-13}$ below, which is about the same quantum efficiency as that of the experimentally confirmed ERS features in graphite. Accordingly, one may wonder why experimentalists have not found evidences for this type of scattering in tBLG yet. One possible reason is the difficulty in preparing large size samples with a constant twist angle over the laser spot, because the sensitivity of the ERS signal, which is a blessing when characterising this material, turns into a curse when the twist angles vary even by a tenth of a degree. This factor is likely to broaden and weaken the signal described here. Another reason that makes this type of scattering difficult to observe is the presence of stronger phonon mediated Raman signals, which may overshadow ERS. Lastly, a third possibility is that experimentalists may have simply overlooked this type of scattering or misinterpret it as a phonon mode. Its experimental observation will be a step forward towards the characterisation of tBLG, and will provide us with a deeper

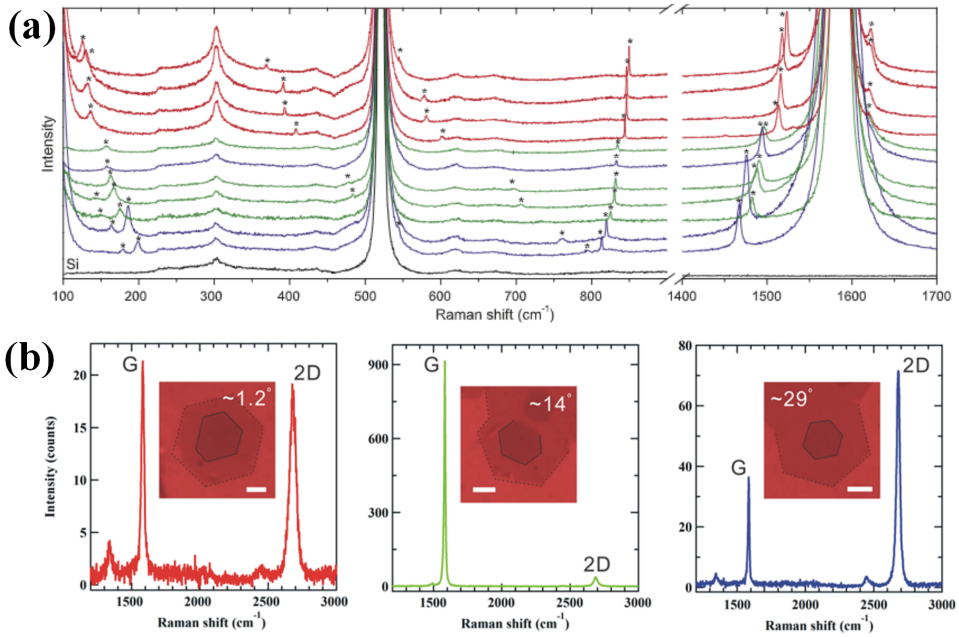

Figure 6.3.1: (a) Source: [173] Fig. 5. Raman spectra of tBLG with different rotational angles. Red, green and blue lines correspond to different energies of the incoming beam, $\Omega = 1.96$ eV, $\Omega = 2.41$ eV and $\Omega = 2.54$ eV, respectively. The black line corresponds to the silicon substrate reference signal. The source does not provide information about the twist angles. (b) Source: [172] Fig. 1b. Raman spectra of tBLG for twist different twist angles below, near and above the G-peak resonance condition.

understanding of its band structure. With the rapid advances in nanofabrication, this problem will likely be overcome and the ERS features will become apparent in the spectra, with their distinctive cross linear polarization factor.

Brevity is the soul of wit.

William Shakespeare

7 Conclusions

In this thesis, we study signatures of electronic transitions in the Raman spectra of graphene materials. This idea gets the best of both worlds. On the one hand, the nature of these Raman excitations provides a direct spectroscopic route to study electronic band structures. On the other hand, the choice of graphene as the building block enhances two-steps processes which, in turn, narrows the possible excitations. In particular, only electronic transitions from the n-th valence band to the n-th conduction band are allowed. This selection rule, which is different in optical absorption, is crucial to establish a clean connection between the Raman spectrum and the density of states. In addition, we have shown that the polarisation of the scattered light is perpendicular to that of the incident beam, which is a distinctive feature of this type of Raman scattering. Therefore, electronic Raman scattering not only gives structural electronic information, such as gap sizes (chapter 4), position of van Hove singularities (chapter 5) or flatness of bands (chapter

6.1), but it also has the potential to test our theoretical models and understanding of graphene-based van der Waals heterostructures.

However, we acknowledge that the experimental quest for these signals is not easy. The first pitfall one finds is the quantum efficiency of electronic Raman scattering being about one or two orders of magnitude smaller than the scattering from lattice vibrations. Additionally, unlike the phonon contribution, these signatures do not generate sharp peaks but broader features, which makes them hard to stand out from background noise. In this regard, we might need to wait for the next generation of Raman spectrometers to confirm some of the features presented in chapter 4. The second difficulty has to do with the sensitivity of the electronic dispersion to the stacking. In particular, we study in chapter 5 that the stacking between consecutive layers of graphene can lead to two completely different dispersions around the $\boldsymbol{K}_\xi$ points, and in chapter 6.1 changing the angle between two layers of graphene by as little as 0.1° can shift saddle points in the dispersion by $\sim$ 10 meV. For this reason, sample preparation is a specially important factor towards the feasibility of the proposed experimental observations.

References

[1] Benjamin Collins Brodie. XIII. On the atomic weight of graphite. *Philosophical Transactions of the Royal Society of London*, 149:249–259, January 1859.

[2] P. Debye and P. Scherrer. Interferenzen an regellos orientierten Teilchen im Röntgenlicht. I. *Nachrichten von der Gesellschaft der Wissenschaften zu Göttingen, Mathematisch-Physikalische Klasse*, 1916:1–15, 1916.

[3] John Desmond Bernal and William Lawrence Bragg. The structure of graphite. *Proceedings of the Royal Society of London. Series A, Containing Papers of a Mathematical and Physical Character*, 106(740):749–773, December 1924.

[4] P. R. Wallace. The Band Theory of Graphite. *Physical Review*, 71(9):622–634, May 1947.

[5] H. P. Boehm, A. Clauss, G. O. Fischer, and U. Hofmann. Das Adsorptionsverhalten sehr dünner Kohlenstoff-Folien. *Zeitschrift für anorganische und allgemeine Chemie*, 316(3-4):119–127, 1962.

[6] A. J. Van Bommel, J. E. Crombeen, and A. Van Tooren. LEED and Auger electron observations of the SiC(0001) surface. *Surface Science*, 48(2):463–472, March 1975.

[7] Chuhei Oshima and Ayato Nagashima. Ultra-thin epitaxial films of graphite and hexagonal boron nitride on solid surfaces. *Journal of Physics: Condensed Matter*, 9(1):1–20, January 1997.

[8] D. P. DiVincenzo and E. J. Mele. Self-consistent effective-mass theory for intralayer screening in graphite intercalation compounds. *Physical Review B*, 29(4):1685–1694, February 1984.

[9] Sumio Iijima. Direct observation of the tetrahedral bonding in graphitized carbon black by high resolution electron microscopy. *Journal of Crystal Growth*, 50(3):675–683, November 1980.

[10] H. W. Kroto, J. R. Heath, S. C. O'Brien, R. F. Curl, and R. E. Smalley. C 60 : Buckminsterfullerene. *Nature*, 318(6042):162–163, November 1985.

[11] D. S. Bethune, C. H. Kiang, M. S. de Vries, G. Gorman, R. Savoy, J. Vazquez, and R. Beyers. Cobalt-catalysed growth of carbon nanotubes with single-atomic-layer walls. *Nature*, 363(6430):605–607, June 1993.

[12] Sumio Iijima and Toshinari Ichihashi. Single-shell carbon nanotubes of 1-nm diameter. *Nature*, 363(6430):603–605, June 1993.

[13] K. S. Novoselov. Electric Field Effect in Atomically Thin Carbon Films. *Science*, 306(5696):666–669, October 2004.

[14] E. Peierls. Bemerkungen zur Theorie der Metalle. *Zeitschrift für Physik*, 88(11):786–791, November 1934.

[15] N. D. Mermin and H. Wagner. Absence of Ferromagnetism or Antiferromagnetism in One- or Two-Dimensional Isotropic Heisenberg Models. *Physical Review Letters*, 17(22):1133–1136, November 1966.

[16] N. D. Mermin. Crystalline Order in Two Dimensions. *Physical Review*, 176(1):250–254, December 1968.

[17] Sidney Coleman. There are no Goldstone bosons in two dimensions. *Communications in Mathematical Physics*, 31(4):259–264, December 1973.

[18] Alexander A. Balandin, Suchismita Ghosh, Wenzhong Bao, Irene Calizo, Desalegne Teweldebrhan, Feng Miao, and Chun Ning Lau. Superior Thermal Conductivity of Single-Layer Graphene. *Nano Letters*, 8(3):902–907, March 2008.

[19] A. K. Geim and K. S. Novoselov. The rise of graphene. *Nature Materials*, 6(3):183–191, March 2007.

[20] C. L. Kane and E. J. Mele. Quantum Spin Hall Effect in Graphene. *Physical Review Letters*, 95(22):226801, November 2005.

[21] J. Sichau, M. Prada, T. Anlauf, T. J. Lyon, B. Bosnjak, L. Tiemann, and R. H. Blick. Resonance Microwave Measurements of an Intrinsic Spin-Orbit Coupling Gap in Graphene: A Possible Indication of a Topological State. *Physical Review Letters*, 122(4):046403, February 2019.

[22] Nikolaos Tombros, Csaba Jozsa, Mihaita Popinciuc, Harry T. Jonkman, and Bart J. van Wees. Electronic spin transport and spin precession in single graphene layers at room temperature. *Nature*, 448(7153):571–574, August 2007.

[23] Sungjae Cho, Yung-Fu Chen, and Michael S. Fuhrer. Gate-tunable graphene spin valve. *Applied Physics Letters*, 91(12):123105, September 2007.

[24] Megumi Ohishi, Masashi Shiraishi, Ryo Nouchi, Takayuki Nozaki, Teruya Shinjo, and Yoshishige Suzuki. Spin Injection into a Graphene Thin Film at Room Temperature. *Japanese Journal of Applied Physics*, 46(7L):L605, June 2007.

[25] R. R. Nair, P. Blake, A. N. Grigorenko, K. S. Novoselov, T. J. Booth, T. Stauber, N. M. R. Peres, and A. K. Geim. Fine Structure Constant Defines Visual Transparency of Graphene. *Science*, 320(5881):1308–1308, June 2008.

[26] Peng Zhang, Lulu Ma, Feifei Fan, Zhi Zeng, Cheng Peng, Phillip E. Loya, Zheng Liu, Yongji Gong, Jiangnan Zhang, Xingxiang Zhang, Pulickel M. Ajayan, Ting Zhu, and Jun Lou. Fracture toughness of graphene. *Nature Communications*, 5(1):1–7, April 2014.

[27] Cardea zero: https://www.teamgroupinc.com/en/product/cardea-zero (accessed on 30-09-19).

[28] ZOLO. https://zoloaudio.com/ (accessed on 30-09-19).

[29] Emberion. https://www.emberion.com/ (accessed on 30-09-19).

[30] Versarien plc - Developing advanced materials and enabling engineering exploitation. http://www.versarien.com/ (accessed on 30-09-19).

[31] http://www.thebbsa.co.uk/the-team/directory/dom-parsons (accessed on 30-09-19).

[32] Yi Lin, Tiffany V. Williams, and John W. Connell. Soluble, Exfoliated Hexagonal Boron Nitride Nanosheets. *The Journal of Physical Chemistry Letters*, 1(1):277–283, January 2010.

[33] Jonathan N. Coleman, Mustafa Lotya, Arlene O'Neill, Shane D. Bergin, Paul J. King, Umar Khan, Karen Young, Alexandre Gaucher, Sukanta De, Ronan J. Smith, Igor V. Shvets, Sunil K. Arora, George Stanton, Hye-Young Kim, Kangho Lee, Gyu Tae Kim, Georg S. Duesberg, Toby Hallam, John J. Boland, Jing Jing Wang, John F. Donegan, Jaime C. Grunlan, Gregory Moriarty, Aleksey Shmeliov, Rebecca J. Nicholls, James M. Perkins, Eleanor M. Grieveson, Koenraad Theuwissen, David W. McComb, Peter D. Nellist, and Valeria Nicolosi. Two-Dimensional Nanosheets Produced by Liquid Exfoliation of Layered Materials. *Science*, 331(6017):568–571, February 2011.

[34] A. K. Geim and I. V. Grigorieva. Van der Waals heterostructures. *Nature*, 499(7459):419–425, July 2013.

[35] Stephen Carr, Daniel Massatt, Shiang Fang, Paul Cazeaux, Mitchell Luskin, and Efthimios Kaxiras. Twistronics: Manipulating the electronic properties of two-dimensional layered structures through their twist angle. *Physical Review B*, 95(7):075420, February 2017.

[36] C. V. Raman. A new radiation. *Indian Journal of Physics*, 2:387–398, 1928.

[37] André Braz, Maria López-López, and Carmen García-Ruiz. Raman spectroscopy for forensic analysis of inks in questioned documents. *Forensic Science International*, 232(1):206–212, October 2013.

[38] Yves Roggo, Klara Degardin, and Pierre Margot. Identification of pharmaceutical tablets by Raman spectroscopy and chemometrics. *Talanta*, 81(3):988–995, May 2010.

[39] Challa S. S. R. Kumar, editor. *Raman Spectroscopy for Nanomaterials Characterization*. Springer Berlin Heidelberg, Berlin, Heidelberg, 2012.

[40] Sven Reichardt and Ludger Wirtz. Raman Spectroscopy of Graphene. *arXiv:1703.06909 [cond-mat]*, January 2017. arXiv: 1703.06909.

[41] A. H. Castro Neto, F. Guinea, N. M. R. Peres, K. S. Novoselov, and A. K. Geim. The electronic properties of graphene. *Reviews of Modern Physics*, 81(1):109–162, January 2009.

[42] A. Kretinin, G. L. Yu, R. Jalil, Y. Cao, F. Withers, A. Mishchenko, M. I. Katsnelson, K. S. Novoselov, A. K. Geim, and F. Guinea. Quantum capacitance measurements of electron-hole asymmetry and next-nearest-neighbor hopping in graphene. *Physical Review B*, 88(16):165427, October 2013.

[43] J. E. Lennard-Jones. The electronic structure of some diatomic molecules. *Transactions of the Faraday Society*, 25(0):668–686, January 1929.

[44] Felix Bloch. Über die Quantenmechanik der Elektronen in Kristallgittern. *Zeitschrift für Physik*, 52(7):555–600, July 1929.

[45] Paul Adrien Maurice Dirac and Ralph Howard Fowler. The quantum theory of the electron. *Proceedings of the Royal Society of London. Series A, Containing Papers of a Mathematical and Physical Character*, 117(778):610–624, February 1928.

[46] The k p Method - Electronic Properties of Semiconductors | Lok C. Lew Yan Voon | Springer.

[47] Paolo Marconcini and Massimo Macucci. The k.p method and its application to graphene, carbon nanotubes and graphene nanoribbons: the Dirac equation. *La Rivista del Nuovo Cimento*, 34(809):489–584, July 2011. arXiv: 1105.1351.

[48] Elena Stolyarova, Kwang Taeg Rim, Sunmin Ryu, Janina Maultzsch, Philip Kim, Louis E. Brus, Tony F. Heinz, Mark S. Hybertsen, and George W. Flynn. High-resolution scanning tunneling microscopy imaging of mesoscopic graphene sheets on an insulating surface. *Proceedings of the National Academy of Sciences*, 104(22):9209–9212, May 2007.

[49] Alex W. Robertson and Jamie H. Warner. Atomic resolution imaging of graphene by transmission electron microscopy. *Nanoscale*, 5(10):4079–4093, May 2013.

[50] C. R. Dean, A. F. Young, I. Meric, C. Lee, L. Wang, S. Sorgenfrei, K. Watanabe, T. Taniguchi, P. Kim, K. L. Shepard, and J. Hone. Boron nitride substrates for high-quality graphene electronics. *Nature Nanotechnology*, 5(10):722–726, October 2010.

[51] Jiamin Xue, Javier Sanchez-Yamagishi, Danny Bulmash, Philippe Jacquod, Aparna Deshpande, K. Watanabe, T. Taniguchi, Pablo Jarillo-Herrero, and Brian J. LeRoy. Scanning tunnelling microscopy and spectroscopy of ultra-flat graphene on hexagonal boron nitride. *Nature Materials*, 10(4):282–285, April 2011.

[52] M. I. Katsnelson, K. S. Novoselov, and A. K. Geim. Chiral tunnelling and the Klein paradox in graphene. *Nature Physics*, 2(9):620–625, September 2006.

[53] Andrea F. Young and Philip Kim. Quantum interference and Klein tunnelling in graphene heterojunctions. *Nature Physics*, 5(3):222–226, March 2009.

[54] B. Huard, J. A. Sulpizio, N. Stander, K. Todd, B. Yang, and D. Goldhaber-Gordon. Transport Measurements Across a Tunable Potential Barrier in Graphene. *Physical Review Letters*, 98(23):236803, June 2007.

[55] N. Stander, B. Huard, and D. Goldhaber-Gordon. Evidence for Klein Tunneling in Graphene p – n Junctions. *Physical Review Letters*, 102(2):026807, January 2009.

[56] C. W. J. Beenakker. *Colloquium* : Andreev reflection and Klein tunneling in graphene. *Reviews of Modern Physics*, 80(4):1337–1354, October 2008.

[57] Yisong Zheng and Tsuneya Ando. Hall conductivity of a two-dimensional graphite system. *Physical Review B*, 65(24):245420, June 2002.

[58] Z. Jiang, Y. Zhang, Y.-W. Tan, H.L. Stormer, and P. Kim. Quantum Hall effect in graphene. *Solid State Communications*, 143(1-2):14–19, July 2007.

[59] K. S. Novoselov, Z. Jiang, Y. Zhang, S. V. Morozov, H. L. Stormer, U. Zeitler, J. C. Maan, G. S. Boebinger, P. Kim, and A. K. Geim. Room-Temperature Quantum Hall Effect in Graphene. *Science*, 315(5817):1379–1379, March 2007.

[60] Cheol-Hwan Park, Feliciano Giustino, Catalin D. Spataru, Marvin L. Cohen, and Steven G. Louie. Angle-Resolved Photoemission Spectra of Graphene from First-Principles Calculations. *Nano Letters*, 9(12):4234–4239, December 2009.

[61] M. Mucha-Kruczyński, O. Tsyplyatyev, A. Grishin, E. McCann, Vladimir I. Fal'ko, Aaron Bostwick, and Eli Rotenberg. Characterization of graphene through anisotropy of constant-energy maps in angle-resolved photoemission. *Physical Review B*, 77(19):195403, May 2008.

[62] M. Mucha-Kruczyński, J. R. Wallbank, and V. I. Fal'ko. Moiré miniband features in the angle-resolved photoemission spectra of graphene/ h BN heterostructures. *Physical Review B*, 93(8):085409, February 2016.

[63] A. C. Ferrari, J. C. Meyer, V. Scardaci, C. Casiraghi, M. Lazzeri, F. Mauri, S. Piscanec, D. Jiang, K. S. Novoselov, S. Roth, and A. K. Geim. Raman Spectrum of Graphene and Graphene Layers. *Physical Review Letters*, 97(18):187401, October 2006.

[64] Andrea C. Ferrari and Denis M. Basko. Raman spectroscopy as a versatile tool for studying the properties of graphene. *Nature Nanotechnology*, 8(4):235–246, April 2013.

[65] Julia Tesch, Fabian Paschke, Mikhail Fonin, Marko Wietstruk, Stefan Böttcher, Roland J. Koch, Aaron Bostwick, Chris Jozwiak, Eli Rotenberg, Anna Makarova, Beate Paulus, Elena Voloshina, and Yuriy Dedkov. The graphene/n-Ge(110) interface: structure, doping, and electronic properties. *Nanoscale*, 10(13):6088–6098, 2018.

[66] J. L. McChesney, Aaron Bostwick, Taisuke Ohta, Thomas Seyller, Karsten Horn, J. González, and Eli Rotenberg. Extended van Hove Singularity and Superconducting Instability in Doped Graphene. *Physical Review Letters*, 104(13):136803, April 2010.

[67] Kin Fai Mak, Matthew Y. Sfeir, James A. Misewich, and Tony F. Heinz. The evolution of electronic structure in few-layer graphene revealed by optical spectroscopy. *Proceedings of the National Academy of Sciences*, 107(34):14999–15004, August 2010.

[68] A. N. Popova. Crystallographic analysis of graphite by X-Ray diffraction. *Coke and Chemistry*, 60(9):361–365, September 2017.

[69] Suman Kalyan Pal. Versatile photoluminescence from graphene and its derivatives. *Carbon*, 88:86–112, July 2015.

[70] Kevin R. Knox, Shancai Wang, Alberto Morgante, Dean Cvetko, Andrea Locatelli, Tevfik Onur Mentes, Miguel Angel Niño, Philip Kim, and R. M. Osgood. Spectromicroscopy of single and multilayer graphene supported by a weakly interacting substrate. *Physical Review B*, 78(20):201408, November 2008.

[71] D. M. Basko. Theory of resonant multiphonon Raman scattering in graphene. *Physical Review B*, 78(12):125418, September 2008. arXiv: 0804.3304.

[72] A. Gupta, G. Chen, P. Joshi, S. Tadigadapa, and Eklund. Raman Scattering from High-Frequency Phonons in Supported n-Graphene Layer Films. *Nano Letters*, 6(12):2667–2673, December 2006.

[73] D. M. Basko, S. Piscanec, and A. C. Ferrari. Electron-electron interactions and doping dependence of the two-phonon Raman intensity in graphene. *Physical Review B*, 80(16):165413, October 2009.

[74] T. M. G. Mohiuddin, A. Lombardo, R. R. Nair, A. Bonetti, G. Savini, R. Jalil, N. Bonini, D. M. Basko, C. Galiotis, N. Marzari, K. S. Novoselov, A. K. Geim, and A. C. Ferrari. Uniaxial strain in graphene by Raman spectroscopy: G peak splitting, Grüneisen parameters, and sample orientation. *Physical Review B*, 79(20):205433, May 2009.

[75] Axel Eckmann, Alexandre Felten, Artem Mishchenko, Liam Britnell, Ralph Krupke, Kostya S. Novoselov, and Cinzia Casiraghi. Probing the Nature of Defects in Graphene by Raman Spectroscopy. *Nano Letters*, 12(8):3925–3930, August 2012.

[76] P. A. Wolff. Thomson and Raman Scattering by Mobile Electrons in Crystals. *Physical Review Letters*, 16(6):225–228, February 1966.

[77] D. Guidotti, Shui Lai, M. V. Klein, and J. P. Wolfe. Electronic Raman Scattering and Antiresonance Behavior in Highly Stressed Photoexcited Silicon. *Physical Review Letters*, 43(26):1950–1953, December 1979.

[78] Diego Olego and Manuel Cardona. Photoluminescence in heavily doped GaAs. Temperature and hole-concentration dependence. *Physical Review B*, 22(2):886–893, July 1980.

[79] H. Yugami, S. Nakashima, M. Hangyo, K. Sakai, and A. Mitsuishi. Electronic Raman scattering from inter-valence band transition in photo-excited *GaP* and $GaAs_{1-x}p_x$ crystals. *Solid State Communications*, 55(2):159–162, July 1985.

[80] Olevskiy Kashuba and Vladimir I. Fal'ko. Signature of electronic excitations in the Raman spectrum of graphene. *Physical Review B*, 80(24):241404, December 2009.

[81] Marcin Mucha-Kruczyński, Oleksiy Kashuba, and Vladimir I. Fal'ko. Spectral features due to inter-Landau-level transitions in the Raman spectrum of bilayer graphene. *Physical Review B*, 82(4):045405, July 2010.

[82] Oleksiy Kashuba and Vladimir I Fal'ko. Role of electronic excitations in magneto-Raman spectra of graphene. *New Journal of Physics*, 14(10):105016, October 2012.

[83] Ajoy Ghatak and S. Lokanathan. Time Dependent Perturbation Theory. In Ajoy Ghatak and S. Lokanathan, editors, *Quantum Mechanics: Theory and Applications*, Fundamental Theories of Physics, pages 676–715. Springer Netherlands, Dordrecht, 2004.

[84] Paul Adrien Maurice Dirac and Niels Henrik David Bohr. The quantum theory of the emission and absorption of radiation. *Proceedings of the Royal Society of London. Series A, Containing Papers of a Mathematical and Physical Character*, 114(767):243–265, March 1927.

[85] A. García-Ruiz, M. Mucha-Kruczyński, and V. I. Fal'ko. Superconductivity-induced features in the electronic Raman spectrum of monolayer graphene. *Physical Review B*, 97(15):155405, April 2018.

[86] C. Faugeras, M. Amado, P. Kossacki, M. Orlita, M. Kühne, A. A. L. Nicolet, Yu. I. Latyshev, and M. Potemski. Magneto-Raman Scattering of Graphene on Graphite: Electronic and Phonon Excitations. *Physical Review Letters*, 107(3):036807, July 2011.

[87] P. S. Pershan. Magneto-Optical Effects. *Journal of Applied Physics*, 38(3):1482–1490, March 1967.

[88] Edward McCann. Electronic Properties of Monolayer and Bilayer Graphene. In Hassan Raza, editor, *Graphene Nanoelectronics: Metrology,*

Synthesis, Properties and Applications, NanoScience and Technology, pages 237–275. Springer, Berlin, Heidelberg, 2012.

[89] P. Kossacki, C. Faugeras, M. Kühne, M. Orlita, A. A. L. Nicolet, J. M. Schneider, D. M. Basko, Yu. I. Latyshev, and M. Potemski. Electronic excitations and electron-phonon coupling in bulk graphite through Raman scattering in high magnetic fields. *Physical Review B*, 84(23):235138, December 2011.

[90] E. Riccardi, M.-A. Méasson, M. Cazayous, A. Sacuto, and Y. Gallais. Gate-Dependent Electronic Raman Scattering in Graphene. *Physical Review Letters*, 116(6):066805, February 2016.

[91] Yu. S. Ponosov, A. V. Ushakov, and S. V. Streltsov. Electronic Raman scattering in graphite and single-layer and few-layer graphene. *Physical Review B*, 91(19):195435, May 2015.

[92] J. Bardeen, L. N. Cooper, and J. R. Schrieffer. Theory of Superconductivity. *Physical Review*, 108(5):1175–1204, December 1957.

[93] J. Robert Schrieffer. *Theory Of Superconductivity*. CRC Press, March 2018.

[94] A. R. Akhmerov and C. W. J. Beenakker. Detection of Valley Polarization in Graphene by a Superconducting Contact. *Physical Review Letters*, 98(15):157003, April 2007.

[95] Hubert B. Heersche, Pablo Jarillo-Herrero, Jeroen B. Oostinga, Lieven M. K. Vandersypen, and Alberto F. Morpurgo. Bipolar supercurrent in graphene. *Nature*, 446(7131):56–59, March 2007.

[96] Jacob Linder, Takehito Yokoyama, Daniel Huertas-Hernando, and Asle Sudbø. Supercurrent Switch in Graphene $\ensuremath{\pi}$ Junctions. *Physical Review Letters*, 100(18):187004, May 2008.

[97] Gianni Profeta, Matteo Calandra, and Francesco Mauri. Phonon-mediated superconductivity in graphene by lithium deposition. *Nature Physics*, 8(2):131–134, February 2012.

[98] B. M. Ludbrook, G. Levy, P. Nigge, M. Zonno, M. Schneider, D. J. Dvorak, C. N. Veenstra, S. Zhdanovich, D. Wong, P. Dosanjh, C. Straßer, A. Stöhr,

S. Forti, C. R. Ast, U. Starke, and A. Damascelli. Evidence for superconductivity in Li-decorated monolayer graphene. *Proceedings of the National Academy of Sciences*, 112(38):11795–11799, September 2015.

[99] J. Chapman, Y. Su, C. A. Howard, D. Kundys, A. N. Grigorenko, F. Guinea, A. K. Geim, I. V. Grigorieva, and R. R. Nair. Superconductivity in Ca-doped graphene laminates. *Scientific Reports*, 6:23254, March 2016.

[100] M. V. Klein and S. B. Dierker. Theory of Raman scattering in superconductors. *Physical Review B*, 29(9):4976–4991, May 1984.

[101] L. M. Fraas, P. F. Williams, and S. P. S. Porto. Photoluminescence studies of superconducting nb_3 sn. *Solid State Communications*, 8(24):2113–2115, December 1970.

[102] C. Kendziora and A. Rosenberg. a-b plane anisotropy of the superconducting gap in $Bi_2Sr_2CaCu_2O_{8+\delta}$. *Physical Review B*, 52(14):R9867–R9870, October 1995.

[103] X. K. Chen, J. G. Naeini, K. C. Hewitt, J. C. Irwin, R. Liang, and W. N. Hardy. Electronic Raman scattering in underdoped $YBa_2Cu_3O_{6.5}$. *Physical Review B*, 56(2):R513–R516, July 1997.

[104] J. G. Naeini, X. K. Chen, J. C. Irwin, M. Okuya, T. Kimura, and K. Kishio. Doping dependence of the pseudogap in $La_{2-x}Sr_xCuO_4$. *Physical Review B*, 59(14):9642–9648, April 1999.

[105] M. Opel, R. Nemetschek, C. Hoffmann, R. Philipp, P. F. Müller, R. Hackl, I. Tüttő, A. Erb, B. Revaz, E. Walker, H. Berger, and L. Forró. Carrier relaxation, pseudogap, and superconducting gap in high-t_c cuprates: A Raman scattering study. *Physical Review B*, 61(14):9752–9774, April 2000.

[106] S. Sugai and T. Hosokawa. Relation between the Superconducting Gap Energy and the Two-Magnon Raman Peak Energy in $Bi_2Sr_2Ca_{1-x}Y_xCu_2O_{8+\delta}$. *Physical Review Letters*, 85(5):1112–1115, July 2000.

[107] F. Venturini, M. Opel, R. Hackl, H. Berger, L. Forró, and B. Revaz. Doping dependence of the electronic Raman spectra in cuprates. *Journal of Physics and Chemistry of Solids*, 63(12):2345–2348, December 2002.

[108] Annica M. Black-Schaffer and Carsten Honerkamp. Chirald-wave superconductivity in doped graphene. *Journal of Physics: Condensed Matter*, 26(42):423201, September 2014.

[109] Second Quantization. In Franz Schwabl, editor, *Advanced Quantum Mechanics*, pages 3–32. Springer Berlin Heidelberg, Berlin, Heidelberg, 2008.

[110] A. Di Bernardo, O. Millo, M. Barbone, H. Alpern, Y. Kalcheim, U. Sassi, A. K. Ott, D. De Fazio, D. Yoon, M. Amado, A. C. Ferrari, J. Linder, and J. W. A. Robinson. p-wave triggered superconductivity in single-layer graphene on an electron-doped oxide superconductor. *Nature Communications*, 8(1):14024, April 2017.

[111] J. P. L. Faye, P. Sahebsara, and D. Sénéchal. Chiral triplet superconductivity on the graphene lattice. *Physical Review B*, 92(8):085121, August 2015.

[112] P. M. Chaikin and T. C. Lubensky. Principles of Condensed Matter Physics by P. M. Chaikin, June 1995.

[113] Yoichiro Nambu. Quasi-Particles and Gauge Invariance in the Theory of Superconductivity. *Physical Review*, 117(3):648–663, February 1960.

[114] N. N. Bogoljubov, V. V. Tolmachov, and D. V. Širkov. A New Method in the Theory of Superconductivity. *Fortschritte der Physik*, 6(11-12):605–682, 1958.

[115] Lihao Han, Miro Zeman, and Arno H. M. Smets. Raman study of laser-induced heating effects in free-standing silicon nanocrystals. *Nanoscale*, 7(18):8389–8397, 2015.

[116] R R Haering. Band structure of rhombohedral graphite. *Canadian Journal of physics*, pages 352–362, 1958.

[117] Tataiana Latychevskaia, Seok-Kyun Son, Yaping Yang, Dale Chancellor, Michael Brown, Servet Ozdemir, Ivan Madan, Gabriele Berruto, Fabrizio Carbone, Artem Mishchenko, and Kostya S. Novoselov. Stacking transition in rhombohedral graphite. *Frontiers of Physics*, 14(1):13608, February 2019.

[118] Damian Moran, Frank Stahl, Holger F. Bettinger, Henry F. Schaefer, and Paul v. R. Schleyer. Towards Graphite: Magnetic Properties of Large

Polybenzenoid Hydrocarbons. *Journal of the American Chemical Society*, 125(22):6746–6752, June 2003.

[119] P. Esquinazi, D. Spemann, R. Höhne, A. Setzer, K.-H. Han, and T. Butz. Induced Magnetic Ordering by Proton Irradiation in Graphite. *Physical Review Letters*, 91(22):227201, November 2003.

[120] J. Xhie, K. Sattler, U. Müller, N. Venkateswaran, and G. Raina. Periodic charge-density modulations on graphite near platinum particles. *Physical Review B*, 43(11):8917–8923, April 1991.

[121] P. Ruffieux, M. Melle-Franco, O. Gröning, M. Bielmann, F. Zerbetto, and P. Gröning. Charge-density oscillation on graphite induced by the interference of electron waves. *Physical Review B*, 71(15):153403, April 2005.

[122] Haiwen Liu, Hua Jiang, and X. C. Xie. Intrinsic superconductivity in ABA-stacked trilayer graphene. *AIP Advances*, 2(4):041405, December 2012.

[123] P. Esquinazi, N. García, J. Barzola-Quiquia, P. Rödiger, K. Schindler, J.-L. Yao, and M. Ziese. Indications for intrinsic superconductivity in highly oriented pyrolytic graphite. *Physical Review B*, 78(13):134516, October 2008.

[124] D. D. L. Chung. A review of exfoliated graphite. *Journal of Materials Science*, 51(1):554–568, January 2016.

[125] A. Grüneis, R. Saito, Ge. G. Samsonidze, T. Kimura, M. A. Pimenta, A. Jorio, A. G. Souza Filho, G. Dresselhaus, and M. S. Dresselhaus. Inhomogeneous optical absorption around the *K* point in graphite and carbon nanotubes. *Physical Review B*, 67(16):165402, April 2003.

[126] Abderrezak Torche, Francesco Mauri, Jean-Christophe Charlier, and Matteo Calandra. First-principles determination of the Raman fingerprint of rhombohedral graphite. *Physical Review Materials*, 1(4):041001, September 2017.

[127] J. W. McClure. Band Structure of Graphite and de Haas-van Alphen Effect. *Physical Review*, 108(3):612–618, November 1957.

[128] J. C. Slonczewski and P. R. Weiss. Band Structure of Graphite. *Physical Review*, 109(2):272–279, January 1958.

[129] Aitor García-Ruiz, Sergey Slizovskiy, Marcin Mucha-Kruczyński, and Vladimir I. Fal'ko. Spectroscopic Signatures of Electronic Excitations in Raman Scattering in Thin Films of Rhombohedral Graphite. *Nano Letters*, 19(9):6152–6156, September 2019.

[130] L. M. Zhang, Z. Q. Li, D. N. Basov, M. M. Fogler, Z. Hao, and M. C. Martin. Determination of the electronic structure of bilayer graphene from infrared spectroscopy. *Physical Review B*, 78(23):235408, December 2008.

[131] Z. Q. Li, E. A. Henriksen, Z. Jiang, Z. Hao, M. C. Martin, P. Kim, H. L. Stormer, and D. N. Basov. Band Structure Asymmetry of Bilayer Graphene Revealed by Infrared Spectroscopy. *Physical Review Letters*, 102(3):037403, January 2009.

[132] L. M. Malard, J. Nilsson, D. C. Elias, J. C. Brant, F. Plentz, E. S. Alves, A. H. Castro Neto, and M. A. Pimenta. Probing the electronic structure of bilayer graphene by Raman scattering. *Physical Review B*, 76(20):201401, November 2007.

[133] A. B. Kuzmenko, I. Crassee, D. van der Marel, P. Blake, and K. S. Novoselov. Determination of the gate-tunable band gap and tight-binding parameters in bilayer graphene using infrared spectroscopy. *Physical Review B*, 80(16):165406, October 2009.

[134] Thiti Taychatanapat, Kenji Watanabe, Takashi Taniguchi, and Pablo Jarillo-Herrero. Quantum Hall effect and Landau-level crossing of Dirac fermions in trilayer graphene. *Nature Physics*, 7(8):621–625, August 2011.

[135] M. S. Dresselhaus and G. Dresselhaus. Intercalation compounds of graphite. *Advances in Physics*, 51(1):1–186, January 2002.

[136] Edward McCann and Mikito Koshino. The electronic properties of bilayer graphene. *Reports on Progress in Physics*, 76(5):056503, May 2013.

[137] M Lifshitz. Anomalies of electron characteristics of metal in the high pressure region. *Journal of experimental and theoretical physics*, 11(5):6, 1959.

[138] Dominik Suszalski, Grzegorz Rut, and Adam Rycerz. Lifshitz transition and thermoelectric properties of bilayer graphene. *Physical Review B*, 97(12):125403, March 2018.

[139] Anastasia Varlet, Marcin Mucha-Kruczyński, Dominik Bischoff, Pauline Simonet, Takashi Taniguchi, Kenji Watanabe, Vladimir Fal'ko, Thomas Ihn, and Klaus Ensslin. Tunable Fermi surface topology and Lifshitz transition in bilayer graphene. *arXiv:1508.02922 [cond-mat]*, August 2015. arXiv: 1508.02922.

[140] I. V. Iorsh, K. Dini, O. V. Kibis, and I. A. Shelykh. Optically induced Lifshitz transition in bilayer graphene. *Physical Review B*, 96(15):155432, October 2017.

[141] Yanmeng Shi, Shi Che, Kuan Zhou, Supeng Ge, Ziqi Pi, Timothy Espiritu, Takashi Taniguchi, Kenji Watanabe, Yafis Barlas, Roger Lake, and Chun Ning Lau. Tunable Lifshitz Transitions and Multiband Transport in Tetralayer Graphene. *Physical Review Letters*, 120(9):096802, February 2018.

[142] János K. Asbóth, László Oroszlány, and András Pályi. A Short Course on Topological Insulators: Band-structure topology and edge states in one and two dimensions. *arXiv:1509.02295 [cond-mat]*, 919, 2016. arXiv: 1509.02295.

[143] Elisa Riccardi, Oleksiy Kashuba, Maximilien Cazayous, Marie-Aude Méasson, Alain Sacuto, and Yann Gallais. Probing chiral electronic excitations in bilayer graphene by Raman scattering. *Physical Review Materials*, 3(1):014002, January 2019.

[144] Younes Henni, Hector Pablo Ojeda Collado, Karol Nogajewski, Maciej R. Molas, Gonzalo Usaj, Carlos A. Balseiro, Milan Orlita, Marek Potemski, and Clement Faugeras. Rhombohedral Multilayer Graphene: A Magneto-Raman Scattering Study. *Nano Letters*, 16(6):3710–3716, June 2016.

[145] Sam Griffiths. https://artplusmarketing.com/practical-magic-the-moire-effect-3faecc04cd07 (accessed on 30-09-19), June 2017.

[146] H. Hashimoto, M. Mannami, and T. Naiki. Dynamical Theory of Electron Diffraction for the Electron Microscopic Image of Crystal Lattices II. Image of Superposed Crystals (Moiré Pattern). *Philosophical Transactions of the Royal Society of London. Series A, Mathematical and Physical Sciences*, 253(1033):490–516, 1961.

[147] D. W. Pashley, J. W. Menter, and G. A. Bassett. Observation of Dislocations in Metals by Means of Moiré Patterns on Electron Micrographs. *Nature*, 179(4563):752–755, April 1957.

[148] Lars A. Bergkvist and Ivan Forsen. Leading mark indicator. patent number: Us4629325a, December 1986.

[149] H. Saadaoui, J. C. Roux, S. Flandrois, and B. Nysten. Graphitization of pyrocarbons: An STM study. *Carbon*, 31(3):481–486, January 1993.

[150] J. M. B. Lopes dos Santos, N. M. R. Peres, and A. H. Castro Neto. Graphene Bilayer with a Twist: Electronic Structure. *Physical Review Letters*, 99(25):256802, December 2007.

[151] Rafi Bistritzer and Allan H. MacDonald. Moiré bands in twisted double-layer graphene. *Proceedings of the National Academy of Sciences*, 108(30):12233–12237, July 2011.

[152] J. M. B. Lopes dos Santos, N. M. R. Peres, and A. H. Castro Neto. Continuum model of the twisted graphene bilayer. *Physical Review B*, 86(15):155449, October 2012.

[153] Mikito Koshino. Interlayer interaction in general incommensurate atomic layers. *New Journal of Physics*, 17(1):015014, January 2015.

[154] Francisco Guinea and Niels R. Walet. Continuum models for twisted bilayer graphene: Effect of lattice deformation and hopping parameters. *Physical Review B*, 99(20):205134, May 2019.

[155] Stephen Carr, Shiang Fang, Ziyan Zhu, and Efthimios Kaxiras. Exact continuum model for low-energy electronic states of twisted bilayer graphene. *Physical Review Research*, 1(1):013001, August 2019.

[156] L. P. Gorkov and George Grüner, editors. *Charge density waves in solids*. Number v. 25 in Modern problems in condensed matter sciences. North-Holland : Sole distributors for the USA and Canada, Elsevier Science Pub. Co, Amsterdam ; New York : New York, NY, USA, 1989.

[157] Yuan Cao, Valla Fatemi, Shiang Fang, Kenji Watanabe, Takashi Taniguchi, Efthimios Kaxiras, and Pablo Jarillo-Herrero. Unconventional superconductivity in magic-angle graphene superlattices. *Nature*, 556(7699):43–50, April 2018.

[158] Yuan Cao, Valla Fatemi, Ahmet Demir, Shiang Fang, Spencer L. Tomarken, Jason Y. Luo, Javier D. Sanchez-Yamagishi, Kenji Watanabe, Takashi Taniguchi, Efthimios Kaxiras, Ray C. Ashoori, and Pablo Jarillo-Herrero. Correlated insulator behaviour at half-filling in magic-angle graphene superlattices. *Nature*, 556(7699):80–84, April 2018.

[159] Pilkyung Moon and Mikito Koshino. Optical absorption in twisted bilayer graphene. *Physical Review B*, 87(20):205404, May 2013.

[160] Pilkyung Moon, Young-Woo Son, and Mikito Koshino. Optical absorption of twisted bilayer graphene with interlayer potential asymmetry. *Physical Review B*, 90(15):155427, October 2014.

[161] Kwangnam Yu, Nguyen Van Luan, Taesoo Kim, Jiwon Jeon, Jiho Kim, Pilkyung Moon, Young Hee Lee, and E. J. Choi. Gate tunable optical absorption and band structure of twisted bilayer graphene. *Physical Review B*, 99(24):241405, June 2019.

[162] S. Shallcross, S. Sharma, E. Kandelaki, and O. A. Pankratov. Electronic structure of turbostratic graphene. *Physical Review B*, 81(16):165105, April 2010.

[163] E. J. Mele. Commensuration and interlayer coherence in twisted bilayer graphene. *Physical Review B*, 81(16):161405, April 2010.

[164] J. C. Slater and G. F. Koster. Simplified LCAO Method for the Periodic Potential Problem. *Physical Review*, 94(6):1498–1524, June 1954.

[165] Lei Liao, Huan Wang, Han Peng, Jianbo Yin, Ai Leen Koh, Yulin Chen, Qin Xie, Hailin Peng, and Zhongfan Liu. van Hove Singularity Enhanced Photochemical Reactivity of Twisted Bilayer Graphene. *Nano Letters*, 15(8):5585–5589, August 2015.

[166] Jianbo Yin, Huan Wang, Han Peng, Zhenjun Tan, Lei Liao, Li Lin, Xiao Sun, Ai Leen Koh, Yulin Chen, Hailin Peng, and Zhongfan Liu. Selectively enhanced photocurrent generation in twisted bilayer graphene with van Hove singularity. *Nature Communications*, 7(1):1–8, March 2016.

[167] Han Peng, Niels B. M. Schröter, Jianbo Yin, Huan Wang, Ting-Fung Chung, Haifeng Yang, Sandy Ekahana, Zhongkai Liu, Juan Jiang, Lexian Yang, Teng Zhang, Cheng Chen, Heng Ni, Alexey Barinov, Yong P. Chen, Zhongfan

Liu, Hailin Peng, and Yulin Chen. Substrate Doping Effect and Unusually Large Angle van Hove Singularity Evolution in Twisted Bi- and Multilayer Graphene. *Advanced Materials*, 29(27):1606741, 2017.

[168] Mikito Koshino, Noah F. Q. Yuan, Takashi Koretsune, Masayuki Ochi, Kazuhiko Kuroki, and Liang Fu. Maximally Localized Wannier Orbitals and the Extended Hubbard Model for Twisted Bilayer Graphene. *Physical Review X*, 8(3):031087, September 2018.

[169] Jian Kang and Oskar Vafek. Symmetry, Maximally Localized Wannier States, and a Low-Energy Model for Twisted Bilayer Graphene Narrow Bands. *Physical Review X*, 8(3):031088, September 2018.

[170] Grigory Tarnopolsky, Alex Jura Kruchkov, and Ashvin Vishwanath. Origin of Magic Angles in Twisted Bilayer Graphene. *Physical Review Letters*, 122(10):106405, March 2019.

[171] Robin W. Havener, Houlong Zhuang, Lola Brown, Richard G. Hennig, and Jiwoong Park. Angle-Resolved Raman Imaging of Interlayer Rotations and Interactions in Twisted Bilayer Graphene. *Nano Letters*, 12(6):3162–3167, June 2012.

[172] Rui He, Ting-Fung Chung, Conor Delaney, Courtney Keiser, Luis A. Jauregui, Paul M. Shand, C. C. Chancey, Yanan Wang, Jiming Bao, and Yong P. Chen. Observation of Low Energy Raman Modes in Twisted Bilayer Graphene. *Nano Letters*, 13(8):3594–3601, August 2013.

[173] Ado Jorio and Luiz Gustavo Cançado. Raman spectroscopy of twisted bilayer graphene. *Solid State Communications*, 175-176:3–12, December 2013.

[174] Ting-Fung Chung, Yang Xu, and Yong P. Chen. Transport measurements in twisted bilayer graphene: Electron-phonon coupling and Landau level crossing. *Physical Review B*, 98(3):035425, July 2018.